

High Peak Power Ultra-Short Pulse Diode-Pumped Yb:KGW Lasers

by

Reza Akbari

A thesis submitted to the Faculty of Graduate Studies of

The University of Manitoba

In partial fulfilment of the requirements of the degree of

DOCTOR OF PHILOSOPHY

Department of Electrical and Computer Engineering

University of Manitoba

Winnipeg

Copyright © 2017 by Reza Akbari

Abstract

Today, the development of a simple, compact and cost-effective laser source which is capable of generating powerful pulses is of importance for a variety of optical applications. The generation of high power pulses in the sub-100 femtosecond range is a demanding task and requires careful choice of laser gain material and laser cavity design. In this regard, the Yb-doped laser crystals are good candidates for high power regime due to their high thermal conductivity and for ultrashort pulse generation because of their broad gain bandwidth. The commercially available Yb:KGW laser crystal was chosen for this work which is capable of generating watt-level sub-100 fs pulses.

In the first stage of this work, a high power CW dual-wavelength laser with high optical efficiency was demonstrated based on a simple approach, i.e., by using a single birefringent filter plate (BRF). The diode-pumped Yb:KGW laser delivered radiation with wavelength pair at 1014.6 nm and 1041.3 nm with 3.4 W of output power and considerably higher efficiency and power when compared to previous works. The wavelength pair tunability was possible by using a BRF with different thickness which offers additional flexibility. Such a powerful dual-wavelength source can be used for generating THz radiation for imaging applications.

The focus of the rest of this work was to generate powerful ultrashort pulses. The generation of watt-level sub-100 fs pulse generation was realized by using a quantum-dot semiconductor saturable absorber mirror (QD-SESAM) in a dual-action with the Kerr lensing effect. The generation of 90 fs pulses with 3.2 W of output power (462 kW of peak power and 41 nJ of energy) was demonstrated. This result exhibited significant increase in the average laser output power and peak power of pulses when compared to the previous results based on QD-SESAMs. The output power of the generated laser was also one of the highest among sub-100 fs diode-pumped bulk Yb-doped lasers. In addition, pulses with duration of 56 fs and 1.95 W of average power were obtained, which were the shortest pulses generated from monoclinic double tungstate crystals (and Yb:KGW laser crystal in particular) and also the most powerful in the sub-60 fs regime.

A watt-level pure Kerr-lens mode-locked (KLM) laser was also realized for the first time with Yb:KGW laser crystal pumped by a multimode fibre-coupled laser diode and without a

semiconductor saturable absorber mirror. The laser delivered 240 fs pulses with 2.3 W of output power and also 120 fs pulses with 1.2 W of output power. These results were the first demonstration of a femtosecond bulk Yb-ion doped KLM laser that produced >1 W of average output power with a cost-effective, highly multimode laser diode as the pump source.

Finally, a numerical investigation of widely-tunable wavelength laser source, i.e., optical parametric oscillator (OPO), pumped by a frequency-doubled mode-locked laser at 532 nm was performed. The properties of three nonlinear crystals (i. e., LBO, BBO and BIBO) were presented and the conditions for the most efficient frequency conversion were investigated. The results of this simulation can be considered as a future development of a high power tunable laser system where the demonstrated lasers in previous section can be used as the source of excitation for the OPO.

Acknowledgements

Foremost, I would like to express my sincere gratitude to my advisor Prof. Arkady Major for his continuous support of my Ph.D study and related research, motivation and immense knowledge.

I would also like to thank the committee members: Prof. Puyan Mojabi and Prof. Francis Lin for their insightful comments and suggestions over the course of my Ph.D study.

My sincere thanks also goes to my colleagues: Dr. Haitao Zhao, Sujith Manjooran and Tanant Waritanant for their stimulating discussions, sharing their experiences and generous help in the laboratory.

I am also especially grateful to the graduate student advisor, Amy Dario, for her generous assistance and guidance in the ECE faculty, University of Manitoba.

I gratefully acknowledge the funding received towards my Ph.D from the University of Manitoba and the Natural Sciences and Engineering Research Council of Canada (NSERC).

Finally, I would like to say a heartfelt thanks to my family: my mother, Sima, my father, Mahmoud and my sister, Raha for always encouraging me to follow my goals and for their emotional support and patience during my Ph.D study.

Table of contents

Abstract	i
Acknowledgements	iii
Table of contents	iv
List of symbols and abbreviations	vii
List of figures	ix
List of tables	xii
Chapter 1. Introduction	1
1.1. Introduction.....	1
1.2. Motivation.....	2
1.3. Objective	4
1.4. Thesis contribution.....	5
1.5. Thesis outline	7
References	9
Chapter 2. Theory and background	12
2.1. Introduction.....	12
2.2. Laser material: Yb:KGW	12
2.3. Group-velocity dispersion (GVD).....	15
2.4. Optical Kerr effect.....	16
2.4.1. Self-phase modulation (SPM)	16
2.4.2. Kerr lensing effect	18
2.5. Mode-locked laser.....	18
2.5.1. Mode-locked laser with saturable absorber	19
2.5.2. Kerr-lens mode-locked laser (KLM)	21
2.5.3. Mode-locked laser model	22
References	24
Chapter 3. Continuous-wave dual-wavelength Yb:KGW laser	26
3.1. Introduction.....	26
3.2. CW dual-wavelength laser	26
3.3. Experiment and results.....	29

3.4. Conclusion.....	32
References	34
Chapter 4. High power femtosecond mode-locked Yb:KGW laser based on quantum-dot saturable absorber and Kerr lensing effect	35
4.1. Introduction.....	35
4.2. Mode-locked laser based on dual-action of quantum-dot saturable absorber and Kerr lensing effect.....	36
4.3. Multi-watt sub-100 fs mode-locked Yb:KGW laser: experiment and results.....	37
4.4. Watt-level sub-60 fs mode-locked Yb:KGW laser: experiment and results	40
4.5. Discussion	44
4.6. Conclusion.....	47
References	49
Chapter 5. High power femtosecond pure Kerr-lens mode-locked Yb:KGW laser	52
5.1. Introduction.....	52
5.2. Mode-locked laser based on Kerr lensing effect.....	52
5.3. Experiment and results.....	54
5.4. Discussion	58
5.5. Conclusion.....	62
References	63
Chapter 6. Simulation of an optical parametric oscillator (OPO) based on the BIBO, BBO and LBO crystals pumped by a frequency-doubled mode-locked Yb:KGW laser	66
6.1. Introduction.....	66
6.2. Optical parametric oscillator and nonlinear crystals	67
6.3. Optical properties	70
6.4. Phase-matching properties	71
6.5. Dispersive properties.....	75
6.6. Spectral properties.....	78
6.7. Conclusion.....	80
References	82

Chapter 7. Conclusions and future works	87
7.1. Conclusions	87
7.2. Future works	88
Appendix A. The beam quality factor (M^2)	90
Appendix B. Ray transfer matrix analysis (ABCD matrix analysis)	91
Appendix C. The Sellmeier equation.....	92
Appendix D. The Kerr-lens mode locking sensitivity.....	94
Appendix E. Optical parametric generation.....	95

List of symbols and abbreviations

Symbols

E_{laser}	Energy of laser photon
E_{pump}	Energy of pump photon
λ_{laser}	Laser wavelength
λ_{pump}	Pump wavelength
$\Delta\lambda$	Spectral bandwidth
λ_{B}	Bragg wavelength
σ_{eff}	Effective emission cross-section
σ_{em}	Emission cross-section
σ_{abs}	Absorption cross-section
β	Ratio of excited ions to total number of ions
β_2	Group velocity dispersion
v_{g}	Group velocity
n	Refractive index
n_2	Nonlinear refractive index
n_{eff}	Effective refraction index
c	Speed of light in vacuum
I	Intensity
ω	Angular frequency
φ	Instantaneous phase
L	Length of propagation
Λ	Bragg grating period
T_{R}	Cavity round-trip time
A	Slowly varying pulse envelop
g	Saturated gain
G	Single-pass gain
D	Group delay dispersion
δ	SPM parameter

k	Wave number
Δk	Wave vector mismatch
d_{eff}	Effective nonlinear coefficient
ϵ_0	Electric permittivity of free space
τ_p	Pulse duration
f	Repetition rate
χ	Electric Susceptibility

Abbreviations

AR	Antireflection
BRF	Birefringent filter
CW	Continuous-wave
FWHM	Full-wave at half-maximum
GTI	Gires–Tournois interferometer
GDD	Group delay dispersion
GVM	Group velocity mismatch
HR	Highly reflecting
KLM	Kerr-lens mode locking
KLAS	Kerr-lens and saturable absorber
NA	Numerical aperture
OC	Output coupler
OPO	Optical parametric oscillator
QD-SESAM	Quantum-dot semiconductor saturable absorber mirror
QW-SESAM	Quantum-well semiconductor saturable absorber mirror
RF	Radio frequency
SAM	Self-amplitude modulation
SPM	Self-phase modulation
SESAM	Semiconductor saturable absorber mirror
Yb	Ytterbium
Sech^2	Hyperbolic secant function squared

List of figures

Figure 2.1. Schematic energy levels of Yb ³⁺ ions in Yb:KGW	13
Figure 2.2. Emission and absorption cross-sections of Yb:KGW along the principle refractive axes (courtesy of S. R. Bowman (Optical Sciences Division, U.S. Naval Research Laboratory))	14
Figure 2.3. The effect of GVD parameter on a pulse: (a) a transform-limited pulse, (b) the dispersed pulse after propagating through a medium with negative β_2 . The blue line is the electrical field, the red line is the pulse envelope.....	15
Figure 2.4. The effect of SPM on a pulse, (a) a transform-limited pulse, (b) the chirped pulse after propagating through a medium with positive n_2 . The blue line is the electrical field, the red line is the pulse envelope, the green line is the instantaneous frequency change	17
Figure 2.5. The Kerr lensing effect. The refractive index of the Kerr medium is modified in the presence of an intense laser beam	18
Figure 2.6. Pulse generation by means of loss modulation in a laser resonator	19
Figure 2.7. (a) SESAM on a copper heat sink and its schematic structure, (b) the reflectivity of a SESAM in terms of pulse fluence.....	20
Figure 2.8. Kerr lensing effect and spatial loss modulation in case of a hard-aperture mode locking (a) and soft-aperture mode locking of a laser (b).....	21
Figure 2.9. The laser model and contribution of SPM, GVD and SAM in pulse formation. GVD(+) is the positive dispersion, GVD(-) is the negative dispersion.....	23
Figure 3.1. Schematic of a birefringent filter plate	28
Figure 3.2. Experimental setup of a CW dual-wavelength Yb:KGW oscillator. AD, achromatic doublets; R1-3, concave mirrors; OC, output coupler. R1=300 mm, R2=300 mm, and R3=500 mm.....	29
Figure 3.3. Output power versus pump power for dual-wavelength laser with 5% output coupler. Insets: the beam intensity profile and laser spectrum at the highest pump power	31
Figure 3.4. (a) Average output power of dual-wavelength laser for different output couplers at the highest pump power of 27.9 W. Circles—experimental data points; solid line is for the eye guide only. (b) Wavelengths of oscillating modes for different output couplers.	32
Figure 4.1. Experimental setup of a mode-locked Yb:KGW laser. AD, achromatic doublet; DM, dichroic mirror; R1-3, concave mirror; OC, output coupler. R1=300 mm, R2=300 mm, R3=500 mm	38
Figure 4.2. (a) The spectrum of the generated pulses with 0.7% QD-SESAM and (b) intensity autocorrelation. The red curves are the <i>sech</i> ² shape fits. The time-bandwidth product	

was calculated to be 0.317. The ripple in the spectrum is a known artifact of the spectrometer	39
Figure 4.3. (a) RF spectrum of the pulse train with 0.7% QD-SESAM, (b) wide-span measurements. (c) Far-field beam intensity profile of the mode-locked laser RBW: resolution bandwidth.....	40
Figure 4.4. (a) Intensity autocorrelation of the mode-locked laser. Inset: wide-range scan (200 ps). (b) Spectrum of the mode-locked laser (black dotted curve), the calculated round-trip GDD (blue dotted curve) and the dispersive function $D(\lambda)$ (upper graph). The $sech^2$ -shape fits are shown as red solid curves.....	41
Figure 4.5. Radio-frequency spectral power of the mode-locked laser. (a) Fundamental harmonic and (inset) wide-span measurement. RBW: resolution bandwidth	42
Figure 4.6. Current and previous mode-locked laser results with QD-SESAMs [12,14,17].....	45
Figure 4.7. A comparison of sub-100 fs diode-pumped bulk Yb-doped crystal lasers [9,10,22,23,38–43,48]. Data from Ref. [18] are not shown for scaling reasons to better visualize the <90 fs regime. SA: SESAM.....	47
Figure 5.1. Experimental setup of Kerr-lens mode-locked Yb:KGW laser. AD, achromatic doublets; DM: dichroic mirror; R1-3: concave mirrors; OC: output coupler. R1=300 mm, R2=300 mm and R3=500 mm.....	54
Figure 5.2. (a) Intensity autocorrelation of the mode-locked laser with CW component. (b) The corresponding mode-locked laser spectrum. The $sech^2$ -shape fits are shown as red solid curves.....	55
Figure 5.3. (a) Intensity autocorrelation of 240 fs pulse. Inset: wide-range scan of 200 ps. (b) The corresponding mode-locked laser spectrum. (c) Radio frequency spectral power. Inset: the wide-span RF measurement. The $sech^2$ -shape fits are shown as red solid curves. RBW: resolution bandwidth	56
Figure 5.4. (a) Intensity autocorrelation of 120 fs pulse. Inset: wide-range scan of 200 ps. (b) The corresponding mode-locked laser spectrum. (c) Radio frequency spectral power. Inset: the wide-span RF measurement. The $sech^2$ -shape fits are shown as red solid curves. RBW: resolution bandwidth	57
Figure 5.5. (a) The Kerr sensitivity map. Contours show negative sensitivity values. The red spot shows the operating point of the mode-locked laser.....	59
Figure 5.6. (a) Thermal conductivity and emission bandwidth of the Yb-doped crystals [7,25–30,35–38]. (b) Comparison of femtosecond Kerr-lens mode-locked lasers based on bulk Yb-ion doped crystals in terms of average output power and pulse duration. R: Ring cavity, HA: Hard-aperture mode-locked laser [1–9,14–16,29–34]. The hollow symbols show lasers excited with high beam quality ($M^2 \leq 3$) pump sources.....	61
Figure 6.1. Optical parametric oscillator pumped by a frequency-doubled mode-locked laser ...	67
Figure 6.2. The refractive index profiles and the group velocities versus the wavelength at room temperature.....	71

Figure 6.3. Angle tuning curves in BBO (a), LBO (B) and BIBO (c) crystals at room temperature with an effective nonlinearity coefficient d_{eff} . Idler—black curve, signal—red.....	73
Figure 6.4. Temperature tuning curves in LBO (a) and BIBO (b) crystals with corresponding effective nonlinearity coefficients d_{eff} . Idler—black curve, signal—red	74
Figure 6.5. Angular walk-off versus wavelength in BBO and BIBO crystals.....	75
Figure 6.6. Group velocity mismatch between the pump, signal and idler in BIBO (a), BBO (b), and LBO (c) crystals	77
Figure 6.7. Group velocity dispersion vs. signal wavelength	78
Figure 6.8. The gain bandwidth versus the signal wavelength for LBO, BBO and BIBO crystals. The solid lines show the first derivative of the bandwidth approximation and the dashed lines show the second derivative around the degeneracy.....	80
Figure E.1. Uniaxial crystal (a) and biaxial crystal (b); \vec{k} defines the propagation direction of a wave (i, p, s); \hat{e} and \hat{o} are unit vectors of possible polarization state of the wave; the intersecting curves in (b) define the values of the refractive indices for a wave (\vec{k}), given by the Fresnel's equation.....	96

List of tables

Table 1.1. Optical properties of some Yb-doped laser crystals and Ti:sapphire for femtosecond pulse generation [25].....	3
Table 4.1. Summary of the mode-locked Yb:KGW laser performance.....	44
Table 5.1. Summary of the KLM laser performance	58
Table 6.1. Optical properties of BBO, BIBO and LBO crystals.....	72

Chapter 1

Introduction

1.1. Introduction

The invention of a laser in early 1960 [1] opened up new horizons to many applications where coherent optical sources are required. Nowadays, a variety of laser sources cover the optical range of electromagnetic spectrum from the ultraviolet to far-infrared in the form of continuous-wave or pulsed laser radiation. The pulsed laser source delivers optical bursts that confine the energy in time periods ranging from milliseconds to a few femtoseconds (1 femtosecond= 1×10^{-15} s). The ultra-short laser pulses specifically refer to optical pulses with the duration of 10^{-15} s to 10^{-12} s and they are characterized by high peak power and broad spectrum. The peak power of these pulses can be extremely high, from kilowatts to terawatts, while the average power can be at the moderate levels, i.e. milliwatts to watts.

Ultra-short pulses with high peak power are used to stimulate nonlinear processes such as in multi-photon imaging [2,3]. In multi-photon microscopy, nonlinear absorption occurs at a focal point of the laser beam and results in emission of fluorescence from the imaged sample. Different substances in the sample exhibit fluorescence with distinct decay rates, making it possible to map the structure of the sample. It has been shown that the application of femtosecond pulses increases the resolution and penetration depth of imaging due to its higher peak power when compared with the longer pulses with picosecond (10^{-12} s) duration [4]. In surgical and ablation applications, the exploitation of femtosecond pulses improves the precision and reduces the secondary damage such as shock waves and cavitation bubbles [5,6].

Another feature of femtosecond laser pulses is their broad spectrum which is suitable for applications such as optical coherence tomography (OCT). Being widely used in ophthalmology, OCT uses a short pulse of coherent light source. It relies on its interference with the reflected light from different layers within the sample in order to create the image. The axial resolution of OCT imaging technique is inversely related to its spectral bandwidth [7] and a femtosecond laser can be

an ideal light source for this technique [8,9]. The broad spectral bandwidth of femtosecond laser pulses can also be utilized for wavelength division multiplexing by slicing the spectrum into several spectral channels for telecommunication applications [10,11]. Furthermore, high peak power femtosecond laser pulses can be employed to generate even broader spectrum by passing through a highly nonlinear optical medium so as to generate a broadband white-light or supercontinuum. Such a broadband light is an attractive light source for characterization of the absorptive and scattering properties of a specimen such as in coherent anti-Stokes Raman scattering spectroscopy and infrared spectroscopy [12,13].

1.2. Motivation

For many years, the Ti:sapphire laser has been a workhorse for a wide range of applications [9,14-16]. It is possible to generate ultra-short pulses with duration of a few femtoseconds or widely tune the wavelength of a somewhat longer pulses owing to the extraordinary broad gain bandwidth of a Ti:sapphire crystal [17,18]. However, the efficiency of Ti:sapphire laser system is low and it is also required to use another laser system for pumping the Ti:sapphire laser, typically an Argon-ion laser or a frequency-doubled Nd:YVO₄ laser [19,20]. Only recently, direct laser diode pumping was proposed for a Ti:sapphire laser with low power InGaN and GaN laser diodes [21-23]. For some applications the generated pulses are required to undergo an external amplification by using complicated and costly systems such as chirped-pulse amplifier or regenerative amplifier so as to acquire the necessary peak power and energy [14,24]. Because of the high level of complexity and cost of these laser systems, the generation of ultra-short pulses with high power and energy based on the other laser materials is of interest. New laser materials are being developed and some are commercially available, but only a few of them have the potential to rival the Ti:sapphire laser for high power sub-100 fs pulse regime of operation. The Ytterbium (Yb)-doped laser crystals with higher quantum efficiency than Ti:sapphire, relatively large gain bandwidth (for supporting sub-100 fs pulses) and thermal conductivity (for high power operation) are suitable candidates for watt-level output power regime. In addition, the wavelength of the maximum absorption at 980 nm in the Yb-doped materials facilitates the use of the efficient high power InGaAs diode lasers as the pumping source. A comparison of properties of the selected Yb-doped laser crystals and Ti:sapphire crystal is presented in Table.1.1.

Table 1.1. Optical properties of some Yb-doped laser crystals and Ti:sapphire for femtosecond pulse generation [25].

Material	Emission bandwidth (FWHM)*	Central emission wavelength	Thermal conductivity (W.K ⁻¹ .m ⁻¹)	High power diode laser pumping
Ti:sapphire	180 nm	790 nm	34	No
Yb:YAG	9 nm	1031 nm	11	Yes
Yb:CALGO	80 nm	1050 nm	6.9	Yes
Yb:KGW	25 nm	1030 nm	3.3	Yes

*FWHM: full width at half maximum

In high power regime of operation, thin disk laser (TDL) systems offer exceptional performance [26]. However, the thin disk lasers have the disadvantage of high cost, complexity of the laser system and pumping geometry as well as the difficulty of the thin disk gain medium fabrication.

Comparing the bulk lasers with fiber lasers oscillators, the bulk lasers are capable of generating high peak power ultra-short pulses directly from the oscillator, while all-fiber laser oscillators usually deliver longer pulses with considerably lower output power [27]. This happens because of the destabilization of the mode locking process caused by the strong nonlinear effects induced by ultra-short pulses due to the extreme confinement of the radiation in a fiber core over long distances. In this case, external amplification of the laser pulses is required [28]. On the other hand, high power performance of a fiber laser oscillator is only possible in normal-dispersion regime where highly chirped pulses with nanosecond/picosecond pulse widths are generated. Therefore, external compression of such pulses is required [29].

Among the bulk lasers, exceptional performance were recently demonstrated for Yb:CALGO and Yb:CaF₂ laser crystals for generating high power sub-100 fs pulse. These crystals possess relatively high thermal conductivity and broad gain bandwidth and the generation of 94 fs pulses with 12.5 W of average output power in Yb:CALGO and 48 fs pulses with 2.7 W of power in Yb:CaF₂ were reported [30,31]. Furthermore, the spectra of femtosecond pulses generated based on the Yb:YAG crystals have reached the full available gain bandwidth of this crystal in the low output power regime [32] as well as in high power regime in a thin disk laser [33].

The commercially available crystal of Yb:KGW is another suitable candidate for sub-100 fs pulse generation with watt-level output power. The full-width at half-maximum (FWHM) gain bandwidth of a Yb:KGW laser crystal is around 25 nm and the theoretical pulse duration of 45 fs can be supported. In addition, the crystal thermal conductivity coefficient is around $3.3 \text{ W.K}^{-1}.\text{m}^{-1}$ which is suitable for high power regime. However its potential in terms of the available spectral gain bandwidth and high power operation has not been fully exploited yet. For instance, the shortest pulse duration generated in Yb:KGW was 59 fs (20.2 nm pulse spectral bandwidth) with only 62 mW of output power [34]. Higher power regime has been demonstrated for longer pulses of 162 fs with 8.8 W of average output power [35] and 290 fs pulses with 10 W of average power [36]. Recently, the generation of 67 fs pulse with 3 W of average output power in a diode-pumped Yb:KGW laser was reported [37]. Based on these facts, enhancement in the performance of Yb:KGW laser in the watt-level sub-100 fs regime of operation was the main motivation of this work.

1.3. Objective

The prime objective of this thesis was to develop a compact and simple laser system based on a diode-pumped Yb:KGW laser crystal which delivers watt-level sub-100 femtosecond pulses directly from the laser oscillator. The major challenges of generating sub-100 fs pulses with high average power are the thermal lensing effect in the laser crystal [38,39] and the enhanced nonlinear effects [40] that should be compensated for. Because of these factors many of the proposed laser oscillators could deliver either ultrashort pulses with relatively low power limited to several hundreds of milliwatts or watt-level long pulses with duration well above 100 fs.

By increasing the pump power for achieving higher laser output power, the thermal load in the crystal increases and leads to a strong thermal lensing effect by altering the refractive index of the crystal and creating a mechanical stress, which considerably affects the laser performance or even stability. The deposited heat can also result in thermal damage of the crystal and needs to be dissipated by using a cooling system. Since the thermal conductivity of bulk laser crystals is restricted, most of the reported femtosecond lasers were limited to low power regime. One solution would be using a thin disk laser gain medium which facilitates the removal of heat and reduces the thermal lensing effect, but it requires a complicated pumping geometry and manufacturing of a

fragile thin disk gain medium [41]. Therefore, one important feature of the laser crystal should be its relatively high thermal conductivity and the thermal lensing effect should be considered in the laser cavity design.

Another challenge is to control the enhanced nonlinear effect such as self-phase modulation and nonlinear phase shift in the cavity as a result of high peak power of the pulse. Since the pulse generation is governed by a nonlinear laser dynamics, the increased nonlinearity can destabilize the laser system and result in the pulse break-up [42,43]. Therefore, it is crucial to compensate for these effects and control the intra-cavity power in order to maintain a stable pulse generation at high power levels.

From the perspective of system design, the laser needs to be simple and compact with limited number of optical components. The ultrashort pulse generation with high power directly from an oscillator implies the elimination (or simplification) of external amplification. Such a system also requires a compact pumping source such as the compact and efficient InGaAs diode lasers. However, diode lasers come with a compromised beam quality factor and divergence.

To achieve this aim, the crystal of Yb:KGW was chosen as the laser gain medium. It is a suitable candidate owing to its relatively large gain bandwidth (25 nm) for sub-100 fs pulse generation and thermal conductivity ($3.3 \text{ W.K}^{-1}.\text{m}^{-1}$) for watt-level operation. This laser crystal is commercially available with customized geometry and doping level. In addition, a cost-effective and compact InGaAs diode laser can be used as the pumping source for the laser system, which is capable of delivering up to 30 W of output power at 980 nm. Accompanied with numerical analysis, two well-established techniques were employed for generating the ultra-short laser pulses, namely a semiconductor saturable absorber mode locking and the Kerr-lens mode locking. A newly developed type of semiconductor saturable absorber (quantum-dot semiconductor saturable absorber mirror) was used for this work. All of the concerns mentioned above had to be addressed accordingly.

1.4. Thesis contribution

This thesis presents the results on high power ultra-short pulse generation based on the diode-pumped Yb:KGW lasers using two well-established techniques, i.e., the saturable absorber mode

locking and Kerr-lens mode locking (KLM). Newly developed saturable absorbers, i.e., quantum-dot saturable absorber mirrors (QD-SESAM) were used and the results favourably compared with the preceding experiments in terms of average output power, pulse duration and peak power. A pure Kerr-lens mode-locked Yb:KGW laser was also demonstrated for the first time with a multimode fibre-coupler laser diode for pumping, which delivered watt-level ultra-short pulses. Besides, a high power continuous-wave dual-wavelength operation of Yb:KGW laser with improved efficiency using an original solution was also reported. In the following the key point contributions of this thesis are presented:

- The generation of 90 fs pulses with 3.2 W of power (462 kW of peak power and 41 nJ of energy) based on the hybrid action of quantum-dot saturable absorber mirror and Kerr lensing effect. The results exhibited significant increase in pulse energy and pulse peak power when compared with the previous works based on quantum-dot saturable absorber mirror. The developed laser was one of the highest power sub-100 fs pulse systems among the Yb-doped lasers. The results were published in Optics Letters journal: R. Akbari, H. Zhao, K. A. Fedorova, E. U. Rafailov, and A. Major, "*Quantum-dot saturable absorber and Kerr-lens mode-locked Yb:KGW laser with >450 kW of peak power,*" Opt. Lett. 41, 3771 (2016).
- The generation of 56 fs pulses with 1.95 W of output power based on dual action of quantum-dot saturable absorber mirror and Kerr lensing effect. These pulses were the shortest ones ever generated from the monoclinic double tungstate laser crystals (and Yb:KGW in particular) and also the most powerful ones in the sub-60 fs regime. The results were published in Applied Physics B journal: R. Akbari, K. A. Fedorova, E. U. Rafailov, and A. Major, "*Diode-pumped ultrafast Yb:KGW laser with 56 fs pulses and multi-100 kW peak power based on SESAM and Kerr-lens mode locking,*" Appl. Phys. B 123, 123 (2017).
- The demonstration of a high power and high efficiency CW dual-wavelength Yb:KGW laser. A stable dual-wavelength operation at 1014.6 nm and 1041.3 nm with 3.4 W of output power was achieved. It presented an improvement of more than an order of magnitude in output power and higher efficiency when compared to previous results, while using a significantly simpler laser design. The results were published in Optics Letters journal: R. Akbari, H.

Zhao, and A. Major, "*High-power continuous-wave dual-wavelength operation of a diode-pumped Yb:KGW laser*," Opt. Lett. 41, 1601 (2016).

- The demonstration of watt-level pure Kerr-lens mode locking of a Yb:KGW laser pumped by a multimode fibre-coupled laser diode for the first time. The laser delivered 240 fs pulses with 2.3 W of average output power at 86.8 MHz, corresponding to 110 kW of peak power and 26 nJ of pulse energy. The shortest generated pulse duration was 120 fs with 1.2 W of output power. These results were the first demonstration of watt-level KLM bulk laser pumped by a multimode laser diode. The results were submitted for publication to Applied Optics journal.
- The analysis of optical parametric oscillators (OPO) based on the nonlinear crystals of BIBO, BBO and LBO pumped by a frequency-doubled femtosecond Yb:KGW laser. Based on this analysis a compact widely-tunable ultrafast oscillator can be developed which can be pumped by the demonstrated femtosecond Yb:KGW lasers. The results of this work were published in Laser Physics journal: R. Akbari and A. Major, "*Optical, spectral and phase-matching properties of BIBO, BBO and LBO crystals for optical parametric oscillation in the visible and near-infrared wavelength ranges*," Laser Phys. 23, 035401 (2013).

1.5. Thesis outline

In chapter 2, a brief introduction of Yb:KGW laser crystal and its optical properties is presented. Then, the optical effects, including group-velocity dispersion and optical Kerr effect, which contribute to the ultrashort pulse formation are introduced. Next, the general concept of mode locking of a laser as the mechanism for generation of femtosecond laser pulses is reviewed. This section is followed by introducing two methods for mode locking of a laser, namely mode locking by using a saturable absorber mirror and the Kerr-lens mode locking. The potential of the combination of these methods is also highlighted. A general description of interplay between the nonlinear optical effects and pulse formation mechanism is provided in the next section.

Chapter 3 is devoted to the results of a continuous-wave dual-wavelength Yb:KGW laser experiment. This experiment was performed at the stage of establishing a continuous-wave laser. The theoretical background of generating dual-wavelength laser by using a birefringent filter plate and a review of the preceding works are represented. Then, the experimental setup is explained and the results are discussed. The superior features of our results are highlighted in the conclusion.

In chapter 4, the results of a femtosecond mode-locked Yb:KGW laser based on dual-action of quantum-dot saturable absorber mirror and Kerr-lens effect are presented. After a concise introduction and literature review, the experimental setup for two sets of experiments is explained. These experiments resulted in the generation of high power sub-100 mode-locked lasers. The results are compared with the previous works and enhancements are highlighted.

Chapter 5 presents the results of the first watt-level pure Kerr-lens mode-locked Yb:KGW laser, pumped by a multimode fibre-coupled diode. Beginning with a review of the previous works on Kerr-lens mode-locked lasers with different Yb-doped crystals and pumping sources, the experiment is explained and results are presented. A comparison is provided with all of the bulk KLM lasers based on the Yb-doped laser crystals and future improvements are discussed.

In chapter 6, the results of simulation of optical parametric oscillators based on the nonlinear crystals of BIBO, BBO and LBO pumped by a frequency-doubled femtosecond Yb:KGW laser are presented. A detailed introduction on these crystals is provided. The optical properties are summarized and efficient phase-matching conditions are investigated in the following sections. Dispersive and spectral properties are also investigated and the most efficient conditions are discussed. The results of these simulations can be considered as a future work for the laser demonstrated in the previous chapters.

Finally, in chapter 7 a summary of the achievements of this thesis is provided and possible improvements are suggested. Future works for each part of this thesis are also proposed.

References

1. T. H. Maiman, "Stimulated Optical Radiation in Ruby," *Nature* **187**, 493–494 (1960).
2. W. R. Zipfel, R. M. Williams, and W. W. Webb, "Nonlinear magic: multiphoton microscopy in the biosciences," *Nat. Biotechnol.* **21**, 1369–1377 (2003).
3. D. Kobat, M. E. Durst, N. Nishimura, A. W. Wong, C. B. Schaffer, and C. Xu, "Deep tissue multiphoton microscopy using longer wavelength excitation," *Opt. Express* **17**, 13354 (2009).
4. M. Oheim, E. Beaurepaire, E. Chaigneau, J. Mertz, S. Charpak, "Two-photon microscopy in brain tissue: parameters influencing the imaging depth." *Journal of neuroscience methods* **111.1**, 29-37 (2001).
5. T. Juhasz, G. A. Kastis, C. Suárez, Z. Bor, and W. E. Bron, "Time-resolved observations of shock waves and cavitation bubbles generated by femtosecond laser pulses in corneal tissue and water," *Lasers Surg. Med.* **19**, 23–31 (1996).
6. T. Juhasz, F. H. Loesel, R. M. Kurtz, C. Horvath, J. F. Bille, and G. Mourou, "Corneal refractive surgery with femtosecond lasers," *IEEE J. Sel. Top. Quantum Electron.* **5**, 902–910 (1999).
7. J. G. Fujimoto, A. D. Aguirre, Y. Chen, P. R. Herz, P.-L. Hsiung, T. H. Ko, N. Nishizawa, and F. X. Kärtner, "Ultrahigh-Resolution Optical Coherence Tomography Using Femtosecond Lasers," in *Ultrashort Laser Pulses in Biology and Medicine*, M. Braun, P. Gilch, and W. Zinth, eds. (Springer Berlin Heidelberg, 2008), pp. 3–27.
8. B. E. Bouma, G. J. Tearney, I. P. Bilinsky, B. Golubovic, and J. G. Fujimoto, "Self-phase-modulated Kerr-lens mode-locked Cr:forsterite laser source for optical coherence tomography," *Opt. Lett.* **21**, 1839 (1996).
9. W. Drexler, U. Morgner, F. X. Kärtner, C. Pitris, S. a Boppart, X. D. Li, E. P. Ippen, and J. G. Fujimoto, "In vivo ultrahigh-resolution optical coherence tomography," *Opt. Lett.* **24**, 1221 (1999).
10. Y. J. Chai, C. G. Leburn, A. a. Lagatsky, C. T. a. Brown, R. V. Pentyl, I. H. White, and W. Sibbett, "1.36-Tb/s spectral slicing source based on a Cr⁴⁺-YAG femtosecond laser," *J. Light. Technol.* **23**, 1319–1324 (2005).
11. E. A De Souza, M. C. Nuss, W. H. Knox, and D. A. B. Miller, "Wavelength-division multiplexing with femtosecond pulses," *Opt. Lett.* **20**, 1166 (1995).
12. H. Kano and H. Hamaguchi, "Femtosecond coherent anti-Stokes Raman scattering spectroscopy using supercontinuum generated from a photonic crystal fiber," *Appl. Phys. Lett.* **85**, 4298 (2004).
13. J. Mandon, E. Sorokin, I. T. Sorokina, G. Guelachvili, and N. Picqué, "Supercontinua for high-resolution absorption multiplex infrared spectroscopy," *Opt. Lett.* **33**, 285 (2008).
14. F. H. Loesel, J. P. Fischer, M. H. Götz, C. Horvath, T. Juhasz, F. Noack, N. Suhm, and J. F. Bille, "Non-thermal ablation of neural tissue with femtosecond laser pulses," *Appl. Phys. B Lasers Opt.* **66**, 121–128 (1998).
15. S. Nolte, C. Momma, H. Jacobs, A. Tünnermann, B. N. Chichkov, B. Wellegehausen, and H. Welling, "Ablation of metals by ultrashort laser pulses," *J. Opt. Soc. Am. B* **14**, 2716 (1997).
16. R. a Farrer, M. J. R. Prevede, C. E. Olson, L. A. Peyser, J. T. Fourkas, and P. T. C. So, "Single-molecule detection with a two-photon fluorescence microscope with fast-scanning capabilities and polarization sensitivity," *Opt. Lett.* **24**, 1832 (1999).
17. R. Ell, U. Morgner, F. X. Kärtner, J. G. Fujimoto, E. P. Ippen, V. Scheuer, G. Angelow, T. Tschudi, M. J. Lederer, A. Boiko, and B. Luther-Davies, "Generation of 5-fs pulses and

- octave-spanning spectra directly from a Ti:sapphire laser," *Opt. Lett.* **26**, 373 (2001).
18. P. G. Antal and R. Szipócs, "Tunable, low-repetition-rate, cost-efficient femtosecond Ti:sapphire laser for nonlinear microscopy," *Appl. Phys. B* **107**, 17–22 (2012).
 19. M. T. Asaki, C.-P. Huang, D. Garvey, J. Zhou, H. C. Kapteyn, and M. M. Murnane, "Generation of 11-fs pulses from a self-mode-locked Ti:sapphire laser," *Opt. Lett.* **18**, 977 (1993).
 20. A. M. Kowalewicz, Jr., a T. Zare, F. X. Kärtner, J. G. Fujimoto, S. Dewald, U. Morgner, V. Scheuer, and G. Angelow, "Generation of 150-nJ pulses from a multiple-pass cavity Kerr-lens mode-locked Ti:Al₂O₃ oscillator," *Opt. Lett.* **28**, 1597 (2003).
 21. C. G. Durfee, T. Storz, J. Garlick, S. Hill, J. a Squier, M. Kirchner, G. Taft, K. Shea, H. Kapteyn, M. Murnane, and S. Backus, "Direct diode-pumped Kerr-lens mode-locked Ti:sapphire laser," *Opt. Express* **20**, 13677 (2012).
 22. S. Sawai, A. Hosaka, H. Kawauchi, K. Hirosawa, and F. Kannari, "Demonstration of a Ti:sapphire mode-locked laser pumped directly with a green diode laser," *Appl. Phys. Express* **7**, 22702 (2014).
 23. P. W. Roth, A. J. Maclean, D. Burns, and A. J. Kemp, "Direct diode-laser pumping of a mode-locked Ti:sapphire laser," *Opt. Lett.* **36**, 304 (2011).
 24. K. Kuemeyer, G. Kensah, M. Heidrich, H. Meyer, U. Martin, I. Gruh, and A. Heisterkamp, "Two-photon induced collagen cross-linking in bioartificial cardiac tissue," *Opt. Express* **19**, 15996 (2011).
 25. F. Druon, F. Balembois, and P. Georges, "New laser crystals for the generation of ultrashort pulses," *Comptes Rendus Phys.* **8**, 153–164 (2007).
 26. C. J. Saraceno, F. Emaury, O. H. Heckl, C. R. E. Baer, M. Hoffmann, C. Schriber, M. Golling, T. Südmeyer, and U. Keller, "275 W average output power from a femtosecond thin disk oscillator operated in a vacuum environment," *Opt. Express* **20**, 23535 (2012).
 27. I. Harti, G. Imeshev, L. Dong, G. C. Cho and M. E. Fermann, "Ultra-compact dispersion compensated femtosecond fiber oscillators and amplifiers," (CLEO). Conference on Lasers and Electro-Optics, pp. 1641-1643 (2005).
 28. T. Eidam, S. Hanf, E. Seise, T.V. Andersen, T. Gabler, C. Wirth, T. Schreiber, J. Limpert, and A. Tünnermann, "Femtosecond fiber CPA system emitting 830 W average output power," *Opt. Lett.* **35**, 94-96 (2010)
 29. K. Kieu, W. Renninger, A. Chong, and F. Wise, "Sub-100 fs pulses at watt-level powers from a dissipative-soliton fiber laser," *Opt. Lett.* **34**, 593-595 (2009).
 30. A. Greborio, A. Guandalini, and J. Aus der Au, "Sub-100 fs pulses with 12.5-W from Yb:CALGO based oscillators," in SPIE proceedings **8235**, p. 823511 (2012).
 31. P. Sevillano, G. Machinet, R. Dubrasquet, P. Camy, J.-L. Doualan, R. Moncorge, P. Georges, F. P. Druon, D. Descamps, and E. Cormier, "Sub-50 fs, Kerr-lens mode-locked Yb:CaF₂ laser oscillator delivering up to 2.7 W," in Advanced Solid-State Lasers Congress (OSA, 2013), p. AF3A.6.
 32. Y. Sasatani, H. Hitotsuya, S. Matsubara, M. Inoue, Y. Ishida, N. Shimojo, and S. Kawato, "Ultrashort-Pulse Generation Close To the Fluorescence Spectrum Limit of the Gain Material in Mode-Locked Yb:YAG Laser With Semiconductor Saturable Absorber," *Int. J. Latest Res. Sci. Technol.* **1**, 334–336 (2012).
 33. J. Zhang, J. Brons, M. Seidel, D. Bauer, D. Sutter, V. Pervak, V. Kalashnikov, Z. Wei, A. Apolonski, F. Krausz, and O. Pronin, "Generation of 49-fs pulses directly from distributed Kerr-lens mode-locked Yb:YAG thin-disk oscillator," in Advanced Solid State Lasers (OSA,

- 2015), Vol. 1, p. ATh4A.7.
34. M. Kowalczyk, J. Sotor, and K. M. Abramski, "59 fs mode-locked Yb:KGW oscillator pumped by a single-mode laser diode," *Laser Phys. Lett.* **13**, 35801 (2016).
 35. V. E. Kisel, A. S. Rudenkov, A. A. Pavlyuk, A. A. Kovalyov, V. V. Preobrazhenskii, M. A. Putyato, N. N. Rubtsova, B. R. Semyagin, and N. V. Kuleshov, "High-power, efficient, semiconductor saturable absorber mode-locked Yb:KGW bulk laser," *Opt. Lett.* **40**, 2707 (2015).
 36. G. R. Holtom, "Mode-locked Yb:KGW laser longitudinally pumped by polarization-coupled diode bars," *Opt. Lett.* **31**, 2719 (2006).
 37. H. Zhao and A. Major, "Powerful 67 fs Kerr-lens mode-locked prismless Yb:KGW oscillator," *Opt. Express* **21**, 31846 (2013).
 38. S. Chénais, F. Druon, S. Forget, F. Balembois, and P. Georges, "On thermal effects in solid-state lasers: The case of ytterbium-doped materials," *Prog. Quantum Electron.* **30**, 89–153 (2006).
 39. D. Stučinskas, R. Antipenkov, and A. Varanavičius, "Thermal lensing in high-power diode-pumped Yb:KGW laser," *Lith. J. Phys.* **50**, 191–199 (2010).
 40. W. H. Renninger and F. W. Wise, "Fundamental Limits to Mode-Locked Lasers: Toward Terawatt Peak Powers," *IEEE J. Sel. Top. Quantum Electron.* **21**, 63–70 (2015).
 41. T. Südmeyer, C. Kränkel, C. R. E. Baer, O. H. Heckl, C. J. Saraceno, M. Golling, R. Peters, K. Petermann, G. Huber, and U. Keller, "High-power ultrafast thin disk laser oscillators and their potential for sub-100-femtosecond pulse generation," *Appl. Phys. B* **97**, 281–295 (2009).
 42. M. Lai, J. Nicholson, and W. Rudolph, "Multiple pulse operation of a femtosecond Ti:sapphire laser," *Opt. Commun.* **142**, 45–49 (1997).
 43. V. L. Kalashnikov, E. Sorokin, and I. T. Sorokina, "Multipulse operation and limits of the Kerr-lens mode-locking stability," *IEEE J. Quantum Electron.* **39**, 323–336 (2003).

Chapter 2

Theory and background

2.1. Introduction

In this chapter, the properties of the chosen laser gain material, Ytterbium-doped potassium-gadolinium tungstate (Yb:KGW or Yb:KGd(WO₄)₂), are reviewed. A review of the optical effects that are involved in pulse formation in a laser cavity, including group-velocity dispersion (GVD), self-phase modulation (SPM) effect and the Kerr lensing effect is provided. The general concept of a mode-locked laser for generating ultra-short laser pulses is introduced, followed by a review of the two techniques for femtosecond pulse generation, namely mode locking by a semiconductor saturable absorber and the Kerr-lens mode locking. The properties of a quantum-dot saturable absorber mirror are also highlighted. Finally, the nonlinear dynamics of pulse formation in a laser system and the role of these parameters are briefly reviewed.

2.2. Laser material: Yb:KGW

The Rare-Earth metal ions doped crystals are commonly used for generating laser radiation due to their fairly long upper state lifetime, sharp fluorescent lines and strong absorption bands. Among them, Ytterbium-doped laser crystals are favorable laser gain media because of their advantageous properties. First, they possess simple energy level structure which consists of only two main electronic manifolds for the laser transition from ²F_{5/2} to ²F_{7/2}, as shown in figure 2.1 for the Yb:KGW laser crystal. This simple structure eliminates undesired loss effects such as up-conversion excitation, excited-state absorption and concentration quenching [1]. Second, Yb-doped crystals also exhibit low quantum defect ($E_{\text{laser}}/E_{\text{pump}} = \lambda_{\text{pump}}/\lambda_{\text{laser}} \approx 0.95$) which results in low thermal load in the crystal when it is excited. Third, there is a strong absorption cross-section between 940 nm and 980 nm in the Yb-doped crystals that makes it possible to use efficient and compact InGaAs laser diodes as the pump source for the laser system.

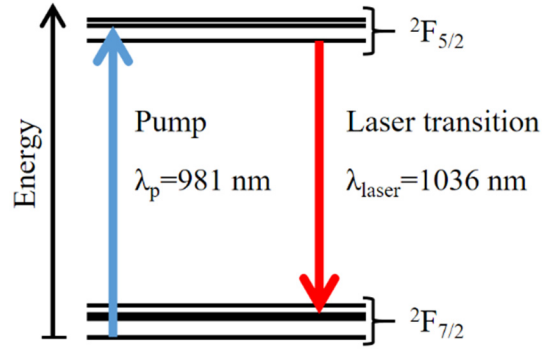


Figure 2.1. Schematic energy levels of Yb^{3+} ions in Yb:KGW.

However, there are undesired characteristics in the Yb-doped crystals as well. The lower energy level for laser transition is near the ground energy level and thus is thermally populated at room temperature. This results in re-absorption of the generated laser radiation and as a result the laser crystal operates in a quasi-three-level regime. This is characterized by a considerable overlap between the absorption cross-section and emission cross-section profiles of the Yb-doped crystals. Furthermore, fairly long fluorescence lifetime of the excited ions in Yb-doped crystals favors Q-switching instability in case of short pulse laser generation, since large amount of energy is stored in the upper energy level over the time, which is much longer than the produced pulse duration [1].

Among the Yb-doped crystals, the crystal of Yb:KGW exhibits high emission cross-section ($2.8 \times 10^{-20} \text{ cm}^2$), broad amplification bandwidth ($\sim 25 \text{ nm}$) and relatively high thermal conductivity ($3.3 \text{ W.K}^{-1}.\text{m}^{-1}$) [2], all of which make it a suitable laser gain medium for generating high power ultra-short laser pulses and widely-tunable laser radiation with the help of an optical parametric oscillator (OPO) [3]. The emission and absorption cross-sections of Yb:KGW crystal for the principal axes are shown in figure 2.2.

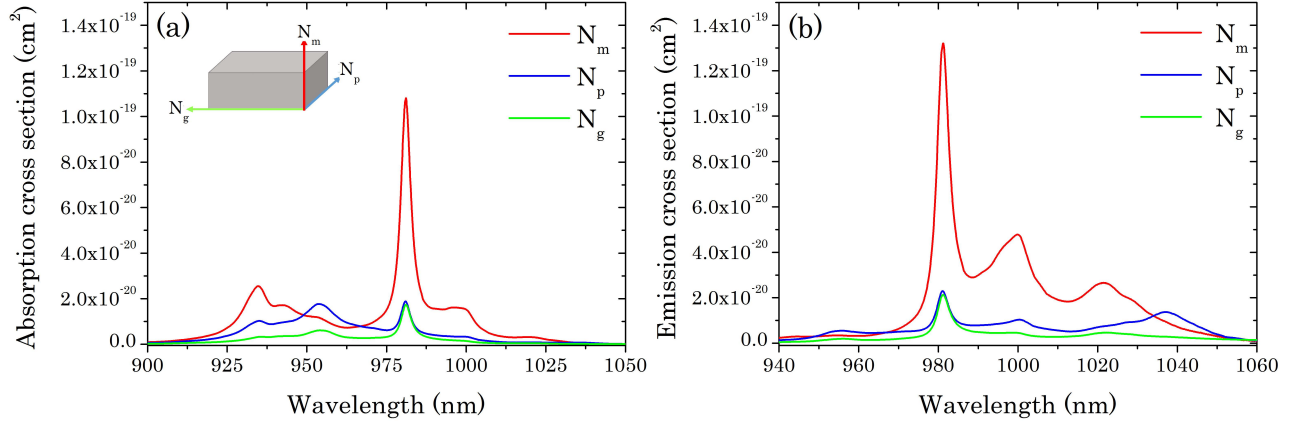


Figure 2.2. Emission and absorption cross-sections of Yb:KGW along the principle refractive axes (courtesy of S. R. Bowman (Optical Sciences Division, U.S. Naval Research Laboratory)).

As a result of the re-absorption loss, the effective emission cross-section of a laser gain medium is expressed as [4]

$$\sigma_{eff} = \beta\sigma_{em} - (1 - \beta)\sigma_{ab} \quad \text{Eq. 2.1}$$

where β is the ratio of the excited Yb ions to the total number of Yb ions in the gain medium. This ratio depends on the net-laser cavity loss and it changes for different output coupling transmission. Therefore, the effective gain profile reshapes which affects the maximum effective gain, its peak wavelength and the available spectral gain bandwidth.

The crystal is usually cut along the N_g-axis and a pump light experiences strong absorption for polarization along the N_m-axis with the largest absorption cross-section at 980 nm. The laser light is usually polarized along the N_m-axis due to its large gain. The N_m-axis exhibits larger gain with the corresponding peak wavelength lying at shorter wavelength range when compared with the N_p-axis, while the N_p-axis has a broader gain bandwidth at longer wavelengths [5]. In addition, an N_g-cut Yb:KGW crystal exhibits the lowest degree of beam astigmatism in high power regime, where the thermal lensing is usually strong [6].

2.3. Group-velocity dispersion (GVD)

The refractive index of an optical medium is a wavelength-dependent parameter. Therefore, the constituent wavelengths of a light pulse with broad spectrum experience different phase velocities which results in dispersion of the pulse envelope. The dispersion parameter can be defined as [7,8]

$$\beta_2 = \frac{d}{d\omega} \left(\frac{1}{v_g(\omega)} \right) = \frac{\lambda^3}{2\pi c^2} \left(\frac{d^2 n(\lambda)}{d\lambda^2} \right) \quad \text{Eq. 2.2}$$

where β_2 is the group-velocity dispersion, $n(\lambda)$ is the wavelength-dependent refractive index of the medium, λ is the wavelength and c is the speed of light in vacuum. The group-velocity dispersion is defined as group-delay dispersion (GDD) per unit length in millimetre. In case of a short laser pulse, GVD broadens a transform-limited pulse in time domain. If $\beta_2 > 0$ for a medium (normal dispersion regime), the long wavelength components of the pulse propagate faster than the short ones and appear at the leading edge of the pulse (figure 2.3). For $\beta_2 < 0$ (anomalous dispersion regime) the long wavelengths travel slower and appear at the trailing edge. Most optical medium at wavelength of 1040 nm exhibit positive dispersion parameter.

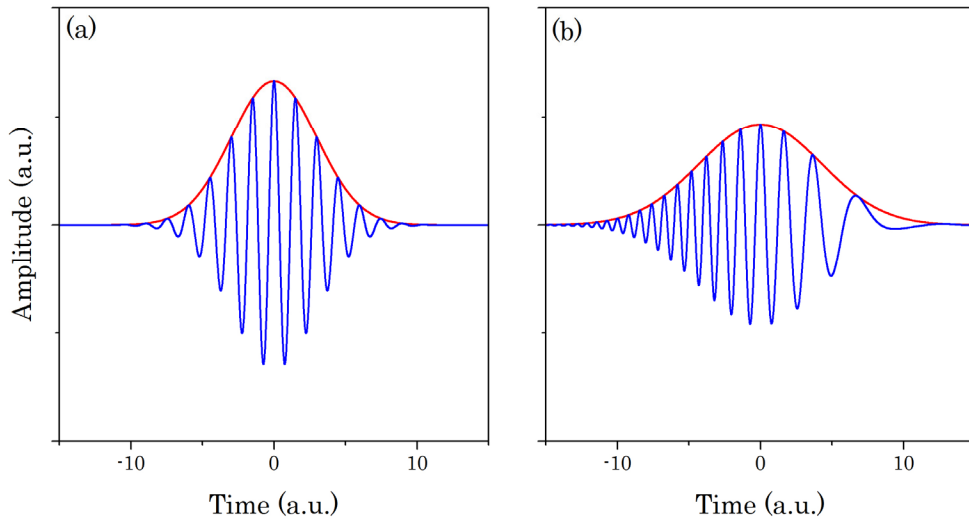


Figure 2.3. The effect of GVD parameter on a pulse: (a) a transform-limited pulse, (b) the dispersed pulse after propagating through a medium with negative β_2 . The blue line is the electrical field, the red line is the pulse envelope.

The dispersion effect also plays a prominent role in short pulse formation in a mode-locked laser oscillator and negative dispersion should be provided in order to balance it as well as the effect of self-phase modulation (section 2.4.1).

2.4. Optical Kerr effect

The refractive index of a medium can be altered in the presence of a strong optical field. It can be expressed as [7]

$$n(I) = n_0 + n_2 I(r, t) \quad \text{Eq. 2.3}$$

where n_0 is the linear refractive index, n_2 is the nonlinear refractive index and $I(r, t)$ is the intensity of the optical field in time and space. In case of propagation of an intense optical pulse, the time dependence of n_2 results in the instantaneous frequency shift within the pulse and the spatial dependence leads to a lensing (i.e. Kerr lensing) effect. The value of n_2 is positive for all optical materials.

2.4.1. Self-phase modulation (SPM)

The refractive index of a medium can be changed when an intense optical pulse propagates through it (Eq. 2.3). Through this change, the phase of the pulse is affected by the intensity of the pulse. The instantaneous frequency can be expressed as [7]

$$\omega(t) = \frac{d\varphi(t)}{dt} = \omega_0 - \frac{2\pi L}{\lambda_0} \frac{dn(I)}{dt} \quad \text{Eq. 2.4}$$

where $\varphi(t)$ is the instantaneous phase, L is the length of the medium, ω_0 and λ_0 are the central frequency and wavelengths of the pulse, respectively. The change in frequency content as a result of pulse intensity is called self-phase modulation (SPM). SPM generates and re-distributes the new wavelengths within a pulse envelope in time domain without broadening of the pulse. At the leading edge of the pulse, where the intensity rises, the instantaneous frequency is reduced and long wavelength components appear, while the trailing edge of the pulse produces the short wavelength components (figure 2.4). In frequency domain, SPM generates the additional frequency components and causes spectral broadening of the pulse.

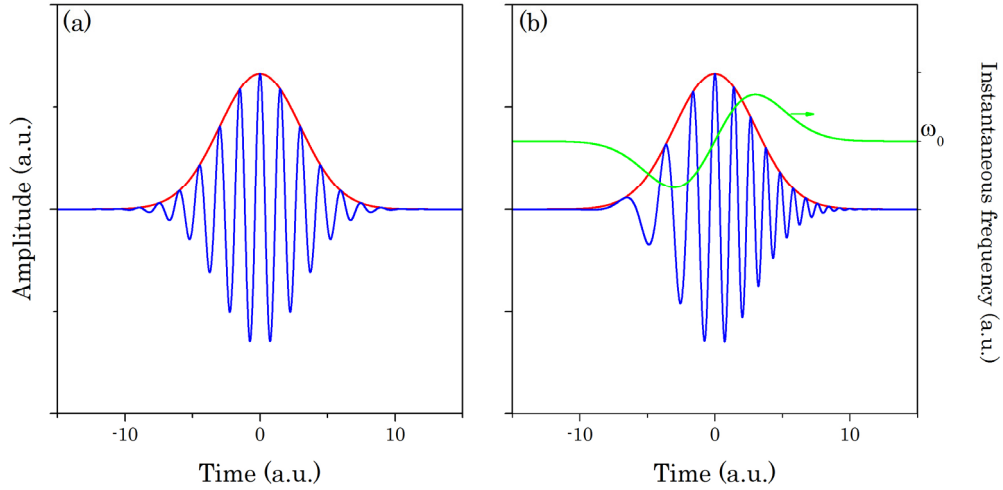


Figure 2.4. The effect of SPM on a pulse, (a) a transform-limited pulse, (b) the chirped pulse after propagating through a medium with positive n_2 . The blue line is the electrical field, the red line is the pulse envelope, the green line is the instantaneous frequency change.

In order to generate transform-limited ultra-short pulses (soliton pulses) from an oscillator, it is required that the effects of SPM and positive dispersion were balanced by the appropriate amount of negative dispersion. In time domain, the temporal broadening of the pulse due to the positive dispersion of optical components as well as the positive chirp induced by the SPM effect is canceled out by the negative dispersion. At the same time the pulse spectrum is broadened mainly due to the SPM effect. The dispersion compensation in a laser cavity can be accomplished by a variety of methods, including prism pair, chirped mirrors, grating pair and Gires–Tournois interferometer (GTI) mirrors [8].

In this work, GTI mirrors were used for dispersion compensation. A GTI mirror is a special case of a Fabry–Perot interferometer comprising a highly reflective rear mirror, a partially reflective front mirror and a spacer material. The incident light undergoes multiple internal reflections in spacer and the reflected light beams constructively interfere, experiencing some phase shift with respect to the incident light. This phase shift and therefore the group delay and dispersion parameter are wavelength dependent. A GTI mirror can provide specific value of negative dispersion for a limited range of wavelengths of interest, which can be used for compensating the positive dispersion of other optical components in a laser cavity [8,9].

2.4.2. Kerr lensing effect

The dependence of the refractive index on the intensity of laser light (Eq. 2.3) also affects the spatial phase of the propagating optical field. Considering the Gaussian distribution of the intensity over the beam cross-section area and a positive nonlinear refractive index (n_2), the refractive index becomes higher at the center of the beam and this part of the wave front propagates slower than in the outer parts of the beam, which leads to a focusing effect of the beam (see figure 2.5) [7,8].

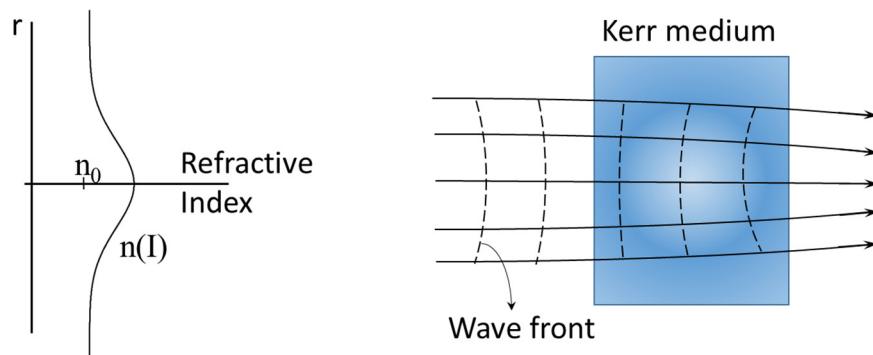


Figure 2.5. The Kerr lensing effect. The refractive index of the Kerr medium is modified in the presence of an intense laser beam.

The Kerr lensing effect can be induced by a high intensity laser pulse propagating through the laser crystal and can be exploited to produce self-amplitude modulation (SAM) for generating ultra-short pulses in a Kerr-lens mode-locked laser (section 2.5.2).

2.5. Mode-locked laser

In order to generate ultra-short laser pulses, the gain or loss in a laser resonator needs to be modulated. In time domain, the net-gain is provided for short instants of time within which the laser oscillation in the form of a pulse becomes possible. In case of solid-state lasers, where the gain medium usually exhibits long relaxation time, the loss modulation method is employed (figure 2.6). The pulsed laser is then called mode-locked laser, since many spectral modes oscillate with a constant phase relation [10–12].

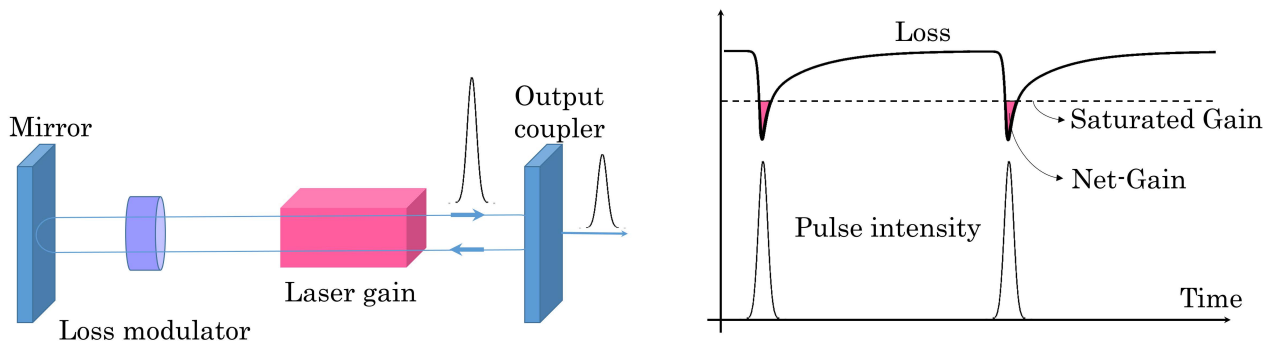


Figure 2.6. Pulse generation by means of loss modulation in a laser resonator.

Generating ultra-short pulses with sub-picosecond pulse width employs a passive mode locking technique, where the loss modulation is caused by the laser pulse itself. This is usually done with the help of an optical component called saturable absorber or the fast responding Kerr lensing effect. In frequency domain, the amplitude of the oscillating laser mode with a specific central frequency (which is initially produced at the peak of the gain) is modulated by the loss modulating effect. It results in generation of the side-band frequencies, oscillating with a fixed phase relationship and the laser therefore is mode-locked [10]. In this case all of the oscillating modes interfere constructively thus producing a single pulse per round trip in a laser cavity.

2.5.1. Mode-locked laser with saturable absorber

In a mode-locked laser saturable absorbers can be used as a loss modulator. The most common type of saturable absorber is a semiconductor saturable absorber mirror (SESAM). A SESAM essentially consists of a Bragg mirror structure and a saturable absorber layer (figure 2.7). The Bragg mirror part acts as a reflective mirror and is comprised of stack of semiconductor layers with varying refractive index. At the interface of each layer, a portion of the penetrating light is reflected back based on Fresnel reflection. In order to have constructive interference of the created reflections of light for a particular wavelength, the optical distance between the interfaces (Λ) should satisfy the Bragg condition, i.e., $\lambda_B = 2n_{eff}\Lambda$. The absorber layer on top of the Bragg mirror absorbs light and exhibits loss for light with low fluence (i.e. energy/area) and has lower light absorption and loss at higher fluence levels. The saturation fluence of a SESAM can be defined as a pulse fluence that can reduce the absorption of SESAM by $1/e$ (37%) of its initial

value. The maximum change in nonlinear reflectivity of the absorber is called the modulation depth. The actual fluence of laser on a SESAM could be roughly 5 times the saturation fluence so that the largest modulation depth can be reached. Consequently, a saturable absorber can act as a loss modulator in a mode-locked laser [11,13].

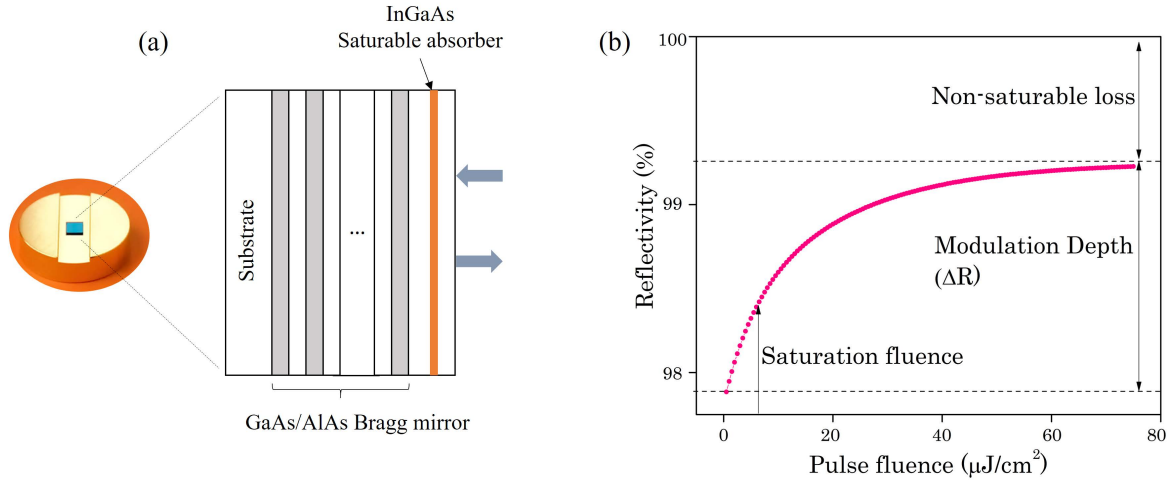


Figure 2.7. (a) SESAM on a copper heat sink and its schematic structure, (b) the reflectivity of a SESAM in terms of pulse fluence.

At the initial stage of pulse formation in a laser resonator incorporating a SESAM as the end mirror, a random intense fluctuation in a laser (i.e. long pulse) can lower the loss of a SESAM and is reflected back into the resonator. Then, it is amplified by the net-gain in successive round trips in the resonator and becomes narrower in width through the mode locking process. In this process, a SESAM assists in pulse narrowing by letting the central part (the most intense part) of the pulse to pass through the SESAM and by absorbing the tails (the less intense part) of the pulse. However, this pulse shortening is only significant during the initial stage of the mode locking process. The main pulse shortening is governed by the nonlinear dynamics of soliton formation and by the balancing of the SPM and GVD effects.

The SESAM that was used in this work was a quantum-dot saturable absorber mirror (QD-SESAM). In the semiconductor absorber layer, the free charge carriers were confined to infinitesimal spatial dimension so that the energy states of the absorber are sharply confined. It results in a sub-picosecond recovery time of carriers as well as lower saturation fluence ($25 \mu\text{J}/\text{cm}^2$), when compared to their quantum-well counterparts with higher saturation fluence ($70-$

100 $\mu\text{J}/\text{cm}^2$). The former is favorable for short pulse generation since the absorber recovers its absorption right after the pulse and the latter is desired for convenient self-starting pulsed operation from the noise level and avoiding the Q-switched operation regime of a mode-locked laser. Furthermore, the absorption and gain bandwidth of the QD-SESAMs are inhomogeneously broadened as a result of Gaussian distribution of dot sizes in absorber structure, which is beneficial for supporting of ultra-short pulses with broad spectrum [14–16].

2.5.2. Kerr-lens mode-locked laser (KLM)

The generation of ultra-short pulses by fast loss modulation is also possible by employing the Kerr lensing effect in a laser gain medium with large nonlinear refractive index (n_2). If an intense pulse of a laser beam passes through the laser crystal, it induces the Kerr lensing effect for an extremely short time and as a result the laser beam is self-focused. With a hard-aperture placed in the way of the laser beam, the self-focused laser mode experiences a low spatial loss, as opposed to the continuous-wave laser without the self-focusing effect (figure 2.8 (a)). In this way, an intra-cavity loss modulation can be provided and this technique is called a hard-aperture Kerr-lens mode locking. Since the Kerr lensing effect is a fast responding effect, it is favorable for generating ultra-short pulses [11].

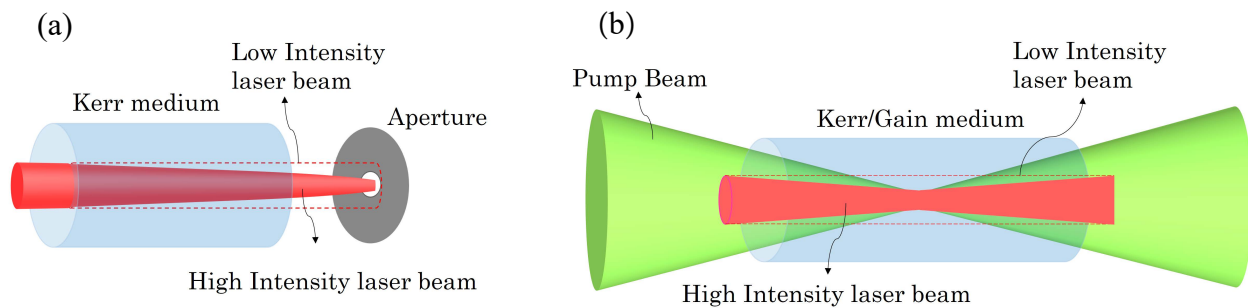


Figure 2.8. Kerr lensing effect and spatial loss modulation in case of a hard-aperture mode locking (a) and soft-aperture mode locking of a laser (b).

An artificial aperturing effect in a Kerr-lens mode-locked laser can be also accomplished through the spatial overlap of the pump beam and the laser mode. In such a case the self-focused laser beam overlaps more efficiently with the pump beam and experiences a higher gain (figure 2.8 (b)). This method is called a soft-aperture Kerr-lens mode locking [17,18].

A Kerr-lens mode-locked laser is capable of generating pulses as short as few femtoseconds owing to its fast saturable absorber action and loss modulation [11]. However, this method requires a critical design of the laser resonator which requires it to be operated near the stability limit. Also, the mode-locked laser operation is not usually self-starting and requires external perturbation. On the other hand, mode-locked lasers based on the semiconductor saturable absorbers offer reliable pulse oscillation and the mode locking is self-starting. The disadvantages of the SESAM mode-locked lasers include the high cost of a SESAM, high likelihood of its damage and dependency of the generated pulses on the absorber properties. The generated pulses in a SESAM mode-locked laser are usually longer than in a Kerr-lens mode-locked laser [11].

A dual action of the Kerr-lens mode locking and semiconductor saturable absorber mirror mode locking techniques can combine the favorable features of both methods. The semiconductor saturable absorber mirror can provide a sustainable and self-starting generation of initial laser pulses and, on the other hand, the fast loss modulation and broadband operation of the Kerr lensing can make it possible to generate ultra-short laser pulses [19–21].

2.5.3. Mode-locked laser model

In a mode-locked laser with a balanced SPM and GVD, the generated pulse undergoes the amplification and temporal spreading in the gain medium, SPM spectral broadening, and pulse width compression due to the negative GVD in the cavity (figure 2.9). The pulse retains its shape, intensity and duration after a round-trip in the cavity if the GVD and SPM effects balance each other. Therefore, the pulse is called a soliton pulse and the system is called a soliton mode-locked laser. The generated pulse can be modelled by the Haus' master equation as follows [22]

$$T_R \frac{\partial A(T,t)}{\partial T} = (g - l)A + (D_g - jD) \frac{\partial^2}{\partial t^2} A + (j\delta)|A|^2 A - q(T,t)A, \quad \text{Eq.2.5}$$

where $A(T,t)$ is the slowly varying pulse envelope, T_R is the cavity round-trip time, g is the saturated gain, l is the linear loss, $D_g = \frac{g}{\Omega_g^2} + \frac{1}{\Omega_f^2}$ is the gain, the gain bandwidth and intra-cavity filtering effect, D is the GVD, δ is the SPM coefficient and $q(T,t)$ is the response of the saturable absorber which describes the self-amplitude modulation (SAM) effect. The last term also includes the Kerr-lens mode locking since the Kerr lensing effect acts as an artificial fast saturable absorber. In case

of mode locking of a laser by a SESAM where the pulse formation is determined by the soliton mode locking through the balancing of the GVD and SPM effects, the saturable absorber mainly acts as a starter and pulse stabilizer. In case of a KLM laser, however, the fast saturable-absorption like effect has a prominent role in pulse formation. The generated pulse has a $sech^2$ function shape and its full-width at half-maximum (FWHM) duration is determined by the parameters in Eq.2.5. In general, the generated pulse width has direct relation with the total dispersion in the laser cavity.

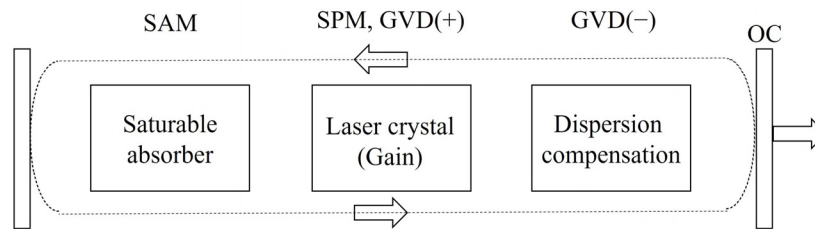


Figure 2.9. The laser model and contribution of SPM, GVD and SAM in pulse formation.

GVD(+) is the positive dispersion, GVD(-) is the negative dispersion.

References

1. F. Druon, F. Balembois, and P. Georges, "New laser crystals for the generation of ultrashort pulses," *Comptes Rendus Phys.* **8**, 153–164 (2007).
2. S. R. Bowman, S. P. O'Connor, and S. Biswal, "Ytterbium laser with reduced thermal loading," *IEEE J. Quantum Electron.* **41**, 1510–1517 (2005).
3. R. Hegenbarth, A. Steinmann, G. Tóth, J. Hebling, and H. Giessen, "Two-color femtosecond optical parametric oscillator with 1.7 W output pumped by a 7.4 W Yb:KGW laser," *J. Opt. Soc. Am. B* **28**, 1344 (2011).
4. H. Zhao and A. Major, "Dynamic characterization of intracavity losses in broadband quasi-three-level lasers," *Opt. Express* **22**, 26651 (2014).
5. V. E. Kisel, A. S. Rudenkov, A. A. Pavlyuk, A. A. Kovalyov, V. V. Preobrazhenskii, M. A. Putyato, N. N. Rubtsova, B. R. Semyagin, and N. V. Kuleshov, "High-power, efficient, semiconductor saturable absorber mode-locked Yb:KGW bulk laser," *Opt. Lett.* **40**, 2707 (2015).
6. D. Stučinskas, R. Antipenkov, and A. Varanavičius, "Thermal lensing in high-power diode-pumped Yb:KGW laser," *Lith. J. Phys.* **50**, 191–199 (2010).
7. C. Rulliere, "Femtosecond Laser Pulses," *Advanced Texts in Physics* (Springer New York, 2005).
8. U. Keller, "Ultrafast solid-state lasers," in *Laser Systems, Part 1* (Springer Berlin Heidelberg, 2007), pp. 33–167.
9. P. M. W. French, G. F. Chen, and W. Sibbett, "Tunable group velocity dispersion interferometer for intracavity and extracavity applications," *Opt. Commun.* **57**, 263–268 (1986).
10. H. A. Haus, "Mode locking of lasers," *IEEE J. Sel. Top. Quantum Electron.* **6**, 1173–1185 (2000).
11. U. Keller, "Recent developments in compact ultrafast lasers," *Nature* **424**, 831–838 (2003).
12. U. Keller, "Ultrafast solid-state laser oscillators: a success story for the last 20 years with no end in sight," *Appl. Phys. B* **100**, 15–28 (2010).
13. U. Keller, K. J. Weingarten, F. X. Kartner, D. Kopf, B. Braun, I. D. Jung, R. Fluck, C. Honninger, N. Matuschek, and J. Aus der Au, "Semiconductor saturable absorber mirrors (SESAM's) for femtosecond to nanosecond pulse generation in solid-state lasers," *IEEE J. Sel. Top. Quantum Electron.* **2**, 435–453 (1996).
14. E. U. Rafailov, M. A. Cataluna, and W. Sibbett, "Mode-locked quantum-dot lasers," *Nat. Photonics* **1**, 395–401 (2007).
15. A. A. Lagatsky, C. G. Leburn, C. T. A. Brown, W. Sibbett, S. A. Zolotovskaya, and E. U. Rafailov, "Ultrashort-pulse lasers passively mode locked by quantum-dot-based saturable absorbers," *Prog. Quantum Electron.* **34**, 1–45 (2010).
16. E. U. Rafailov, S. J. White, A. A. Lagatsky, A. Miller, W. Sibbett, D. A. Livshits, A. E. Zhukov, and V. M. Ustinov, "Fast Quantum-Dot Saturable Absorber for Passive Mode Locking of Solid-State Lasers," *IEEE Photonics Technol. Lett.* **16**, 2439–2441 (2004).
17. J. Herrmann, "Theory of Kerr-lens mode locking: role of self-focusing and radially varying gain," *J. Opt. Soc. Am. B* **11**, 498 (1994).
18. H. Liu, J. Nees, and G. Mourou, "Diode-pumped Kerr-lens mode-locked Yb:KY(WO₄)₂ laser," *Opt. Lett.* **26**, 1723 (2001).
19. H. Zhao and A. Major, "Powerful 67 fs Kerr-lens mode-locked prismless Yb:KGW

- oscillator," *Opt. Express* **21**, 31846 (2013).
20. D. H. Sutter, G. Steinmeyer, L. Gallmann, N. Matuschek, F. Morier-Genoud, U. Keller, V. Scheuer, G. Angelow, and T. Tschudi, "Semiconductor saturable-absorber mirror-assisted Kerr-lens mode-locked Ti:sapphire laser producing pulses in the two-cycle regime," *Opt. Lett.* **24**, 631 (1999).
 21. F. Friebel, F. Druon, J. Boudeile, D. N. Papadopoulos, M. Hanna, P. Georges, P. Camy, J. L. Doualan, A. Benayad, R. Moncorgé, C. Cassagne, and G. Boudebs, "Diode-pumped 99 fs Yb:CaF₂ oscillator," *Opt. Lett.* **34**, 1474–6 (2009).
 22. F. X. Kartner, I. D. Jung, and U. Keller, "Soliton mode locking with saturable absorbers," *IEEE J. Sel. Top. Quantum Electron.* **2**, 540–556 (1996).

Chapter 3

Continuous-wave dual-wavelength Yb:KGW laser

3.1. Introduction

In this chapter, the development of a high power continuous-wave dual-wavelength laser based on Yb:KGW crystal is demonstrated. Such a laser source is desirable for THz imaging and spectroscopy applications. A brief introduction and a review of previous work on dual-wavelength lasers are given. Then, the experimental setup and results are presented and the improved features of the laser are discussed. In this experiment, a stable dual-wavelength operation at 1014.6 and 1041.3 nm (7.57 THz of frequency offset) with 3.4 W of average output power and a diffraction-limited beam profile was obtained. Dual-wavelength laser operation at shorter- or longer-wavelength pairs with lower average output power could also be realized for other output-coupling transmissions. The results of this experiment demonstrated an order of magnitude higher output power and ~ 4 times higher optical-to-optical efficiency when compared to the values reported in previous experiments based on Yb:KGW laser crystal, while using a significantly simpler laser design.

3.2. CW dual-wavelength laser

Continuous-wave (CW) dual-wavelength lasers with wavelengths separated by a few THz have established their applications in THz imaging and spectroscopy [1,2]. Dual-wavelength laser action has been reported in a number of laser crystals such as Nd:YVO₄ [3] and Nd:GdVO₄ [4] where the generated wavelengths were set by the specific laser-cavity optics design and the intrinsic properties of the gain media, which typically have multiple well defined laser transitions (e.g., 912 and 1064 nm). On the other hand, simultaneous CW dual-wavelength oscillation is possible by providing the same lasing threshold condition and net-gain equalization for two particular spectral lines within one sufficiently broad gain bandwidth. This approach is possible

with broad gain bandwidth laser materials such as Yb-ion-doped or Ti:sapphire. Tunable CW dual-wavelength lasers based on Yb:KGd(WO₄)₂ (Yb:KGW) crystal have been demonstrated by using chirped-volume Bragg gratings [5] and glass etalons [6] where the generated wavelengths were independently tunable with variable separation up to 7.8 and 3.1 THz, respectively. These laser systems, however, required rather complex design in terms of the number of optical elements used in the cavity for tuning of the wavelengths, requirements for spatial separation of the two generated wavelengths, and the custom designed pump-shaping system.

Recently, a CW dual-wavelength laser has been reported in a diode-pumped Yb:KGW laser without employing any additional elements for polarization control [7]. By using the polarization-dependent reabsorption loss as a mechanism to reach gain equalization, two orthogonally polarized laser lines along the N_m- and N_p-axes were generated. The polarization-dependent reabsorption loss originated from the anisotropic thermal lensing effect and the dual-wavelength operation was controlled by the pump power in certain pump-power ranges. A dual-wavelength oscillation at 1028.7 nm (E//N_m) and 1037.5 nm (E//N_p) with 4.6 W of output power using 5% output coupling could be generated and the wavelength separation slightly depended on the output coupling level. Similar thermal-lens driven polarization switching in dual-wavelength operation was also observed in a Tm:KL(WO₄)₂ laser [8].

As a more convenient approach dual-wavelength laser action can be realized by means of a birefringent filter (BRF) when its wavelength-dependent loss in a laser cavity results in the net-gain equalization for two wavelengths. A multiple-plate BRF was recently used with a Ti:sapphire laser to generate wavelengths with fixed separation of around 2 nm and tunable between 805 and 840 nm [9]. In this case however, a custom-built multiplate BRF required a sophisticated design procedure. At the same time this approach has not yet been reported with diode-pumped Yb-doped laser crystals. Among the Yb-doped gain media, the laser crystal of Yb:KGW attracts attention due to its high emission cross-section (2.8×10^{-20} cm² for polarization along its N_m-axis) and fairly broad amplification bandwidth (~25 nm) with small intrinsic quantum defect [10]. These properties allow the use of a wavelength-dependent loss optical component such as a birefringent filter in order to generate two distinct wavelengths within the available gain bandwidth. Since the free spectral range (i.e., separation of transmission peaks) of a single plate BRF depends on its

thickness, it is possible to find a condition when it can be accommodated by the available gain bandwidth, thus greatly simplifying the design of a dual-wavelength laser.

The wavelength-dependent loss property of a BRF originates from the wavelength-dependent phase retardation caused by its birefringent structure and can be expressed as [11]

$$\begin{aligned} \varphi &= \sin^2 \gamma (k\delta l / \cos \phi), \\ \sin^2 \gamma &= \cos^2 \theta \sin^2 \alpha + (\cos \phi \cos \theta \cos \alpha - \sin \phi \sin \theta)^2, \end{aligned} \quad \text{Eq. 3.1}$$

where φ is the phase retardation due to birefringence, k is the wavenumber in vacuum, δ is the difference between the ordinary and extraordinary refractive indices ($n_e - n_o$), l is the thickness of the filter plate, ϕ is the refraction angle of the ordinary ray, θ is the angle between the optical axis of BRF and its surface plane, and α is the angle between the optical axis of the crystal and plane of incidence (rotation angle), as shown in figure 3.1. For a quartz BRF plate cut at its normal axis and placed at the Brewster's angle, $\delta \approx 0.009$, $\phi \approx 33^\circ$, and $\theta = 0$. The phase retardation results in a wavelength-dependent transmission profile exhibiting low loss peaks at wavelengths whose separation is governed by the thickness of the filter and its orientation. The free spectral range of a BRF plate can be explicitly expressed as [12]

$$\Delta\lambda = \frac{\lambda_0^2}{\delta l} \frac{\sin \phi_B}{1 - (\cos^2 \alpha \cos^2 \phi_B)}, \quad \text{Eq. 3.2}$$

where ϕ_B is the Brewster's angle, and $\lambda_0 = 2\lambda_1\lambda_2/(\lambda_1 + \lambda_2)$. Consequently, for an appropriate thickness of the BRF, two low loss transmission peaks can fall within the gain bandwidth of the laser crystal, which is necessary for dual-wavelength operation of a laser.

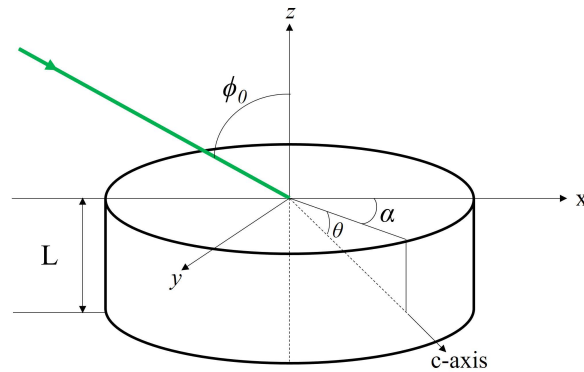


Figure 3.1. Schematic of a birefringent filter plate.

In this work a high-power CW dual-wavelength Yb:KGW laser was demonstrated using a single birefringent filter plate. With an N_g -cut crystal, the generated wavelengths had the same polarization along the N_m -axis of the crystal and a stable laser operation at 1014.6/1041.3 nm wavelengths with 3.4 W of average output power using a 4 mm thick birefringent filter plate was demonstrated.

3.3. Experiment and results

A 5 mm-long Yb:KGW crystal (Eksma) with a doping level of 1.5 at. % was cut along its N_g -axis and was antireflection coated for pump and laser wavelengths. The pump laser was delivered by a fiber-coupled laser diode (100 μm core, 0.22 NA, Apollo Instruments Inc.) and two achromatic doublets with 1:3 imaging ratio focused the pump beam to a waist of 300 μm in diameter inside the crystal (see figure 3.2). The laser diode could provide up to 30 W of pump power. The laser diode as well as the crystal were water-cooled at 16°C in order to stabilize the pump wavelength around 980 nm. In a Z-fold cavity the laser mode size of 270 μm was formed for appropriate spatial mode matching with the pump beam to maximize output power and to avoid dual-wavelength operation observed in [7]. In order to introduce a wavelength-dependent loss to the laser cavity, a quartz birefringent plate (Cstech Inc.) with a thickness of 4 mm was placed at Brewster's angle in the long arm of the cavity before the output coupler. The output power and laser spectrum of dual-wavelength oscillation were recorded by a calibrated power meter and an optical spectrum analyzer with a resolution of 0.07 nm, respectively.

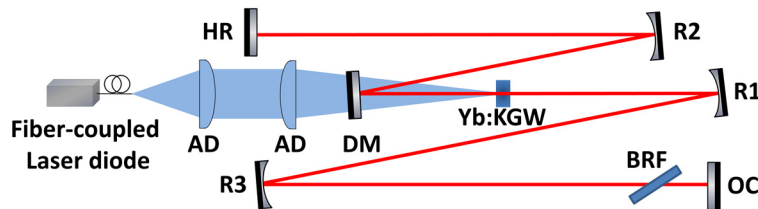


Figure 3.2. Experimental setup of a CW dual-wavelength Yb:KGW oscillator. AD, achromatic doublets; R1-3, concave mirrors; OC, output coupler. R1=300 mm, R2=300 mm, and R3=500 mm.

The N_g -cut Yb:KGW crystal exhibited a strong absorption ($\sim 50\%$ – 60%) of the unpolarized pump radiation around 980 nm [13,14]. The CW laser could deliver up to 6 W of average power

with laser polarization along the N_m -axis without the birefringent filter in the laser cavity. The Yb:KGW crystal exhibited a thermal-lensing effect that was measured to be around 100–150 mm of equivalent focal length [15] for the operating range of pump power. A wavelength-dependent loss was then introduced to the laser by inserting the BRF plate at the Brewster's angle. Therefore, the wavelengths that experienced the phase retardation of 2π were transmitted through the filter with low loss. In our configuration the 4 mm thick birefringent quartz plate could provide a wavelength separation up to 35 nm according to the Eq. (3.2).

A dual-wavelength Yb:KGW laser operation was realized with 5% output coupler at 1014.6 and 1041.3 nm ($\Delta\nu = 7.57$ THz) with maximum average output power of 3.4 W at 27.9 W of pump power. The dual-wavelength operation for different pump powers is shown in figure 3.3. The variation in average output power based on the measurement of standard deviation is also shown as error bars. As can be seen, the variation in average output power decreases at high pump powers, which could equivalently be observed as relative instantaneous change of spectral amplitudes of the oscillating wavelengths (which was about 10%) using the spectrum analyzer. At each pump power level the BRF had to be slightly adjusted to maintain a $\sim 1:1$ spectral intensity ratio of the generated wavelengths. The lower limit of the pump power for dual-wavelength operation was imposed by the condition where simultaneous oscillation of wavelengths was not possible. The linewidths of the generated wavelengths were measured to be 0.07 nm and were limited by the resolution of our spectrometer. For 5% output coupling, the slope efficiency of 30% with respect to the pump power (55% with respect to the absorbed pump power in nonlasing condition) and optical-to-optical efficiency of 12.2% for the highest incident pump power (23.3% with respect to the absorbed pump power) was obtained. Our results represent an order of magnitude higher output power and ~ 4 times higher optical-to-optical efficiency when compared to the values reported in [5] and [6]. In these cases total dual-wavelength output powers of 250 and 120 mW and optical-to-optical efficiencies of 6% (with respect to the absorbed pump power) and 3% (with respect to the incident pump power) were achieved, respectively. On the other hand, comparing with the optical-to-optical efficiencies of $\sim 16\%$ – 17% previously obtained by us in dual-wavelength [7] and single-wavelength [13] regimes, our results indicate an increase in intracavity losses caused by the insertion of the birefringent filter.

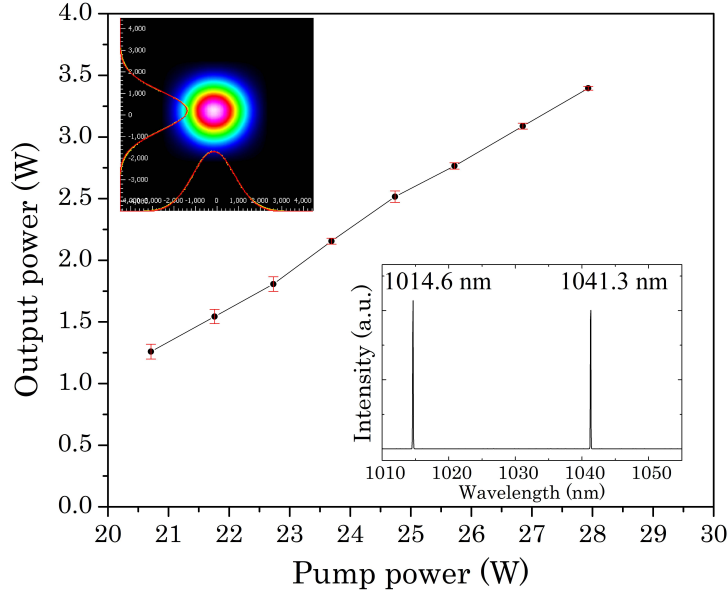


Figure 3.3. Output power versus pump power for dual-wavelength laser with 5% output coupler. Insets: the beam intensity profile and laser spectrum at the highest pump power.

In figure 3.3 the output beam intensity profile at the highest output power is also depicted in the inset, which exhibited almost perfect Gaussian intensity distribution along both axes. The M^2 beam quality factor (Appendix A) was measured to be less than 1.2. The average output power of the dual-wavelength laser for different output coupling levels at the highest pump power of 27.9 W, as well as the corresponding generated wavelength pairs, are shown in figure 3.4. The short wavelengths of the dual-wavelength laser between 1010 and 1018.8 nm and long wavelengths between 1038.5 and 1048.5 nm could be generated for these output couplers. The highest average output power of 3.4 W was obtained for the 5% output coupler.

As shown in figure 3.4 (b) the generated wavelengths for higher output coupling were shifted toward shorter wavelengths while their separation remained almost constant. Since the effective gain of Yb:KGW as a quasi-three level laser medium is influenced by the reabsorption loss, it can be expressed with the help of Eq. 2.1 (see Chapter 2) as [13]

$$g_{eff}(\lambda_L) = 2 N_0 l_c (\beta \sigma_{em}(\lambda_L) - (1 - \beta) \sigma_{abs}(\lambda_L)), \quad \text{Eq. 3.3}$$

where N_0 is the ground-state population set by the doping level, l_c is the length of the laser crystal, β is the fractional population inversion, and $\sigma_{em}(\lambda_L)$ and $\sigma_{abs}(\lambda_L)$ are the emission and absorption cross sections at laser wavelength, respectively. A higher output coupling leads to a higher steady-

state gain and a higher fractional population inversion β . In case of Yb:KGW, a higher gain exhibits a peak at shorter wavelengths [13] and the observed wavelength shift in our laser is due to the shift in the peak of the effective gain of Yb:KGW for higher output coupling.

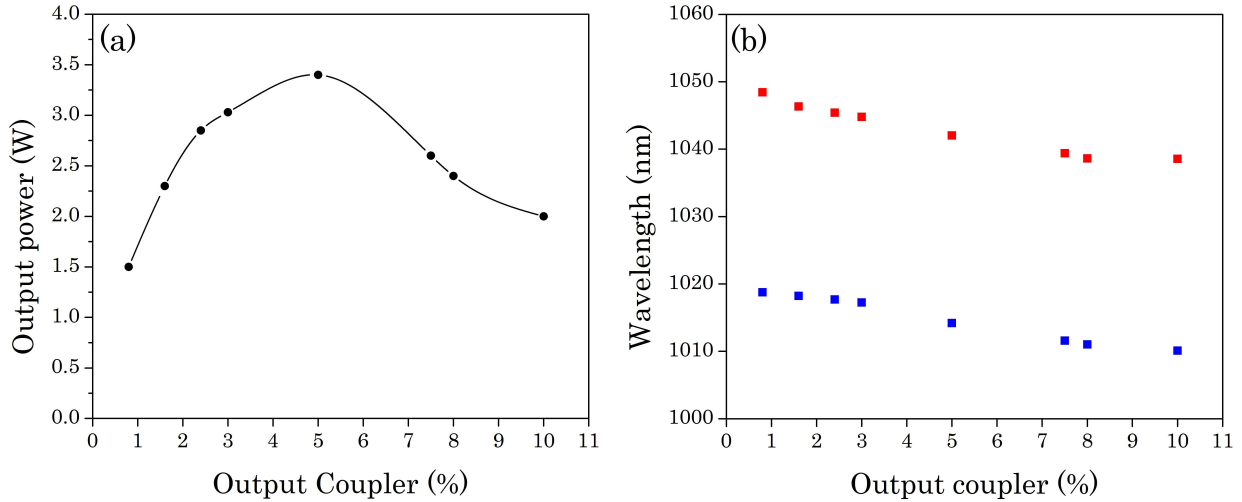


Figure 3.4. (a) Average output power of dual-wavelength laser for different output couplers at the highest pump power of 27.9 W. Circles – experimental data points; solid line is for the eye guide only. (b) Wavelengths of oscillating modes for different output couplers.

Since the free spectral range of a birefringent filter is inversely related to its thickness (Eq. 3.2), the proposed approach allows changing of the wavelength separation by using filter plates with thicknesses other than 4 mm. Indeed, by using a 6 mm thick BRF, dual-wavelength laser oscillation was achieved with $\Delta\lambda=16.7$ nm, which corresponds to $\Delta\nu=4.65$ THz. This result is in good agreement with Eq. (3.2), which predicts a reduction in wavelength separation by a factor of 0.67 ($\Delta\lambda = 26.7$ nm for 4 mm BRF). At the same time dual-wavelength generation was not feasible for a BRF plate with smaller thickness (e.g., 2 mm) since the free spectral range of which became larger than the available effective gain bandwidth of the used Yb:KGW crystal.

3.4. Conclusion

In conclusion, a high-power dual-wavelength laser operation of a diode pumped N_g -cut Yb:KGW crystal using a single BRF plate was demonstrated. It exhibited stable oscillating wavelengths and a diffraction-limited output-beam profile. For a pump power of 27.9 W, dual-wavelength laser radiation at 1014.6/1041.3 nm and 3.4 W of output power using a 5% output

coupler could be generated. This represents an improvement of more than an order of magnitude in output power and higher optical-to-optical efficiency when compared to the previous results while using a significantly simpler laser design. The observed slope efficiency was 30% with the beam quality factor of less than 1.2. By using a higher output coupling, wavelength pairs at shorter wavelengths were generated with lower output powers. The demonstrated approach allows stable generation of dual-wavelength radiation with controllable spacing that can be achieved by varying the thickness of the employed BRF plate. However, this approach does not offer individual control of the wavelength. We believe that the same technique can be also used with other gain media as well as fiber lasers. The demonstrated laser can be used to generate THz radiation by using photoconductive antenna (photomixer) [16,17].

References

1. J. B. Baxter and G. W. Guglietta, "Terahertz Spectroscopy," *Anal. Chem.* **83**, 4342–4368 (2011).
2. C. B. Reid, E. Pickwell-MacPherson, J. G. Laufer, A. P. Gibson, J. C. Hebden, and V. P. Wallace, "Accuracy and resolution of THz reflection spectroscopy for medical imaging," *Phys. Med. Biol.* **55**, 4825 (2010).
3. Y.-F. Chen, "CW dual-wavelength operation of a diode-end-pumped Nd:YVO₄ laser," *Appl. Phys. B Lasers Opt.* **70**, 475–478 (2000).
4. K. Lünstedt, N. Pavel, K. Petermann, and G. Huber, "Continuous-wave simultaneous dual-wavelength operation at 912 nm and 1063 nm in Nd:GdVO₄," *Appl. Phys. B* **86**, 65–70 (2006).
5. A. Brenier, "Tunable THz frequency difference from a diode-pumped dual-wavelength Yb³⁺:KGd(WO₄)₂ laser with chirped volume Bragg gratings," *Laser Phys. Lett.* **8**, 520–524 (2011).
6. R. Czarny, M. Alouini, C. Larat, M. Krakowski, and D. Dolfi, "THz-dual-frequency Yb³⁺:KGd(WO₄)₂ laser for continuous wave THz generation through photomixing," *Electron. Lett.* **40**, 942 (2004).
7. H. Zhao and A. Major, "Orthogonally Polarized Dual-Wavelength Operation of a CW Yb:KGW Laser Induced by Thermal Lensing," in *CLEO (OSA, 2013)*, p. CTh4I.2.
8. P. A. Loiko, X. Mateos, N. V Kuleshov, A. A. Pavlyuk, K. V Yumashev, V. Petrov, U. Griebner, M. Aguilo, and F. Diaz, "Thermal-Lens-Driven Effects in N_g-Cut Yb-and Tm-Doped Monoclinic KLu(WO₄)₂ Crystals," *IEEE J. Quantum Electron.* **50**, 1–8 (2014).
9. C. G. Trevino-Palacios, O. J. Zapata-Nava, E. V. Mejia-Urriarte, N. Qureshi, G. Paz-Martinez, and O. Kolokolstev, "Dual wavelength continuous wave laser using a birefringent filter," *J. Eur. Opt. Soc. Rapid Publ.* **8**, 13021 (2013).
10. S. R. Bowman, S. P. O'Connor, and S. Biswal, "Ytterbium laser with reduced thermal loading," *IEEE J. Quantum Electron.* **41**, 1510–1517 (2005).
11. K. Naganuma, G. Lenz, and E. P. Ippen, "Variable bandwidth birefringent filter for stable femtosecond lasers," *IEEE J. Quantum Electron.* **28**, 2142–2150 (1992).
12. S. Zhu, "Birefringent filter with tilted optic axis for tuning dye lasers: theory and design," *Appl. Opt.* **29**, 410 (1990).
13. H. Zhao and A. Major, "Dynamic characterization of intracavity losses in broadband quasi-three-level lasers," *Opt. Express* **22**, 26651 (2014).
14. H. Zhao and A. Major, "Megawatt peak power level sub-100 fs Yb:KGW oscillators," *Opt. Express* **22**, 30425 (2014).
15. H. Mirzaeian, S. Manjooran, and A. Major, "A simple technique for accurate characterization of thermal lens in solid state lasers," in *SPIE Proceedings* **9288**, pp. 928802–1 (2014).
16. M. Tani, O. Morikawa, S. Matsuura and M. Hangyo, "Generation of terahertz radiation by photomixing with dual-and multiple-mode lasers," *Semiconductor Science and Technology* **20**, S151 (2005).
17. S. Hoffmann, and M. R. Hofmann. "Generation of terahertz radiation with two color semiconductor lasers." *Laser & Photonics Reviews* 1.1, 44-56 (2007).

Chapter 4

High power femtosecond mode-locked Yb:KGW laser based on quantum-dot saturable absorber and Kerr lensing effect

4.1. Introduction

In this chapter, the generation of high power ultrashort pulses from diode-pumped Yb:KGW lasers based on dual-action of Kerr lensing effect and quantum-dot semiconductor saturable absorber mirror (QD-SESAM) is demonstrated. The main goal of these experiments was to generate watt-level sub-100 fs pulses directly from the laser oscillator. Such pulses are highly desirable for excitation of various nonlinear processes. In the first set of experiments (section 4.3) by using a quantum-dot saturable absorber mirror with a 0.7% (0.5%) modulation depth, the mode-locked laser delivered 90 fs (93 fs) pulses with 3.2 W (2.9 W) of average power at the repetition rate of 77 MHz, corresponding to 462 kW (406 kW) of peak power and 41 nJ (38 nJ) of pulse energy. To the best of our knowledge, these present the highest average and peak powers generated to date from quantum-dot saturable absorber-based mode-locked lasers and one of the highest in sub-100 fs regime from bulk lasers. In the second set of experiments (section 4.4) a watt-level sub-60 fs laser was demonstrated. The laser delivered 56 fs pulses with 1.95 W of average power corresponding to 450 kW of peak power. The width of the generated laser spectrum was 20.5 nm, which was near the gain bandwidth limit of the Yb:KGW crystal. To the best of our knowledge, these are the shortest pulses generated from the monoclinic double tungstate crystals (and Yb:KGW laser crystal in particular) and are the most powerful in the sub-60 fs regime for bulk Yb-doped lasers. At the same time they are also the shortest pulses produced to date with the help of a quantum-dot-based saturable absorber mirror. A comprehensive comparison of the performance of our lasers and previous results is also provided (section 4.5).

4.2. Mode-locked laser based on dual-action of quantum-dot saturable absorber mirror and Kerr lensing effect

High power operation of ultrashort pulse laser sources is highly desirable for a variety of nonlinear optical experiments [1–4]. The Yb-ion based laser oscillators are well suited for this task. Indeed, such a performance of a mode-locked laser in high power regime is feasible owing to the propitious properties of Yb-ion crystals, including fairly broad gain bandwidth, absorption properties suitable for diode pumping, absence of parasitic losses and tolerable level of thermo-optical effects [5–7]. Among the commercially available Yb-doped crystals, Yb:KGW exhibits favourable properties for generating high power sub-100 fs pulses (Chapter 2). The generation of high power ultrashort pulses with a spectrum as broad as the emission bandwidth of the gain medium is still a demanding task. As was discussed in Chapter 2, in the high power regime the induced nonlinear effects, non-negligible thermal lensing and broad-band group velocity dispersion (GVD) compensation should be carefully addressed.

The conventional design of a mode-locked laser system based on semiconductor saturable absorber mirrors (SESAMs) offers a flexible procedure and it provides a reliable and efficient femtosecond laser performance. However, this method is limited in further shortening of the pulse duration owing to the finite recovery time of the absorber which is also susceptible to damage. On the other hand, Kerr-lens mode locking technique (KLM) enables one to generate shorter pulses due to its inherently fast saturable absorption-like effect, but it requires careful design procedure and does not usually offer self-starting mode-locked oscillation [8]. A combination of these two techniques (termed KLAS: Kerr-lens and saturable absorber) can provide a mechanism that benefits from the self-starting operation provided by the SESAM as well as the fast loss modulation and broadband operation of the KLM lasers [9,10]. At the same time the KLAS mode-locked lasers based on the quantum-dot SESAMs can be an alternative approach to the widely used quantum-well SESAMs.

Quantum-dot semiconductor saturable absorber mirrors (QD-SESAMs) have attracted a lot of interest for generation of ultrashort laser pulses from solid-state and fiber lasers [11–15] due to their favorable properties when compared with the widely used quantum-well counterparts, QW-SESAMs [16]. Indeed, because of the strong confinement of free charge carriers to infinitesimal spatial dimension, the density of states is sharply enhanced. In QD-SESAMs this leads to a sub-

picosecond recovery time of carriers and low saturation fluence ($25 \mu\text{J}/\text{cm}^2$). Furthermore, the absorption and gain bandwidths are inhomogeneously broadened as a result of a Gaussian distribution of dot sizes in the absorber structure, which is beneficial for the generation of ultrashort laser pulses [11–13]. Femtosecond laser pulse generation using QD-SESAMs has been reported for a Cr:forsterite [12], Yb:KYW [14] and Ti:sapphire [17] laser crystals. These results, however, were limited in terms of power and pulse duration. In high power regime, the generation of watt-level sub-100 femtosecond laser pulses directly from the Yb-doped bulk crystal lasers has been reported for Yb:KGW [9,10], Yb:CALGO [18,19], Yb:CaF₂ [20–22] and Yb:Lu₂O₃ [23] using QW-SESAMs. However, the generated pulse width in the works with direct diode-pumping was limited to above 65 fs.

4.3. Multi-watt sub-100 fs mode-locked Yb:KGW laser: experiment and results

The laser used a 5 mm-long Yb:KGW crystal (cut along the N_g-axis) with 1.5% doping level in a Z-fold cavity, as shown in figure 4.1. The crystal was pumped at 980 nm by a 30 W fiber-coupled laser diode (100 μm core diameter, 0.22 NA) which was focused to a spot size of 300 μm in diameter by two achromatic doublets. The cavity configuration provided a mode size of around 280 μm which could be precisely tuned by changing the position of the output coupler that was mounted on a translation stage. This allowed for the introduction of the soft aperturing effect via the Kerr lensing into the laser cavity by making the laser mode size slightly larger than the pump spot size in the crystal (see section 2.5.2 in Chapter 2). The crystal absorbed 50–60% of the pump power depending on the pump power level. The thermal lens strength of the crystal at a pump power of 30 W (18 W absorbed) was estimated to be 10 diopters using a modified ABCD-matrix analysis (Appendix B) [24]. An output coupler with a transmission of 7.5% was used in the cavity.

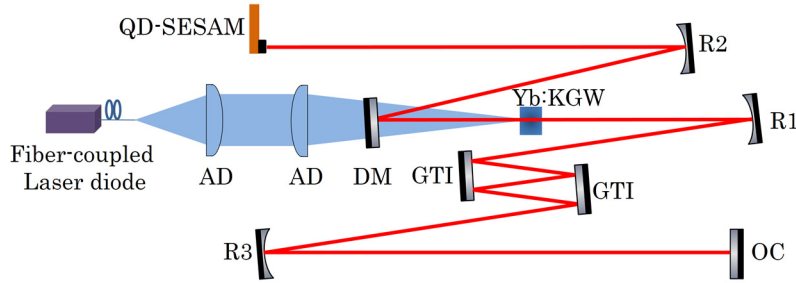


Figure 4.1. Experimental setup of a mode-locked Yb:KGW laser. AD, achromatic doublet; DM, dichroic mirror; R1-3, concave mirror; OC, output coupler. R1=300 mm, R2=300 mm, R3=500 mm.

For the mode-locked laser operation, two QD-SESAMs (grown by Innolume GmbH) with modulation depths of 0.7% and 0.5% (with seven and five pairs of InGaAs quantum-dot layers in the saturable structure, respectively), and a saturation fluence of $25 \mu\text{J}/\text{cm}^2$ [14] were used. They were provided to us by Prof. Edik Rafailov from Aston University, UK. These saturable absorbers exhibited recovery time with a sub-picosecond fast component. The absorbers were not water cooled and were used as one of the end mirrors. The beam spot size on them was designed to be initially around $350 \mu\text{m}$ in diameter. It was changing to a smaller size when the length of the arm at the output coupler side was reduced to introduce the Kerr lensing. Two Gires–Tournois interferometer mirrors (GTI, Layertec GmbH) provided negative dispersion to compensate for the positive dispersion of the crystal and for the induced chirp from self-phase modulation (SPM).

The laser cavity was initially optimized for the CW laser operation near the middle of the stability region. In this regime, the laser could deliver up to 5 W of output power. The HR mirror (Laseroptik GmbH) was then replaced by one of the QD-SESAMs, and the GTI mirrors were configured to provide a negative round-trip dispersion of -4400 fs^2 . With a QD-SESAM in the cavity, a Q-switched mode-locked laser regime was readily observed. At this point, the fluence on the absorber was $\sim 200 \mu\text{J}/\text{cm}^2$. By reducing the cavity length using the translation stage with an output coupler, a stable mode-locked laser with a spectral bandwidth of around 5 nm could be obtained.

At this point, the mode-locked laser was purely supported by the used QD-SESAM, and the mode-locked operation was completely self-starting. For this regime, the fluence on the QD-SESAM was around $240 \mu\text{J}/\text{cm}^2$. Further reduction of the cavity length resulted in multi-pulse

operation of the laser until a transition to a single pulse mode-locked laser regime could be observed. The latter transition indicated that the Kerr-lens mode locking regime came into effect, since the cavity mode size at this position was slightly larger than the pump beam size in the crystal. Introduction of the Kerr lensing was also accompanied by a continuous increase in the spectral width of the generated pulses. The transition sequence of the pulsed regimes as a result of reducing the cavity length was similar to the ones previously observed in [9,10]. Similarly, without the QD-SESAM in the cavity, no pure Kerr-lens mode locking could be achieved. Using the QD-SESAM with 0.7% modulation depth at the pump power of 30 W, the laser could deliver 90 fs pulses (see figure 4.2) with an average output power of 3.2 W at a repetition rate of 77 MHz. This corresponds to 462 kW of peak power and 41 nJ of pulse energy. The fluence on the absorber was around $340 \mu\text{J}/\text{cm}^2$. With the 0.5% modulation depth QD-SESAM, 93 fs long pulses with an average output power of 2.9 W at 76.9 MHz repetition rate, corresponding to 406 kW of peak power and 38 nJ of pulse energy, could be generated. The ripple in the spectrum was a known artifact of a spectrometer caused by a multi-mode fiber input, similar to the observation reported in [25]. It was caused by the multimode fiber connection to the optical spectrometer and was removed by replacing with a single-mode fiber in later experiments. A single pulse mode locking regime without instabilities was confirmed by monitoring the femtosecond-to-nanosecond time scales using a wide-range scan (200 ps) autocorrelator and a combination of fast oscilloscope/photodetector with a resolution of ~ 100 ps [26].

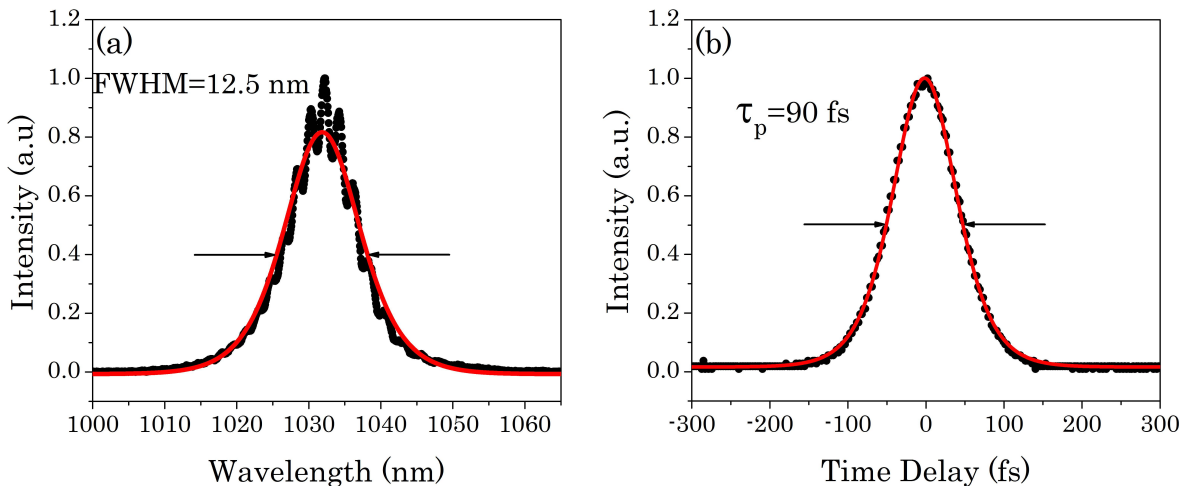


Figure 4.2. (a) The spectrum of the generated pulses with 0.7% QD-SESAM and (b) intensity autocorrelation. The red curves are the *sech*² shape fits. The time-bandwidth product was calculated to be 0.317. The ripple in the spectrum is a known artifact of the spectrometer.

The radio frequency (RF) spectrum of the 90 fs mode-locked laser is shown in figure 4.3. The spectral power of the fundamental mode was 50 dB above the noise level. In a wide-range RF scan measurement (figure 4.3(b)), no additional peaks between the higher order modes were observed, indicating clean mode locking. The drop of intensity of high-order harmonics in the RF spectrum was caused by the biasing conditions of the used photodetector and did not affect the observation of mode locking instabilities. The far-field beam intensity profile of the mode-locked laser which was near diffraction limited with $M^2 < 1.2$ is also shown in figure 4.3(c).

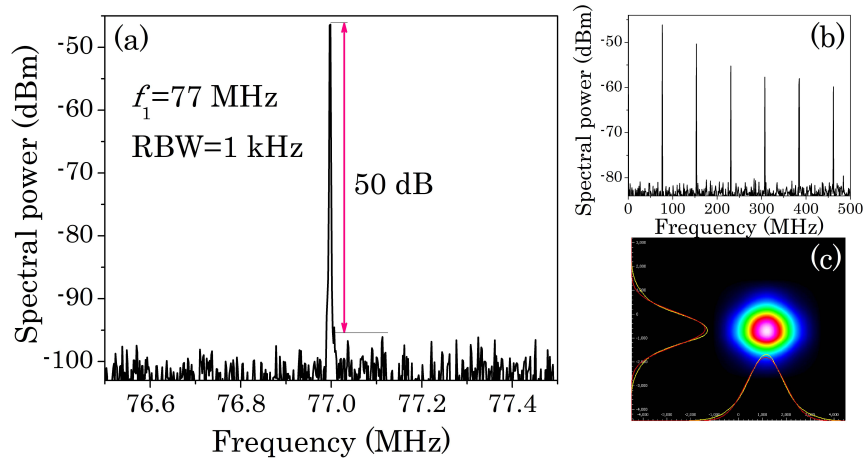


Figure 4.3. (a) RF spectrum of the pulse train with 0.7% QD-SESAM, (b) wide-span measurements. (c) Far-field beam intensity profile of the mode-locked laser. RBW: resolution bandwidth.

4.4. Watt-level sub-60 fs mode-locked Yb:KGW laser: experiment and results

In these experiments the laser oscillator used a 6 mm-long 1.6 at. % doped Yb:KGW crystal in a similar cavity as shown in figure 4.1. The pump was focused to a spot size of 340 μm by using two AR-coated achromatic doublets. The absorbed pump power was measured to be around 60%. The laser mode inside the crystal was estimated to be 290 μm in diameter using ABCD matrix analysis (Appendix B) and it could be gradually increased by adjusting the position of the output coupler mounted on a translation stage. In continuous-wave (CW) regime the laser could deliver up to 6 W of output power using an HR mirror as one of the end mirrors. The laser was polarized along the N_m -axis of the crystal. The total negative GDD of -3200 fs^2 per round trip was achieved by two bounces on a -550 fs^2 and -250 fs^2 GTI mirrors.

The mode-locked laser operation was initiated by using the QD-SESAM with a 0.5% modulation depth as the end mirror. A stable mode-locked laser with spectral bandwidth of 5-8 nm could be initially generated. The spectral bandwidth of the pulse depended on the pump power and the separation of the output coupler (OC) and the concave mirror R3 (figure 4.1). The output power was maximized for this regime and the fluence on the absorber was as high as $270 \mu\text{J}/\text{cm}^2$. Similar to the previous experiment, the Kerr lensing effect was then introduced by decreasing the OC-R3 distance using a translation stage. This corresponded to the increase of the laser mode size with respect to the pump beam in the crystal. During this procedure the laser underwent multi-pulse oscillation and the number of pulses per cavity round trip was reduced as the Kerr lensing effect became more pronounced. A careful adjustment of the pump power was needed during this transition regime. Once the Kerr lensing effect became sufficiently strong, a stable single-pulse mode-locked laser operation was obtained. With incident pump power of 18.3 W the laser delivered 56 fs pulses with an average output power of 1.95 W at the repetition rate of 77.3 MHz. This corresponds to 450 kW of peak power and 25 nJ of pulse energy. The FWHM spectral bandwidth of the laser was measured to be 20.5 nm with a central wavelength of 1040 nm as shown in figure 4.4. The time-bandwidth product (TBWP) was calculated to be 0.335. At this point the fluence on the saturable absorber was $370 \mu\text{J}/\text{cm}^2$.

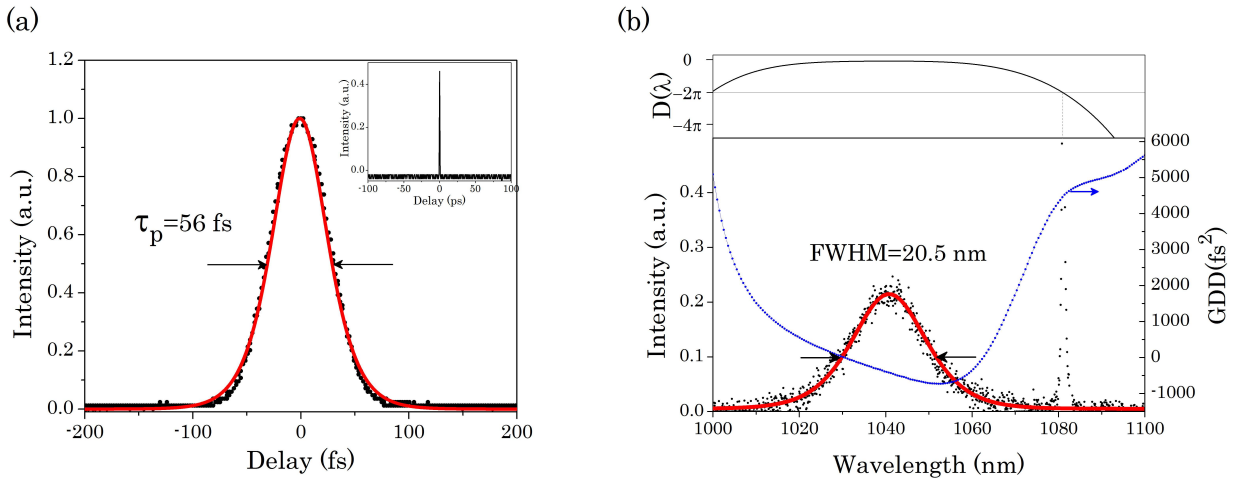


Figure 4.4. (a) Intensity autocorrelation of the mode-locked laser. Inset: wide-range scan (200 ps). (b) Spectrum of the mode-locked laser (black dotted curve), the calculated round-trip GDD (blue dotted curve) and the dispersive function $D(\lambda)$ (upper graph). The sech^2 -shape fits are shown as red solid curves.

The radio-frequency spectral power of the mode-locked laser confirmed the absence of the RF spectral sidebands around fundamental harmonic and also additional peaks between high order harmonics (figure 4.5). This indicated that Q-switched, Q-switched mode-locked regime and amplitude instability were absent in the generated laser pulse train. The signal to noise ratio was measured to be >45 dB.

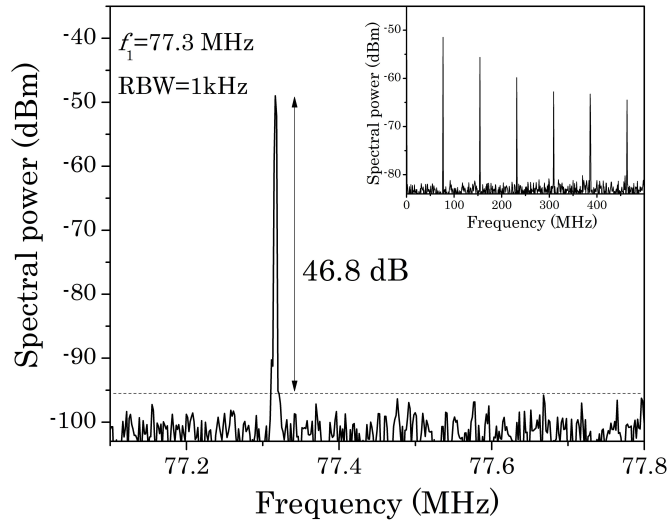


Figure 4.5. Radio-frequency spectral power of the mode-locked laser. Fundamental harmonic and (inset) wide-span measurement. RBW: resolution bandwidth.

The spectrum of the generated pulse was accompanied by a narrow spectral component at 1081 nm which corresponded to the existence of a dispersive wave (figure 4.4(b)). This dispersive wave, however, was not observed in the measurements performed by the oscilloscope and autocorrelator owing to its low intensity and correspondingly long duration. Indeed, the dispersive wave in normal dispersion regime is broadened due to the interplay of SPM and positive GVD at its oscillation wavelength. The net-GVD was calculated based on the available dispersion measurement data of the GTI mirrors, optical components and the Sellmeier coefficients (Appendix C) of an undoped KGW crystal [27]. The calculated positive GDD at the dispersive wave oscillation wavelength (1080 nm) was around $+4500$ fs². As can be seen in figure 4.4(b), the total GDD of the cavity rapidly shifted to the normal regime mainly due to the dispersion profile of the -550 fs² GTI mirror. The spectral energy of the dispersive wave was estimated to be 6.9% of the total spectral energy and its presence did not deteriorate the long-term stability of the mode-locked laser. The co-existence of dispersive waves with the main mode-locked pulse has been reported and analyzed previously [28–33]. These waves co-propagate with the main pulse and

some of the pulse energy is coupled out to the dispersive waves if they are phase-matched. The higher order dispersion coefficients have substantial effect in this regime. A general phase-matching condition can be expressed as [32],

$$D(\omega_n) = \sum_{m \geq 2} \left(\frac{\beta_m}{m!} (-1)^m \omega_n^m \right) + \frac{\beta_2}{2T^2} = \pm 2\pi j, \quad j = 0, 1, 2, \dots \quad \text{Eq.4.1}$$

where $\beta_m = \left. \frac{\partial^m \phi(\omega)}{\partial \omega^m} \right|_{\omega_0}$ are the dispersion coefficients, ω_0 is the carrier frequency, $\phi(\omega)$ is the phase delay per round-trip, ω_n is the dispersive wave frequency and $T = \tau/1.76$ where τ is the FWHM of the mode-locked pulse duration. The dispersion coefficients at carrier frequency (1041 nm) were calculated to be $\beta_2 = -430 \text{ fs}^2$, $\beta_3 = -21451 \text{ fs}^3$, $\beta_4 = -4.84 \times 10^6 \text{ fs}^4$ using the net-GVD data. For the measured pulse width of $\tau = 56 \text{ fs}$, the dispersive function (Eq.4.1) is plotted in figure 4.4(b) (upper curve). The resonance condition was satisfied at the wavelength where the observed dispersive wave was present, i.e., $D(\lambda = 1081 \text{ nm}) = -2\pi$. Other possible resonance wavelengths at longer or shorter wavelengths in normal GVD regime were not supported by the effective gain of the laser crystal in combination with the increasing loss of the output coupler and dichroic mirror at those wavelengths. In order to eliminate the dispersive wave, a flatter and broader anomalous GVD profile per round-trip for the intended wavelength range is required.

The performance of the laser was also investigated for different GDD and output coupler values (table 4.1). The pump power had to be adjusted because of different amount of loss incurred by different number of bounces on combinations of GTI mirrors. By increasing the total negative GDD, longer pulses were generated as expected [10]. The dispersive wave was not observed in case of net-GDD of -4800 fs^2 mainly due to the narrower spectrum of the laser around 1040 nm. With this value of GDD higher output power could be extracted from the laser cavity by using higher output coupling without significantly compromising the pulse width. For example, 90 fs pulses with 2.85 W of average output power were generated by using 10% output coupling and -4800 fs^2 GDD.

Table 4.1. Summary of the mode-locked Yb:KGW laser performance

GTI-GDD* (fs ²)	Output coupler (%)	Pulse width (fs)	Average output power (W)	Dispersive wave	Pump power** (W)
-3200	5	56	1.95	Yes	18.3
-3700	5	68	1.35	Yes	17.5
-4800	5	95	2	No	18.7
-4800	7.5	88	2.5	No	18.6
-4800	10	90	2.85	No	18.9

*The roundtrip net-GDD of GTI mirrors

**The incident pump power

4.5. Discussion

In this section the results of the two sets of experiments are compared and discussed. The mode-locked laser in the first experiment (section 4.3) was performed with a 5 mm-long Yb:KGW crystal (1.5 at. % Yb doping, N_g-cut) and the laser delivered 90 fs pulses with 3.2 W of output power by using a 0.7% QD-SESAM and 93 fs pulse with 2.9 W of output power by using a 0.5% QD-SESAM, respectively. The laser was polarized along the N_m-axis of the crystal and the net introduced GDD was -4400 fs². Due to the mechanical damage to the crystal, the second experiment was performed with the same laser cavity design but with a 6 mm-long Yb:KGW crystal (1.6 at. % Yb doping, N_g-cut) and similar pulses at high power level could be generated, i.e., 90 fs pulses with 2.85 W of output power with the N_m-polarization and using a net-GDD of -4800 fs². The higher GDD was required for compensating for the positive dispersion of the extra length of the used crystal (+200 fs²/mm). By reducing the net-GDD to -3200 fs² in this experiment, significantly shorter pulses of 56 fs with 1.95 W of output power could be generated. This showed the important role of dispersion compensation in a mode-locked laser, which has linear relation to the pulse width (Chapter 2). However, the output power for the obtained shorter pulses is lower than for the longer pulses mainly because of the increased influence of the nonlinear effects in the cavity, i.e. SPM and SAM, during the nonlinear dynamics of the pulse formation (Chapter 2, Eq. 2.5). Further increase of the pump power would result in single pulse brake-up into a multi-pulse oscillation. In addition, the longer length of the crystal in this experiment and therefore an increased level of SPM also contributed to the shortening of the pulse length to sub-60 fs regime by broadening of its spectrum.

The results of these two experiments compare favourably with all previous works (in terms of the peak power and the energy of the generated pulses) where QD-SESAMs were used for the generation of femtosecond pulses using Yb:KYW, Cr:forsterite, and Ti:sapphire laser crystals [12,14,17]. A summary of all reported results is compiled in figure 4.6. For example, the mode-locked Yb:KYW laser delivered 114 fs pulses with 500 mW of average output power (41 kW of peak power) and 200 fs pulses with a higher average power of 1.15 W (53.7 kW of peak power) [14]. Therefore, our highest power result (90 fs, 3.2 W, section 4.3) represents a ~ 2.8 times increase in output power and an ~ 8.6 times increase in peak power with respect to the previous results. In the sub-100 fs regime, these numbers rise to 58 and 140 times, respectively, when compared to Cr:forsterite [12]. The results for the shortest generated pulses (56 fs, 1.95 W, section 4.4) also showed enhancement in terms of pulse duration when compared to the previously reported KLAS mode-locked Yb:KGW laser based on a QW-SESAM, where 67 fs pulses with 3 W of output power were generated [9]. This can be explained by the increased level of SPM due to a longer crystal. Interestingly enough, the generated 56 fs pulses are also the shortest produced to date with the QD-SESAM absorbers (previously, 86 fs pulses were generated from Cr:forsterite laser [12]).

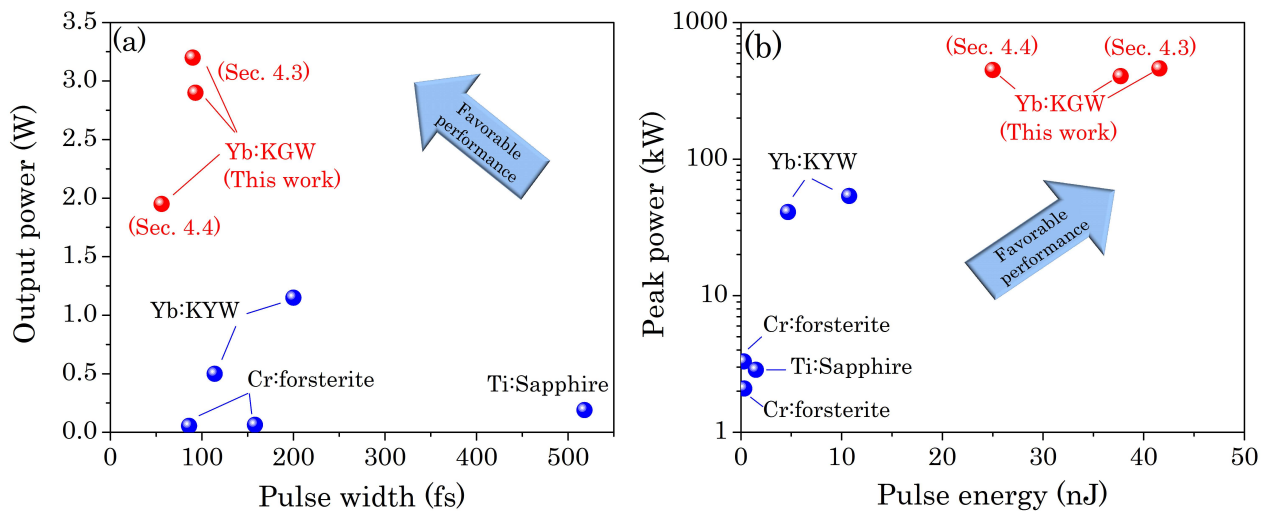


Figure 4.6. Current and previous mode-locked laser results with QD-SESAMs [12,14,17].

High power regime requires careful compensation of strong thermal lensing effect in Yb:KGW crystal. A promising candidate for this regime is Yb:CALGO crystal with thermal conductivity coefficient of 6.9 W/m/K and emission bandwidth of 80 nm [34]. For example, the

generation of 94 fs pulses with 12.5 W of average output power with SESAM mode locking was reported in [18]. Shorter pulses with duration of 40 fs at lower output power of 1.1 W were also demonstrated in this crystal by Kerr-lens mode locking technique [19]. Another promising Yb-doped laser crystal for generating high power sub-100 fs pulses is Yb:CaF₂ with thermal conductivity coefficient of 6 W/m/K and emission bandwidth of 30 nm [35,36]. Generation of 68 fs and 60 fs pulses with output powers of 2.3 W and 2.7 W using Kerr-lens mode locking has been reported in [21] and [20], respectively. It should be noted that results presented in [19,20] and [21] were not obtained with directly diode-pumped lasers which greatly reduces their overall efficiency and potential for further power scaling. Therefore, the use of commercially available laser diodes for direct diode pumping is a desired feature due to the reduced cost and complexity of the laser system. A diode-pumped SESAM mode-locked Yb:CaF₂ laser was also demonstrated, delivering 87 fs pulses with 1.4 W of output power [22]. A new laser crystal, Yb³⁺:Lu₂O₃, with thermal conductivity of 11 W/m/K and emission bandwidth of 13 nm has also shown its potential in this regime [37] and the generation of 71 fs pulses with 1.09 W of average power was reported with this crystal in [23]. Watt-level sub-100 fs pulse generation was also reported for Yb:YVO₄ and Yb:KYW using the KLM technique in [38]. A comparison of performance of the diode-pumped Yb-lasers in the sub-100 fs regime is shown in Figure 4.7. As can be seen, the generated 56 fs pulses with 450 kW of peak power in our work demonstrate more than one order of magnitude higher average and peak powers when compared to the previous sub-60 fs diode-pumped Yb-lasers [39–43]. The generated pulses in our work (section 4.4) are the shortest pulses generated from the monoclinic double tungstate crystals (and Yb:KGW laser crystal in particular) and the most powerful in the sub-60 fs regime. When comparing to the previous work on Yb:KGW laser in [44] delivering 59 fs pulses with 62 mW of output power, our result demonstrates significant enhancement in terms of output power. At the same time they are also the shortest pulses produced to date with the help of a quantum-dot-based saturable absorber. We believe that such a powerful ultrashort pulse laser source will be attractive for nonlinear frequency conversion into the visible and near-infrared ranges [45–47].

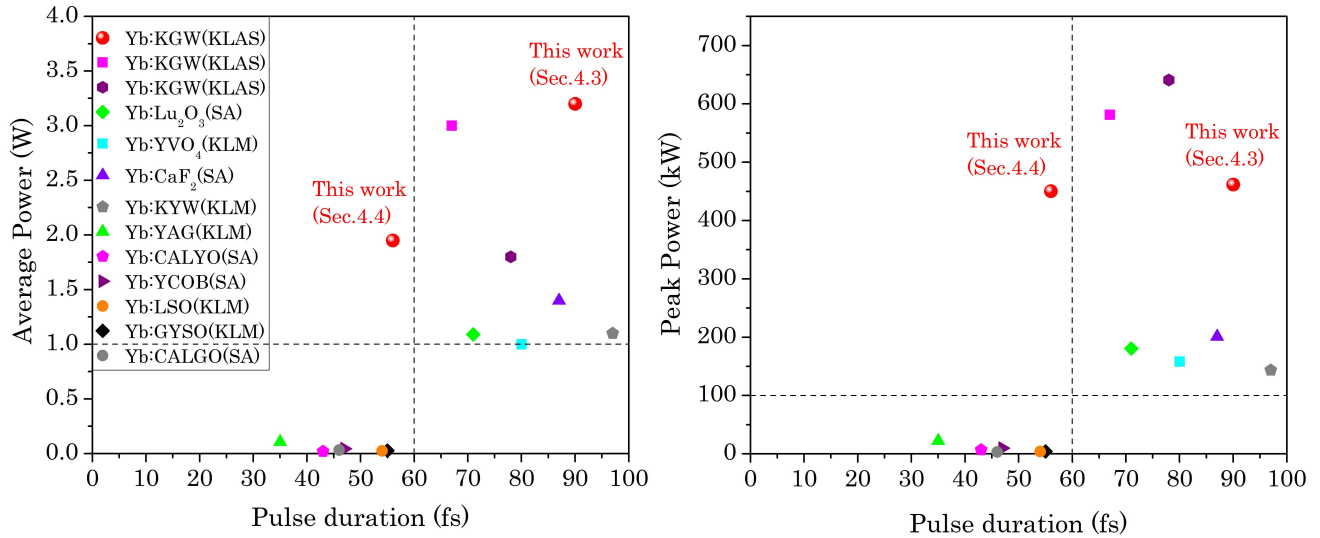


Figure 4.7. A comparison of sub-100 fs diode-pumped bulk Yb-doped crystal lasers [9,10,22,23,38–43,48]. Data from Ref. [18] are not shown for scaling reasons to better visualize the <90 fs regime. SA: SESAM.

4.6. Conclusion

In this chapter, the generation of high power ultrashort pulses from diode-pumped Yb:KGW mode-locked lasers was demonstrated. The mode locking technique was based on the dual action of a quantum-dot saturable absorber mirror and the Kerr lensing effect (KLAS mode locking). The quantum-dot saturable absorber was used for initiation and initial pulse forming and the Kerr lensing effect was employed for further pulse shortening into the sub-100 fs regime. In section 4.3, the resultant mode-locked laser delivered 90 fs pulses with an average output power of 3.2 W by using a QD-SESAM with the modulation depth of 0.7%. This corresponded to 462 kW of peak power and 41 nJ of pulse energy. With the same laser system and a QD-SESAM with the modulation depth of 0.5%, 93 fs pulses with 2.9 W of average power and 406 kW of peak power (38 nJ of pulse energy) could be generated. Our results showed remarkably higher average output and pulse peak powers when compared to the previous works with QD-SESAMs and also the highest power among the sub-100 fs bulk Yb-doped crystals, except for the Yb:CALGO result in [18].

The generation of shorter pulses was possible by reducing the net-GDD in the laser cavity at the expense of output power. A high power sub-60 fs Yb:KGW laser mode-locked using KLAS

mode locking with QD-SESAM was demonstrated in section 4.4. The laser delivered 56 fs pulses with 1.95 W of average power, which is, to the best of our knowledge, the shortest pulse duration generated from the monoclinic double tungstate crystals and the Yb:KGW crystal in particular. The output average and peak powers were an order of magnitude higher than the previously reported values. The spectral bandwidth of the mode-locked laser was 20.5 nm which was near the emission bandwidth limit of the Yb:KGW laser crystal (~25 nm). The pulse duration was limited by the appearance of the dispersive wave at longer wavelength which was caused by the increased level of uncompensated dispersion. This fact and the underutilized emission bandwidth point out to the possibility of generation of even shorter pulses from this crystal. This can be achieved by more careful dispersion management.

References

1. A. Major, D. Sandkuijl, and V. Barzda, "Efficient frequency doubling of a femtosecond Yb:KGW laser in a BiB₃O₆ crystal," *Opt. Express* **17**, 12039 (2009).
2. D. Sandkuijl, R. Cisek, A. Major, and V. Barzda, "Differential microscopy for fluorescence-detected nonlinear absorption linear anisotropy based on a staggered two-beam femtosecond Yb:KGW oscillator," *Biomed. Opt. Express* **1**, 895 (2010).
3. R. Akbari and A. Major, "Optical, spectral and phase-matching properties of BIBO, BBO and LBO crystals for optical parametric oscillation in the visible and near-infrared wavelength ranges," *Laser Phys.* **23**, 35401 (2013).
4. A. Major, F. Yoshino, J. S. Aitchison, P. W. E. Smith, E. Sorokin, and I. T. Sorokina, "Ultrafast nonresonant third-order optical nonlinearities in ZnSe for photonic switching at telecom wavelengths," *Appl. Phys. Lett.* **85**, 4606 (2004).
5. S. R. Bowman, S. P. O'Connor, and S. Biswal, "Ytterbium laser with reduced thermal loading," *IEEE J. Quantum Electron.* **41**, 1510–1517 (2005).
6. W. F. Krupke, "Ytterbium solid-state lasers. The first decade," *IEEE J. Sel. Top. Quantum Electron.* **6**, 1287–1296 (2000).
7. P. A. Loiko, K. V. Yumashev, N. V. Kuleshov, and A. A. Pavlyuk, "Thermo-optical properties of pure and Yb-doped monoclinic KY(WO₄)₂ crystals," *Appl. Phys. B* **106**, 663–668 (2012).
8. U. Keller, "Ultrafast solid-state laser oscillators: a success story for the last 20 years with no end in sight," *Appl. Phys. B* **100**, 15–28 (2010).
9. H. Zhao and A. Major, "Powerful 67 fs Kerr-lens mode-locked prismless Yb:KGW oscillator," *Opt. Express* **21**, 31846 (2013).
10. H. Zhao and A. Major, "Megawatt peak power level sub-100 fs Yb:KGW oscillators," *Opt. Express* **22**, 30425 (2014).
11. E. U. Rafailov, M. A. Cataluna, and W. Sibbett, "Mode-locked quantum-dot lasers," *Nat. Photonics* **1**, 395–401 (2007).
12. A. A. Lagatsky, C. G. Leburn, C. T. A. Brown, W. Sibbett, S. A. Zolotovskaya, and E. U. Rafailov, "Ultrashort-pulse lasers passively mode locked by quantum-dot-based saturable absorbers," *Prog. Quantum Electron.* **34**, 1–45 (2010).
13. E. U. Rafailov, S. J. White, A. A. Lagatsky, A. Miller, W. Sibbett, D. A. Livshits, A. E. Zhukov, and V. M. Ustinov, "Fast Quantum-Dot Saturable Absorber for Passive Mode Locking of Solid-State Lasers," *IEEE Photonics Technol. Lett.* **16**, 2439–2441 (2004).
14. A. A. Lagatsky, F. M. Bain, C. T. A. Brown, W. Sibbett, D. A. Livshits, G. Erbert, and E. U. Rafailov, "Low-loss quantum-dot-based saturable absorber for efficient femtosecond pulse generation," *Appl. Phys. Lett.* **91**, 231111 (2007).
15. N. Meiser, K. Seger, V. Pasiskevicius, H. Jang, E. Rafailov, and I. Krestnikov, "Gigahertz repetition rate mode-locked Yb:KYW laser using self-assembled quantum dot saturable absorber," *Appl. Phys. B* **110**, 327–333 (2013).
16. U. Keller, K. J. Weingarten, F. X. Kartner, D. Kopf, B. Braun, I. D. Jung, R. Fluck, C. Honninger, N. Matuschek, and J. Aus der Au, "Semiconductor saturable absorber mirrors (SESAM's) for femtosecond to nanosecond pulse generation in solid-state lasers," *IEEE J. Sel. Top. Quantum Electron.* **2**, 435–453 (1996).
17. V. G. Savitski, P. J. Schlosser, J. E. Hastie, A. B. Krysa, J. S. Roberts, M. D. Dawson, D. Burns, and S. Calvez, "Passive Mode-Locking of a Ti:sapphire Laser by InGaP Quantum-

- Dot Saturable Absorber," *IEEE Photonics Technol. Lett.* **22**, 209–211 (2010).
18. A. Greborio, A. Guandalini, and J. Aus der Au, "Sub-100 fs pulses with 12.5-W from Yb:CALGO based oscillators," in *SPIE Proceedings* **8235**, p. 823511 (2012).
 19. P. Sevillano, P. Georges, F. Druon, D. Descamps, and E. Cormier, "32-fs Kerr-lens mode-locked Yb:CaGdAlO₄ oscillator optically pumped by a bright fiber laser," *Opt. Lett.* **39**, 6001 (2014).
 20. P. Sevillano, G. Machinet, R. Dubrasquet, P. Camy, J.-L. Doualan, R. Moncorge, P. Georges, F. P. Druon, D. Descamps, and E. Cormier, "Sub-50 fs, Kerr-lens mode-locked Yb:CaF₂ laser oscillator delivering up to 2.7 W," in *Advanced Solid-State Lasers Congress (OSA, 2013)*, p. AF3A.6.
 21. G. Machinet, P. Sevillano, F. Guichard, R. Dubrasquet, P. Camy, J.-L. Doualan, R. Moncorgé, P. Georges, F. Druon, D. Descamps, and E. Cormier, "High-brightness fiber laser-pumped 68 fs–2.3 W Kerr-lens mode-locked Yb:CaF₂ oscillator," *Opt. Lett.* **38**, 4008 (2013).
 22. F. Pirzio, S. D. Di Dio Cafiso, M. Kemnitzer, F. Kienle, A. Guandalini, J. Aus der Au, and A. Agnesi, "65-fs Yb:CaF₂ laser mode-locked by semiconductor saturable absorber mirror," *J. Opt. Soc. Am. B* **32**, 2321 (2015).
 23. M. Tokurakawa, A. Shirakawa, K. Ueda, R. Peters, S. T. Fredrich-Thornton, K. Petermann, and G. Huber, "Ultrashort pulse generation from diode pumped mode-locked Yb³⁺:sesquioxide single crystal lasers," *Opt. Express* **19**, 2904 (2011).
 24. H. Mirzaeian, S. Manjooran, and A. Major, "A simple technique for accurate characterization of thermal lens in solid state lasers," in *SPIE Proceedings* **9288**, pp. 928802–1 (2014).
 25. W. Schneider, A. Ryabov, C. Lombosi, T. Metzger, Z. Major, J. A. Fülöp, and P. Baum, "800-fs, 330-μJ pulses from a 100-W regenerative Yb:YAG thin-disk amplifier at 300 kHz and THz generation in LiNbO₃," *Opt. Lett.* **39**, 6604 (2014).
 26. T. Waritanant and A. Major, "High efficiency passively mode-locked Nd:YVO₄ laser with direct in-band pumping at 914 nm," *Opt. Express* **24**, 12851 (2016).
 27. M. C. Pujol, M. Rico, C. Zaldo, R. Solé, V. Nikolov, X. Solans, M. Aguiló, and F. Díaz, "Crystalline structure and optical spectroscopy of Er³⁺-doped KGd(WO₄)₂ single crystals," *Appl. Phys. B* **68**, 187–197 (1999).
 28. M. J. P. Dymott and A. I. Ferguson, "Pulse duration limitations in a diode-pumped femtosecond Kerr-lens mode-locked Cr:LiSAF laser," *Appl. Phys. B Lasers Opt.* **65**, 227–234 (1997).
 29. F. Salin, P. Grangier, P. Georges, and A. Brun, "Pulse propagation near zero group-velocity dispersion in a femtosecond dye laser," *Opt. Lett.* **15**, 1374 (1990).
 30. S. Ozharar, I. Baylam, M. N. Cizmeciyan, O. Balci, E. Pince, C. Kocabas, and A. Sennaroglu, "Graphene mode-locked multipass-cavity femtosecond Cr⁴⁺:forsterite laser," *J. Opt. Soc. Am. B* **30**, 1270 (2013).
 31. V. L. Kalashnikov, E. Sorokin, and I. T. Sorokina, "Mechanisms of spectral shift in ultrashort-pulse laser oscillators," *J. Opt. Soc. Am. B* **18**, 1732 (2001).
 32. Q. Lin and I. Sorokina, "High-order dispersion effects in solitary mode-locked lasers: side-band generation," *Opt. Commun.* **153**, 285–288 (1998).
 33. P. F. Curley, C. Spielmann, T. Brabec, F. Krausz, E. Wintner, and A. J. Schmidt, "Operation of a femtosecond Ti:sapphire solitary laser in the vicinity of zero group-delay dispersion," *Opt. Lett.* **18**, 54 (1993).

34. J. Petit, P. Goldner, and B. Viana, "Laser emission with low quantum defect in Yb:CaGdAlO₄," *Opt. Lett.* **30**, 1345 (2005).
35. M. Siebold, S. Bock, U. Schramm, B. Xu, J. L. Doualan, P. Camy, and R. Moncorgé, "Yb:CaF₂ — a new old laser crystal," *Appl. Phys. B* **97**, 327–338 (2009).
36. J. Boudeile, J. Didierjean, P. Camy, J. L. Doualan, A. Benayad, V. Ménard, R. Moncorgé, F. Druon, F. Balembois, and P. Georges, "Thermal behaviour of ytterbium-doped fluorite crystals under high power pumping," *Opt. Express* **16**, 10098 (2008).
37. U. Griebner, V. Petrov, K. Petermann, and V. Peters, "Passively mode-locked Yb:Lu₂O₃ laser," *Opt. Express* **12**, 3125 (2004).
38. F. M. Bain, A. A. Lagatsky, C. T. A. Brown, and W. Sibbett, "High-power Kerr-lens mode-locked ytterbium lasers," in *SPIE Proceedings* **6871**, p. 68712L (2008).
39. A. Yoshida, A. Schmidt, V. Petrov, C. Fiebig, G. Erbert, J. Liu, H. Zhang, J. Wang, and U. Griebner, "Diode-pumped mode-locked Yb:YCOB laser generating 35 fs pulses," *Opt. Lett.* **36**, 4425 (2011).
40. A. Agnesi, A. Greborio, F. Pirzio, G. Reali, J. Aus der Au, and A. Guandalini, "40-fs Yb³⁺:CaGdAlO₄ laser pumped by a single-mode 350-mW laser diode," *Opt. Express* **20**, 10077 (2012).
41. F. Pirzio, S. D. D. D. Cafiso, M. Kemnitzer, A. Guandalini, F. Kienle, S. Veronesi, M. Tonelli, J. Aus der Au, and A. Agnesi, "Sub-50-fs widely tunable Yb:CaYAlO₄ laser pumped by 400-mW single-mode fiber-coupled laser diode," *Opt. Express* **23**, 9790 (2015).
42. J. Zhu, Z. Gao, W. Tian, J. Wang, Z. Wang, Z. Wei, L. Zheng, L. Su, and J. Xu, "Kerr-Lens Mode-Locked Femtosecond Yb:GdYSiO₅ Laser Directly Pumped by a Laser Diode," *Appl. Sci.* **5**, 817–824 (2015).
43. W.-L. Tian, Z.-H. Wang, J.-F. Zhu, Z.-Y. Wei, L.-H. Zheng, X.-D. Xu, and J. Xu, "Generation of 54 Fs Laser Pulses from a Diode Pumped Kerr-Lens Mode-Locked Yb:LSO Laser," *Chinese Phys. Lett.* **32**, 24206 (2015).
44. M. Kowalczyk, J. Sotor, and K. M. Abramski, "59 fs mode-locked Yb:KGW oscillator pumped by a single-mode laser diode," *Laser Phys. Lett.* **13**, 35801 (2016).
45. H. Zhao, I. T. Lima, and A. Major, "Near-infrared properties of periodically poled KTiOPO₄ and stoichiometric MgO-doped LiTaO₃ crystals for high power optical parametric oscillation with femtosecond pulses," *Laser Phys.* **20**, 1404–1409 (2010).
46. I. T. Lima, V. Kultavewuti, and A. Major, "Phasematching properties of congruent MgO-doped and undoped periodically poled LiNbO₃ for optical parametric oscillation with ultrafast excitation at 1 μm," *Laser Phys.* **20**, 270–275 (2010).
47. S. Manjooran, H. Zhao, I. T. Lima, and A. Major, "Phase-matching properties of PPKTP, MgO:PPSLT and MgO:PPcLN for ultrafast optical parametric oscillation in the visible and near-infrared ranges with green pump," *Laser Phys.* **22**, 1325–1330 (2012).
48. S. Uemura and K. Torizuka, "Sub-40-fs Pulses from a Diode-Pumped Kerr-Lens Mode-Locked Yb-Doped Yttrium Aluminum Garnet Laser," *Jpn. J. Appl. Phys.* **50**, 10201 (2011).

Chapter 5

High power femtosecond pure Kerr-lens mode-locked Yb:KGW laser

5.1. Introduction

In this chapter, the generation of high power ultra-short pulses from a Yb:KGW laser pumped by a multimode fibre-coupled laser diode and by using the Kerr-lens mode locking technique is demonstrated for the first time to our knowledge. The main goal of this experiment was to generate watt-level femtosecond pulses directly from a purely Kerr-lens mode-locked laser, while eliminating the saturable absorber mirror due to the cost and its tendency to damage. However, it comes at the expense of designing the laser cavity near the stability boundary and arduous cavity alignment procedure. A brief introduction on this regime of mode locking and a review on the preceding work are provided below. In the following section the experimental results are presented. The laser delivered 240 fs pulse with 2.3 W of average output power (110 kW of peak power and 26 nJ of pulse energy). The shortest generated pulse duration was 120 fs with 1.2 W of output power and the self-starting regime was also demonstrated. The laser exhibited more than an order of magnitude higher output power when compared to the previously reported bulk Yb-ion doped lasers with multimode laser diode pumping systems. In the discussion section, the oscillator performance in terms of the Kerr-lens mode locking sensitivity is investigated and the limiting factor to the laser operation is discussed. Also, a comprehensive comparison between our work and previous results is provided. Finally, a summary of the experiments and achievements is provided.

5.2. Mode-locked laser based on Kerr lensing effect

In the previous chapter, the generation of high power ultrashort pulses from diode-pumped Yb:KGW laser oscillators based on dual-action of quantum-dot saturable absorber mirror and Kerr

lensing effect was demonstrated. The mode locking of these lasers by using the QD-SESAMs provided self-starting operation and the design procedure was flexible, but saturable absorbers are susceptible to damage and are costly. Therefore, elimination of SESAMs from the laser oscillator is desired. Kerr-lens mode locking (KLM) of a laser, on the other hand, offers a fast saturable absorber-like loss modulation and results in a considerable pulse shortening at the expense of designing the laser cavity near its stability boundary and requires tedious alignment procedure. Furthermore, high power operation of the laser can be strongly affected by a considerable thermal lensing effect, which needs to be considered in the design procedure.

Femtosecond pure Kerr-lens mode-locked bulk lasers have been reported in a variety of laser crystals, including Yb-doped crystals such as Yb:KYW [1–5], Yb:CALGO [6], Yb:CALYO [7], Yb:YVO₄ [8,9], and Cr-doped crystals such as Cr:forsterite [10]; Cr:ZnSe [11] and Cr:YAG [12], and Ti:sapphire [13]. Nevertheless, only a few watt-level KLM lasers have been reported, for example, with Yb:CaF₂ [14,15], Yb:CALGO [16] Yb:YVO₄ [9] and Yb:KYW [9] crystals, which were not directly diode-pumped by the widely used fiber-coupled pump modules. Indeed, output powers exceeding 1 W were exclusively reported for lasers that used high brightness pump sources with $M^2 \leq 3$ [9,14-16]. At the same time KLM bulk lasers with multimode pumping ($M^2 > 20$) typically could deliver only an order of magnitude lower output powers [5-7,29-34]. These facts were caused by the current lack of powerful high brightness pump sources similar to those that are widely used for KLM operation of Ti:sapphire lasers.

In this work, we investigated the development of a high-power diode-pumped pure KLM Yb:KGW laser. In contrast to the previous high power works [9,14-16], the laser was pumped by a conventional multimode ($M^2 \approx 40$) fiber-coupled laser diode and delivered 240 fs pulses with 2.3 W of output power at the repetition rate of 86.8 MHz, corresponding to 110 kW of peak power and 26 nJ of pulse energy. Shorter pulses of 120 fs with 1.2 W of average output power were also generated. The self-starting operation of the oscillator was demonstrated. The limiting factor to the laser operation was the appearance of a strong continuous wave (CW) component in the mode-locked laser spectrum. To the best of our knowledge, this is the first demonstration of a femtosecond Yb-ion doped KLM bulk laser that produced >1 W of average output power with highly multimode pump source.

5.3. Experiment and results

A 6-mm-long N_g -cut Yb:KGW crystal doped with 1.6 at. % Yb was used in a cavity similar to the previous mode-locked laser oscillators in Chapter 4 (figure 5.1). The crystal was pumped by the same fiber-coupled laser diode (100 μm , 0.22 NA) with a maximum power of 30 W at 980 nm. The pump beam was imaged to a spot size of 320 μm in the crystal by using two AR-coated achromatic doublets. The absorption of the pump power was measured to be around 60% of the incident power on the crystal. For the initial alignment, the cavity mode size inside the crystal was estimated to be 290 μm in diameter without the Kerr lensing effect using the ABCD matrix analysis. The output coupler was mounted on a translation stage so that the laser beam size could be varied in the crystal with respect to the pump by reducing the OC-R3 separation. The laser could deliver up to 6 W of average power in continuous-wave regime with the polarization along the N_m -axis of the crystal. The strength of thermal lens in the crystal for the operating range of pump power was measured to be around 100-150 mm of equivalent focal length [17]. Gires-Tournois interferometer mirrors (GTI, Layertec GmbH) were used in order to compensate for the positive group velocity dispersion (GVD) of the crystal and optical components, as well as the self-phase modulation (SPM). All other cavity optics was designed to exhibit low dispersion at the laser wavelengths (Laseroptik GmbH).

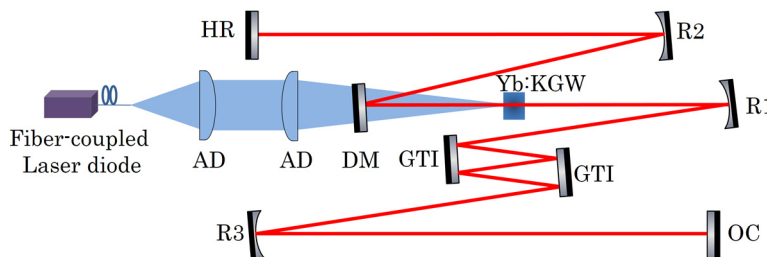


Figure 5.1. Experimental setup of the Kerr-lens mode-locked Yb:KGW laser. AD, achromatic doublets; DM: dichroic mirror; R1-3: concave mirrors; OC: output coupler. R1=300 mm, R2=300 mm and R3=500 mm.

In order to compensate for the positive dispersion two GTI mirrors with -1300 fs^2 GDD were used and a round-trip negative GDD of -10400 fs^2 was achieved by two bounces on each mirror. The laser was aligned for the highest CW power with 10% output coupling. By carefully

adjusting the position of mirror R2 and R3-OC separation a single pulse mode-locked laser was achieved. Our simulation showed that at this point (i.e. without the Kerr lensing effect) the cavity mode size reached the same size as the pump beam size and its size was reduced by about $10\ \mu\text{m}$ with the Kerr lensing effect. The mechanical perturbation that was required for the initiation of mode locking was produced by moving of the mirror R2. The single pulse oscillation per round trip was confirmed by using a fast oscilloscope/photodetector with a temporal resolution of 100 ps in combination with a wide-range scan (200 ps) autocorrelation [18]. The laser initially delivered 335 fs pulses with 4.65 W of average output power at 18.7 W of incident pump power (figure 5.2). The spectral bandwidth of the pulse at half maximum was 3.4 nm and a strong CW component was accompanying the mode-locked laser spectrum (see figure 5.2(b)). The CW component could be suppressed by reducing the pump power to 16.2 W and introducing some adjustment to the cavity alignment by tilting the HR mirror. At this point, the laser delivered 240 fs pulses with 2.3 W of average output power at the repetition rate of 86.8 MHz, corresponding to 110 kW of peak power and 26 nJ of pulse energy. The optical-to-optical efficiency was 14% which is quite typical for mode-locked lasers. The spectrum of the pulse was 4.7 nm wide with the central wavelength of 1031 nm (figure 5.3). The radio frequency (RF) spectrum showed a large signal-to-noise ratio of $>60\ \text{dB}$ for the fundamental RF harmonic without spectral sidebands which indicated the absence of Q-switched mode locking regime (figure 5.3(c)). The wide-span RF measurement exhibited no signs of additional peaks between the higher RF harmonics and therefore confirmed that no secondary pulses were present.

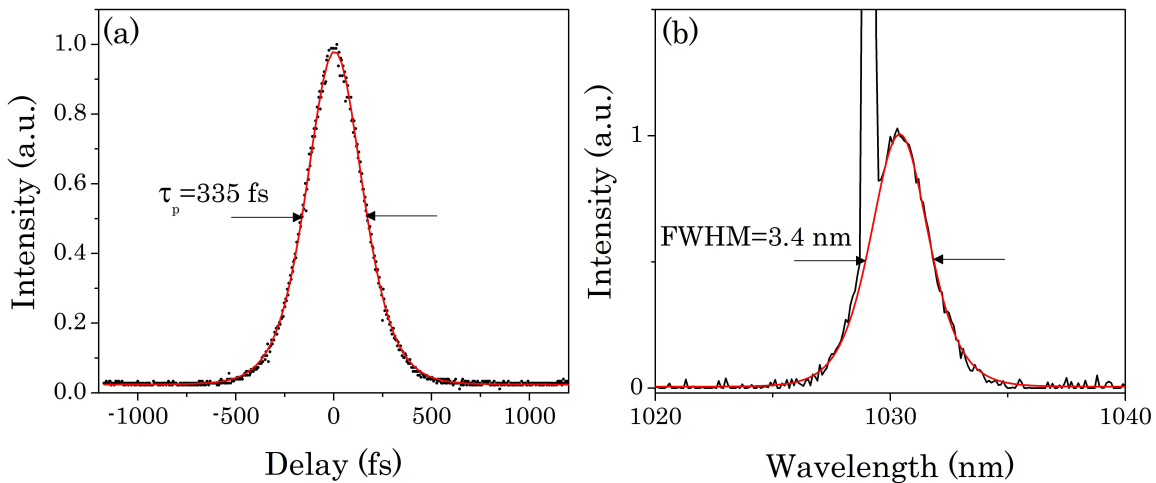


Figure 5.2. (a) Intensity autocorrelation of the mode-locked laser with CW component. (b) The corresponding mode-locked laser spectrum. The sech^2 -shape fits are shown as red solid curves.

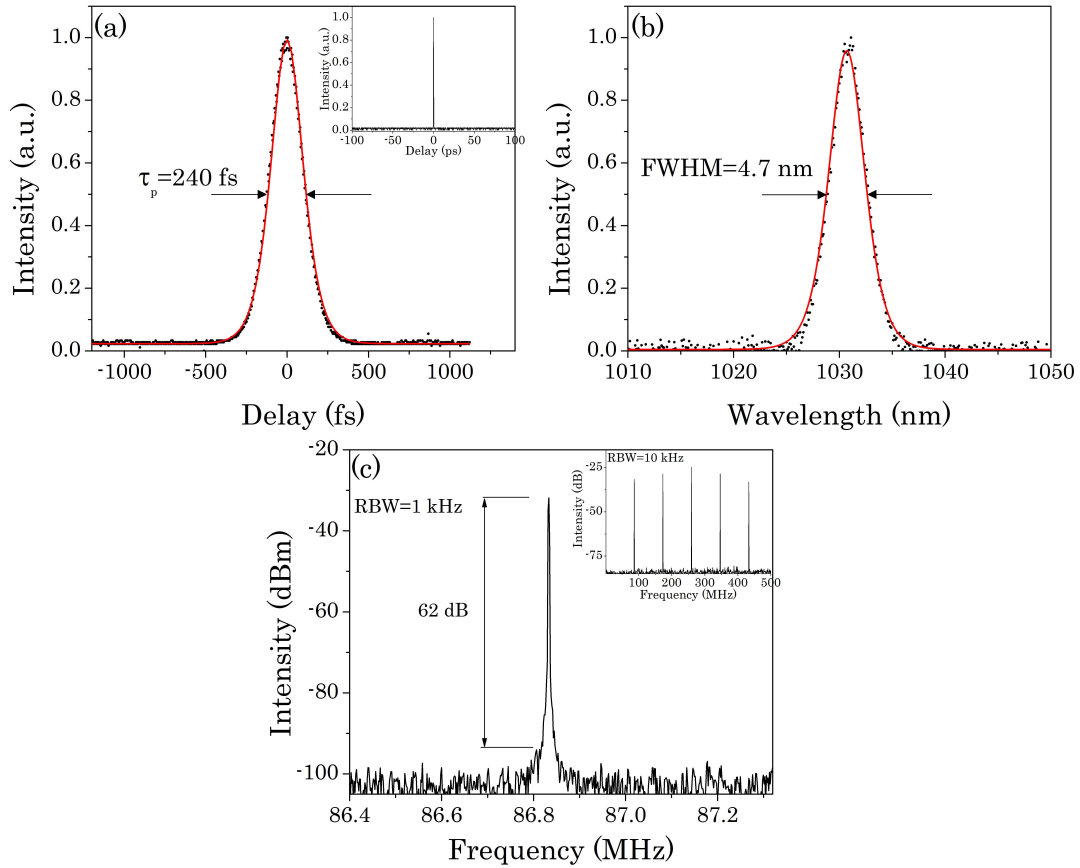


Figure 5.3. (a) Intensity autocorrelation of 240 fs pulse. Inset: wide-range scan of 200 ps. (b) The corresponding mode-locked laser spectrum. (c) Radio frequency spectral power. Inset: the wide-span RF measurement. The $sech^2$ -shape fits are shown as red solid curves. RBW: resolution bandwidth.

The mode-locked laser with the shortest pulse duration was obtained by using a 7.5% output coupler and a round-trip GDD of -5600 fs^2 , which was achieved through four bounces on the -1300 fs^2 and -100 fs^2 GTI mirrors. At the incident pump power of 17 W, the laser initially operated in the mode-locked regime with a CW component. It produced 3.6 W of average output power with a $\sim 5 \text{ nm}$ wide spectrum. By reducing the pump power to 14 W and adjusting alignment of the cavity, the CW component was eliminated and the laser delivered 120 fs pulses with 1.2 W of average output power. The spectral bandwidth of the pulse became 9.5 nm with the central wavelength of 1038.5 nm (see figure 5.4).

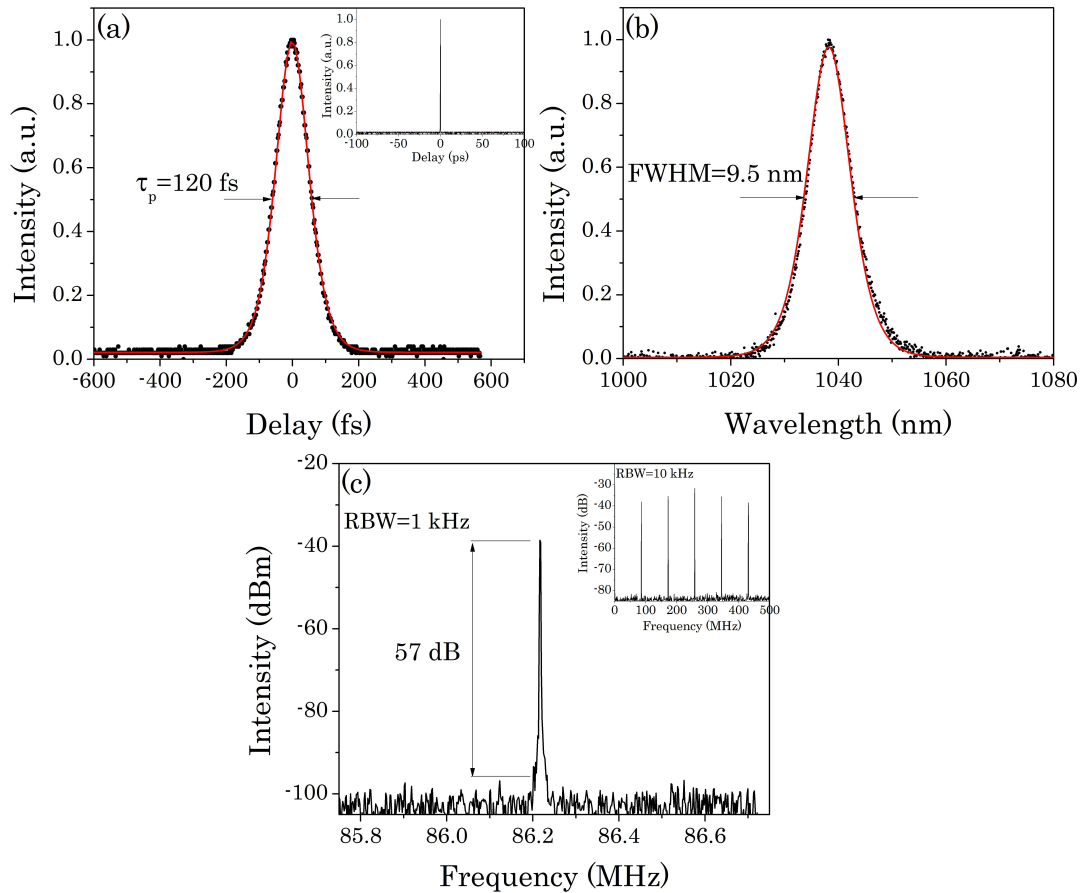


Figure 5.4. (a) Intensity autocorrelation of 120 fs pulse. Inset: wide-range scan of 200 ps. (b) The corresponding mode-locked laser spectrum. (c) Radio frequency spectral power. Inset: the wide-span RF measurement. The $sech^2$ -shape fits are shown as red solid curves. RBW: resolution bandwidth.

A self-starting mode-locked laser operation was also realized by reducing the output coupling to 5% and using the same amount of negative GDD in the cavity (i.e. -5600 fs^2). At the pump power of 14.8 W, the laser delivered 120 fs pulses with 1.7 W of output power. The self-starting was confirmed by temporary blocking and unblocking of the laser cavity. In some cases, the laser could start oscillation in multi-pulse regime but switched to a single pulse oscillation after a few seconds. In case of the self-starting mode-locked laser, the spectrum of the pulse was accompanied by a CW component which could not be suppressed.

The performance of the mode-locked laser was also investigated for smaller values of GDD. However, the CW component in the spectrum could not be eliminated and the measured pulse

duration did not appreciably change. A summary of laser performance for all values of GDD is shown in table 5.1.

Table 5.1. A summary of the KLM laser performance.

GDD (fs ²)	OC %	Pump power (W)	Pulse width (fs)	Output power (W)
-4000	10	17.6	120	2.9 ^(a)
-4400	10	17.3	120	2.6 ^{(a),(b)}
-5600	5	14.8	120	1.7 ^{(a),(b)}
-5600	7.5	14	120	1.2
-5600	10	15.5	135	1.7
-6750	7.5	14.1	147	1.35
-10400	10	16.2	240	2.3

^(a) with CW component

^(b) self-starting

5.4. Discussion

First, the strength of the Kerr lens mode locking of a resonator was evaluated by calculating the Kerr sensitivity parameter, which was defined by Magni et al. [19]. It describes a relative variation of the laser mode size due to the Kerr lensing effect (Appendix D). In order to have an effective discrimination between the CW laser mode and the self-focused laser mode which is induced by the Kerr lensing effect, a large and negative value of the sensitivity is required (i.e. the laser mode size should get smaller for more effective soft aperturing effect). We adopted the analysis for the case of a soft-aperture mode locking. In figure 5.5, the negative sensitivity values for the upper stability region are shown as contours in terms of the folding mirrors separation (R1-R2) and the laser crystal position with respect to the mirror R2. The thermal lensing effect was included in the calculation. The operating point of the cavity was located near the stability boundary (shown as a red spot) but the mode-locked laser did not drift into the unstable condition. The Kerr sensitivity parameter was calculated to be -0.11 which was high enough for a reliable mode locking.

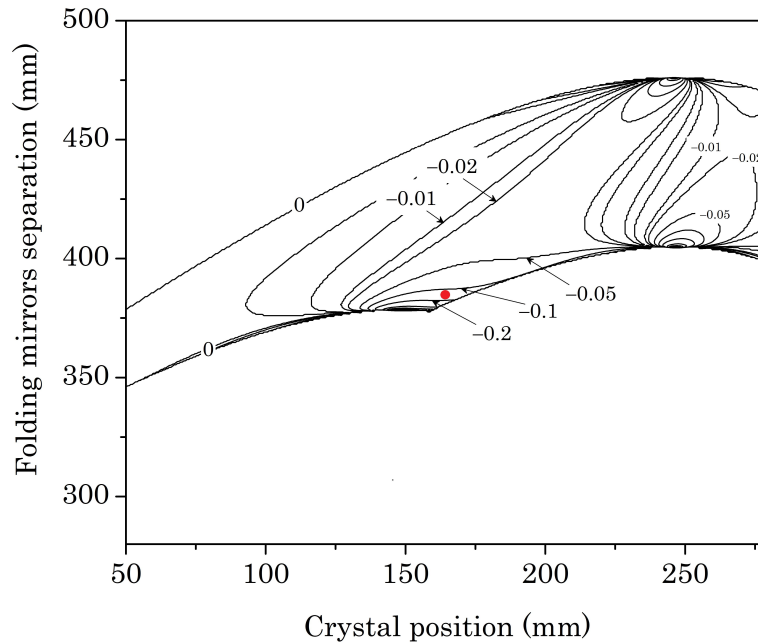


Figure 5.5. The Kerr sensitivity map. Contours show negative sensitivity values. The red spot shows the operating point of the mode-locked laser.

Considering the experimental results, the observed CW component in the spectrum of the KLM mode-locked laser has been previously reported. For example, in a KLM Yb:KYW laser the CW radiation could be eliminated by increasing the output coupling and therefore reducing the intra-cavity power [5]. Naumov et al. [12] described it as the excess energy radiation inside the resonator for a KLM Cr⁴⁺:YAG laser, which led to the saturation and reduction of self-amplitude modulation (SAM) at high intensities. The CW radiation could be suppressed by lowering the pump power (i.e. by reducing the saturation of SAM). On the other hand, the self-starting mode-locked operation (which requires a high SAM coefficient) was only feasible when the CW component was present. The same self-starting condition was also reported for a KLM Cr⁴⁺:YAG laser in [20]. In another experiments, the observed CW spikes in the KLM Cr⁴⁺:YAG [21] and Cr²⁺:ZnSe [22] lasers were attributed to the CW energy transfer to higher order transverse laser modes in the cavity. Furthermore, Machinet et al. [14] investigated the appearance of the CW component in the spectrum of a KLM Yb:CaF₂ laser when they measured the sensitivity of the mode-locked laser to the pump waist position in the crystal. The CW component appeared in the spectrum when the pump waist was moved longitudinally, which implied the important role of spatial overlap between the gain channel and the laser beam waist. In the mode-locked lasers using saturable absorbers, however, such a CW radiation could be suppressed by increasing the modulation depth of the absorber [23,24].

In our KLM laser, the CW radiation could not be eliminated solely by reducing the pump power or increasing the output coupler transmission. Some adjustment to the end mirror alignment was also required to suppress the CW component. We believe that two factors have contributed to this effect. First, by decreasing the pump power the possible saturation of SAM was reduced. At the same time, adjustment of the HR mirror alignment brought the laser mode into a position that had a more effective soft-aperturing effect. This is due to the fact that in case of the pump beam with poor beam quality factor ($M^2 \approx 40$) the soft-aperturing effect occurs within a short Rayleigh range of the pump beam. Therefore, precise positioning of the waists of the laser mode and pump beams was required. As a penalty, this could be achieved at the expense of the reduced output power. Similar to the self-starting KLM lasers in the previous works [12,20], the self-starting regime in our case was possible only with the CW spike present in the spectrum (see Table 5.1). It should be mentioned that since the laser cavity was designed for the soft-aperturing effect and large Kerr sensitivity in the crystal, adding a hard-aperture in the cavity did not help to eliminate the CW background or improve the Kerr-lens mode-locked operation.

In order to compare the results of this experiment to the previous reports on KLM lasers, it is worth considering the thermal properties of the laser crystal required for high power operation and the gain bandwidth required for support of ultrashort pulse generation. High power regime requires careful compensation of thermal lensing effect. Most of the Yb-doped crystals for which the KLM lasers were demonstrated have higher thermal conductivity coefficient than the Yb:KGW crystal, including Yb:YVO₄, Yb:CALGO, Yb:CaF₂, Yb:LSO and Yb:YAG crystals (see figure 5.6 (a)) [25–28]. Therefore, they are potential candidates for high power operation. The promising laser media for this regime are Yb:CaF₂ and Yb:CALGO crystals with thermal conductivity coefficients of 5.2 W/m/K and 6.9 W/m/K, respectively [26]. For instance, the generation of 68 fs with 2.3 W and 60 fs pulses and 2.73 W of output power in Yb:CaF₂ crystal have been reported (figure 5.6 (b)) [14,15]. In these works high brightness fiber lasers with high spatial beam quality ($M^2 \approx 1-2$) were used as the pump source. The optical-to-optical efficiency (~23-33%) of such mode-locked lasers was higher than our laser which indicated the important role of the spatial mode matching between the pump beam and the laser mode. However, when the overall efficiency is considered (i. e. including the pump source of the fiber laser system [40]), their efficiency reduces to a considerably lower value (~5-7%) than in our case. With a similar pumping system, a KLM Yb:CALGO laser delivered 40 fs pulses with 1.1 W of average output power [16]. Sub-

100 fs KLM lasers based on the Yb:YVO₄ and Yb:KYW crystals with the watt-level output power have been also reported using a tapered laser diode with a beam quality factor $M^2=3$ in [9]. These results indicate that using a custom-made pump source with high spatial beam quality was beneficial to generating multi-watt femtosecond pulses, but it increases the cost and complexity when compared to the standard commercially available multimode fiber-coupled laser diode in our system. On the other hand, considering the relatively smaller thermal conductivity coefficient of the Yb:KGW crystal when compared to, e.g., Yb:CALGO and Yb:CaF₂, our results demonstrated an outstanding performance in high power regime.

At the same time our results favorably compared with the previously demonstrated KLM Yb:KYW lasers (the crystal of Yb:KYW has similar properties to the Yb:KGW) that used single-mode fiber-coupled laser diodes as the pump [1–5]. For example, the KLM Yb:KYW laser delivered 204 fs pulses with 174 mW of output power at the repetition rate of 82 MHz in [2]. Therefore, our result represents more than one order of magnitude increase in average output power.

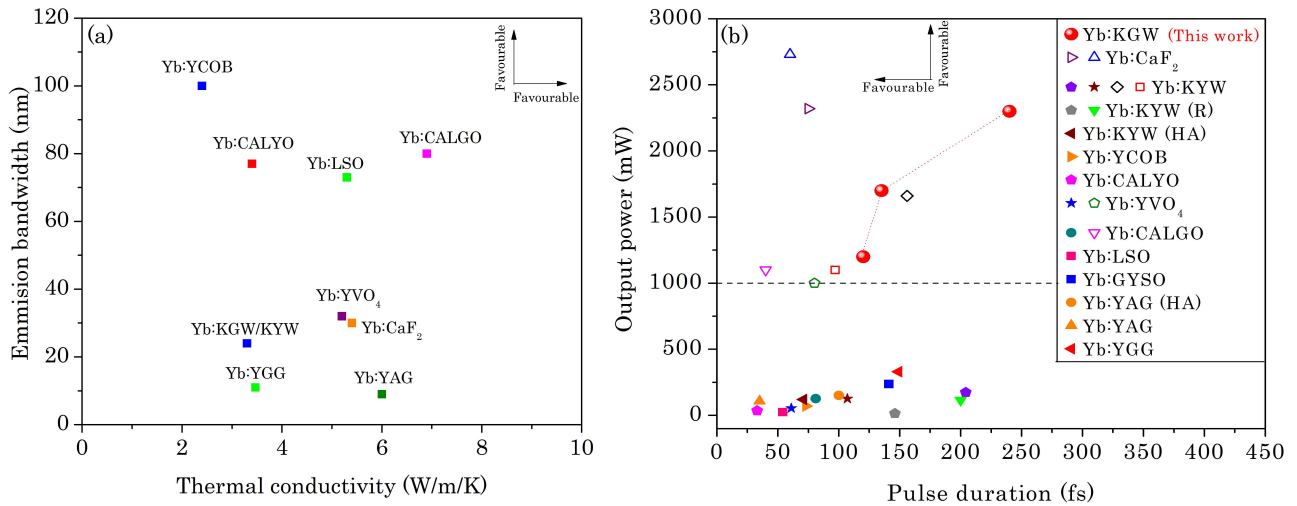


Figure 5.6. (a) Thermal conductivity and emission bandwidth of the Yb-doped crystals [7,25–30,35–38]. (b) Comparison of femtosecond Kerr-lens mode-locked lasers based on bulk Yb-ion doped crystals in terms of average output power and pulse duration. R: Ring cavity, HA: Hard-aperture mode-locked laser [1–9,14–16,29–34]. The hollow symbols show lasers excited with high beam quality ($M^2 \leq 3$) pump sources.

A summary of the KLM lasers with bulk Yb-ion doped crystals and a comparison between their thermal conductivity coefficients and emission bandwidths are compiled in figure 5.6. In the watt-level regime, none of the reported lasers (shown as hollow symbols in figure 5.6 (b)) used a multimode fiber-coupled laser diode as a pump source. Therefore, our results is the first report of a high power femtosecond KLM bulk Yb-ion doped laser using a simple multimode fiber-coupled pump diode module. It is believed that by using a shorter crystal with higher doping level coupled with an effective thermal management strategy it would be possible to enhance the laser operation in terms of output power. Another interesting direction would be to try mode locking regime with other laser polarizations [41,5,39] that have smoother emission spectra and can lead to the generation of shorter pulses or achieve this in dual-wavelength regime (chapter 3). Other broadband gain media such as Yb:CaF₂ [14,15], Yb:CALGO [16] or Yb:YVO₄ [9] can be also considered.

5.5. Conclusion

In summary, a high power pure Kerr-lens mode-locked operation of an Yb:KGW laser was demonstrated using a multimode fiber-coupled diode pump module. The laser delivered 240 fs pulses with 2.3 W of average output power at the repetition rate of 86.8 MHz, corresponding to 110 kW of peak power and 26 nJ of pulse energy. This is an order of magnitude higher output power than in previous reports with similar pump sources. The main limiting factor to the laser operation was the appearance of a strong CW component in the spectrum of the pulse. It was attributed to the saturation of SAM at high intracavity intensities and imperfect overlap between the laser mode and the pump beam in the crystal used for soft-aperturing KLM effect. This background CW radiation, however, could be suppressed by reducing the pump power and introducing some adjustment to the laser cavity alignment. The shortest generated pulse duration was 120 fs with 1.2 W of average output power. Self-starting operation of the laser was also realized and was accompanied by the CW component. In this case the laser delivered 120 fs pulses with 1.7 W. The demonstrated laser exhibits excellent performance using a cost-effective multimode fiber-coupled laser diode for laser pumping.

References

1. A. A. Lagatsky, C. T. A. Brown, and W. Sibbett, "Highly efficient and low threshold diode-pumped Kerr-lens mode-locked Yb:KYW laser," *Opt. Express* **12**, 3928 (2004).
2. P. Wasylczyk and C. Radzewicz, "Design and alignment criteria for a simple, robust, diode-pumped femtosecond Yb:KYW oscillator," *Laser Phys.* **19**, 129–133 (2009).
3. M. Endo, A. Ozawa, and Y. Kobayashi, "Kerr-lens mode-locked Yb:KYW laser at 4.6-GHz repetition rate," *Opt. Express* **20**, 12191 (2012).
4. P. Wasylczyk, P. Wnuk, and C. Radzewicz, "Passively modelocked, diode-pumped Yb:KYW femtosecond oscillator with 1 GHz repetition rate," *Opt. Express* **17**, 5630 (2009).
5. H. Liu, J. Nees, and G. Mourou, "Diode-pumped Kerr-lens mode-locked Yb:KY(WO₄)₂ laser," *Opt. Lett.* **26**, 1723 (2001).
6. Z. Gao, J. Zhu, J. Wang, Z. Wang, Z. Wei, X. Xu, L. Zheng, L. Su, and J. Xu, "Diode-pumped Kerr-lens mode-locked Yb:CaGdAlO₄ laser with tunable wavelength," *Laser Phys. Lett.* **13**, 15302 (2016).
7. Z. Gao, J. Zhu, J. Wang, Z. Wei, X. Xu, L. Zheng, L. Su, and J. Xu, "Generation of 33 fs pulses directly from a Kerr-lens mode-locked Yb:CaYAlO₄ laser," *Photonics Res.* **3**, 335 (2015).
8. A. A. Lagatsky, A. R. Sarmani, C. T. A. Brown, W. Sibbett, V. E. Kisel, A. G. Selivanov, I. A. Denisov, A. E. Troshin, K. V. Yumashev, N. V. Kuleshov, V. N. Matrosov, T. A. Matrosova, and M. I. Kupchenko, "Yb³⁺-doped YVO₄ crystal for efficient Kerr-lens mode locking in solid-state lasers," *Opt. Lett.* **30**, 3234 (2005).
9. F. M. Bain, A. A. Lagatsky, C. T. A. Brown, and W. Sibbett, "High-power Kerr-lens mode-locked ytterbium lasers," in *SPIE Proceedings* **6871**, p. 68712L (2008).
10. C. Chudoba, J. G. Fujimoto, E. P. Ippen, H. A. Haus, U. Morgner, F. X. Kärtner, V. Scheuer, G. Angelow, and T. Tschudi, "All-solid-state Cr:forsterite laser generating 14-fs pulses at 13 μm," *Opt. Lett.* **26**, 292 (2001).
11. M. N. Cizmeciyan, H. Cankaya, A. Kurt, and A. Sennaroglu, "Operation of femtosecond Kerr-lens mode-locked Cr:ZnSe lasers with different dispersion compensation methods," *Appl. Phys. B Lasers Opt.* **106**, 887–892 (2012).
12. S. Naumov, E. Sorokin, V. L. Kalashnikov, G. Tempea, and I. T. Sorokina, "Self-starting five optical cycle pulse generation in Cr⁴⁺:YAG laser," *Appl. Phys. B Lasers Opt.* **76**, 1–11 (2003).
13. L. Xu, G. Tempea, A. Poppe, M. Lenzner, C. Spielmann, F. Krausz, A. Stingl, and K. Ferencz, "High-power sub-10-fs Ti:sapphire oscillators," *Appl. Phys. B Lasers Opt.* **65**, 151–159 (1997).
14. G. Machinet, P. Sevillano, F. Guichard, R. Dubrasquet, P. Camy, J.-L. Doualan, R. Moncorgé, P. Georges, F. Druon, D. Descamps, and E. Cormier, "High-brightness fiber laser-pumped 68 fs–2.3 W Kerr-lens mode-locked Yb:CaF₂ oscillator," *Opt. Lett.* **38**, 4008 (2013).
15. P. Sevillano, G. Machinet, R. Dubrasquet, P. Camy, J.-L. Doualan, R. Moncorgé, P. Georges, F. P. Druon, D. Descamps, and E. Cormier, "Sub-50 fs, Kerr-lens mode-locked Yb:CaF₂ laser oscillator delivering up to 2.7 W," in *Advanced Solid-State Lasers Congress (OSA, 2013)*, p. AF3A.6.
16. P. Sevillano, P. Georges, F. Druon, D. Descamps, and E. Cormier, "32-fs Kerr-lens mode-locked Yb:CaGdAlO₄ oscillator optically pumped by a bright fiber laser," *Opt. Lett.* **39**,

- 6001 (2014).
17. H. Mirzaeian, S. Manjooran, and A. Major, "A simple technique for accurate characterization of thermal lens in solid state lasers," in *SPIE Proceedings* **9288**, pp. 928802–1 (2014).
 18. T. Waritanant and A. Major, "High efficiency passively mode-locked Nd:YVO₄ laser with direct in-band pumping at 914 nm," *Opt. Express* **24**, 12851 (2016).
 19. V. Magni, G. Cerullo, and S. De Silvestri, "Closed form gaussian beam analysis of resonators containing a Kerr medium for femtosecond lasers," *Opt. Commun.* **101**, 365–370 (1993).
 20. Y. P. Tong, A. V. Shestakov, B. H. T. Chai, J. M. Sutherland, P. M. W. French, and J. R. Taylor, "Self-starting Kerr-lens mode-locked femtosecond Cr⁴⁺:YAG and picosecond Pr³⁺:YLF solid-state lasers," *Opt. Lett.* **21**, 644 (1996).
 21. S. Akturk, M. Kimmel, R. Trebino, S. Naumov, E. Sorokin, and I. Sorokina, "Measuring several-cycle 1.5- μ m pulses using frequency-resolved optical gating," *Opt. Express* **11**, 3461 (2003).
 22. S. Vasilyev, M. Mirov, and V. Gapontsev, "Kerr-lens mode-locked femtosecond polycrystalline Cr²⁺:ZnS and Cr²⁺:ZnSe lasers," *Opt. Express* **22**, 5118 (2014).
 23. A. Agnesi, P. Dallochio, F. Pirzio, and G. Reali, "Compact sub-100-fs Nd:silicate laser," *Opt. Commun.* **282**, 2070–2073 (2009).
 24. C. Schriber, F. Emaury, A. Diebold, S. Link, M. Golling, K. Beil, C. Kränkel, C. J. Saraceno, T. Südmeyer, and U. Keller, "Dual-gain SESAM modelocked thin disk laser based on Yb:Lu₂O₃ and Yb:Sc₂O₃," *Opt. Express* **22**, 18979 (2014).
 25. W. Ryba-Romanowski, "YVO₄ crystals – puzzles and challenges," *Cryst. Res. Technol.* **38**, 225–236 (2003).
 26. J. Petit, P. Goldner, and B. Viana, "Laser emission with low quantum defect in Yb:CaGdAlO₄," *Opt. Lett.* **30**, 1345 (2005).
 27. M. Jacquemet, C. Jacquemet, N. Janel, F. Druon, F. Balembois, P. Georges, J. Petit, B. Viana, D. Vivien, and B. Ferrand, "Efficient laser action of Yb:LSO and Yb:YSO oxyorthosilicates crystals under high-power diode-pumping," *Appl. Phys. B* **80**, 171–176 (2005).
 28. H. Qiu, P. Yang, J. Dong, P. Deng, J. Xu, and W. Chen, "The influence of Yb concentration on laser crystal Yb:YAG," *Mater. Lett.* **55**, 1–7 (2002).
 29. Z. Gao, J. Zhu, W. Tian, J. Wang, Z. Zhang, Z. Wei, H. Yu, H. Zhang, and J. Wang, "Generation of 73 fs pulses from a diode pumped Kerr-lens mode-locked Yb:YCa₄O(BO₃)₃ laser," *Opt. Lett.* **39**, 5870 (2014).
 30. W.-L. Tian, Z.-H. Wang, J.-F. Zhu, Z.-Y. Wei, L.-H. Zheng, X.-D. Xu, and J. Xu, "Generation of 54 Fs Laser Pulses from a Diode Pumped Kerr-Lens Mode-Locked Yb:LSO Laser," *Chinese Phys. Lett.* **32**, 24206 (2015).
 31. J. Zhu, Z. Gao, W. Tian, J. Wang, Z. Wang, Z. Wei, L. Zheng, L. Su, and J. Xu, "Kerr-Lens Mode-Locked Femtosecond Yb:GdYSiO₅ Laser Directly Pumped by a Laser Diode," *Appl. Sci.* **5**, 817–824 (2015).
 32. S. Uemura and K. Torizuka, "Kerr-Lens Mode-Locked Diode-Pumped Yb:YAG Laser with the Transverse Mode Passively Stabilized," *Appl. Phys. Express* **1**, 12007 (2008).
 33. S. Uemura and K. Torizuka, "Sub-40-fs Pulses from a Diode-Pumped Kerr-Lens Mode-Locked Yb-Doped Yttrium Aluminum Garnet Laser," *Jpn. J. Appl. Phys.* **50**, 10201 (2011).
 34. J. Zhang, H. Han, W. Tian, L. Lv, Q. Wang, and Z. Wei, "Diode-pumped 88-fs Kerr-lens

- mode-locked Yb:Y₃Ga₅O₁₂ crystal laser," *Opt. Express* **21**, 29867 (2013).
35. F. Druon, F. Balembois, and P. Georges, "New laser crystals for the generation of ultrashort pulses," *Comptes Rendus Phys.* **8**, 153–164 (2007).
 36. S. Chénais, F. Druon, S. Forget, F. Balembois, and P. Georges, "On thermal effects in solid-state lasers: The case of ytterbium-doped materials," *Prog. Quantum Electron.* **30**, 89–153 (2006).
 37. L. Shah, Q. Ye, J. . Eichenholz, D. . Hammons, M. Richardson, B. H. . Chai, and R. . Peale, "Laser tunability in Yb³⁺:YCa₄O(BO₃)₃ {Yb:YCOB}," *Opt. Commun.* **167**, 149–153 (1999).
 38. H. Yu, K. Wu, B. Yao, H. Zhang, Z. Wang, J. Wang, Y. Zhang, Z. Wei, Z. Zhang, X. Zhang, and M. Jiang, "Growth and Characteristics of Yb-doped Y₃Ga₅O₁₂ Laser Crystal," *IEEE J. Quantum Electron.* **46**, 1689–1695 (2010).
 39. A. Major, D. Sandkuijl, and V. Barzda, "A diode-pumped continuous-wave Yb:KGW laser with N_g-axis polarized output," *Laser Phys. Lett.* **6**, 779–781 (2009).
 40. J. Boulet, Y. Zaouter, R. Desmarchelier, M. Cazaux, F. Salin, J. Saby, R. Bello-Doua, and E. Cormier, "High power ytterbium-doped rod-type three-level photonic crystal fiber laser," *Opt. Express* **16**, 17891–17902 (2008).
 41. G. R. Holtom, "Mode-locked Yb:KGW laser longitudinally pumped by polarization-coupled diode bars," *Opt. Lett.* **31**, 2719 (2006).

Chapter 6

Simulation of an optical parametric oscillator (OPO) based on the BIBO, BBO and LBO crystals pumped by a frequency-doubled mode-locked Yb:KGW laser

6.1. Introduction

In this chapter, the results of numerical investigation of the phase-matching properties of the BIBO, BBO and LBO crystals for femtosecond optical parametric oscillators (OPO) are presented. An OPO laser source generates wavelength-tunable laser radiation (i.e., signal and idler waves) from an input laser (pump) and is based on parametric generation in a nonlinear optical crystal. The main goal of this numerical work was to investigate the performance of an OPO as an extension of the demonstrated high power mode-locked lasers in previous chapters as a future work. First, an introduction to an OPO oscillator and the nonlinear crystals that are used for frequency conversion is provided. The previous works on OPOs are also reviewed. Then the optical properties of the BIBO, BBO and LBO crystals as the chosen nonlinear media are reviewed. The phase-matching properties of these crystals for an OPO with wavelength tuning in the visible and near infrared spectral ranges were numerically investigated and the results were discussed. In addition, dispersive characteristics, including the group velocity mismatch and group velocity dispersion, which are of significant importance in femtosecond OPOs, were calculated and discussed. Finally, the attainable gain bandwidths for each crystal were estimated. The results of this work can be considered as the future application of the demonstrated high power femtosecond mode-locked lasers in the previous chapters.

6.2. Optical parametric oscillator and nonlinear crystals

An OPO is a widely-tunable wavelength laser source based on parametric oscillation and consists of a nonlinear crystal with high second-order nonlinearity, i. e. $\chi^{(2)}$ (Appendix E) placed in a resonator which is excited by the pump laser (figure 6.1). The typical capability of wavelength tunability of the OPOs is much higher than that of conventional lasers. Ultra-short pulses with high peak power from a mode-locked laser and with a central wavelength in the near-infrared region can be frequency doubled by a second harmonic generation crystal and be used as the pump for the OPO crystal.

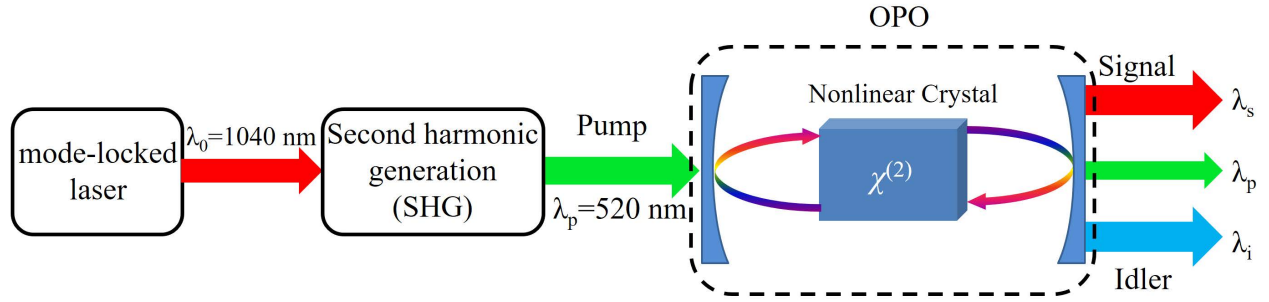


Figure 6.1. Optical parametric oscillator pumped by a frequency-doubled mode-locked laser.

Optical parametric oscillation is based on the induced nonlinear polarization ($P_n \propto \epsilon_0 \chi^{(2)} E^2$) by a high power input laser (i.e., pump) wave. As a result parametric waves (i.e., signal and idler) at different wavelengths can be generated with efficient energy coupling between the pump and these waves if the phase-matching condition is satisfied,

$$\omega_p = \omega_s + \omega_i$$

$$\vec{k}_p = \vec{k}_s + \vec{k}_i \quad \text{Eq.6.1}$$

where \vec{k} is the wave vector and $|\vec{k}| = \frac{\omega n}{c}$, n is the refractive index, c is the speed of light in vacuum, ω is the angular frequency of the wave, and p, s, i stand for pump, signal and idler, respectively. Since the wave vectors are functions of the refractive indices along the propagation path of each wave, a nonlinear crystal with the defined principal axes of refractive index can be used in a particular geometry for generating specific wavelengths (see Appendix E).

Ultra-short pulse optical parametric oscillators (OPO) have found numerous applications due to their capability to generate broadly tunable radiation with relatively high peak power. In fact, OPOs based on the second-order nonlinearity in crystals can considerably expand the range of the attainable wavelengths as well as being able to produce ultrafast pulses owing to the instantaneous nature of the nonlinear gain. Such a versatile tunable laser can be used in coherent anti-Stokes Raman scattering (CARS) microscopy and spectroscopy [1], time-resolved spectroscopy [2] and stimulated emission microscopy [3]. In particular, picosecond synchronously green-pumped OPOs are of importance in CARS microscopy because the spectral width of the laser source matches the intrinsic linewidth of molecular vibrational frequencies, and they can provide wavelengths in the near-infrared region [4–6].

In general, femtosecond OPOs are pumped by the Ti:sapphire lasers at 800 nm, which are in turn excited by the other green laser sources such as argon-ion laser or harmonics of the Nd:YAG or Nd:YVO₄ lasers [7,8]. These pumping schemes increase the complexity and cost of an OPO system. However, developments in Yb-doped materials have allowed the generation of femtosecond laser pulses with multi-watt output powers which can be directly pumped by inexpensive InGaAs diode lasers [9–13]. Using a pump source in the visible range, for instance, a frequency-doubled femtosecond Yb-doped laser at 520 nm, allows us to exploit the wavelength range of the OPOs more effectively, and the generated signal and idler wavelengths can cover the visible and near-infrared ranges, respectively. The tunability and optical characteristics of the OPOs are principally defined by the nonlinear crystals in a resonant cavity. Amongst the wide variety of the nonlinear crystals, β -barium borate (BaB₂O₄) and lithium triborate (LiB₃O₅) are well-known materials that are extensively used in OPOs [14–18].

β -Barium borate (BBO) is a non-centrosymmetric negative uniaxial crystal possessing the point group symmetry 3m [19]. As a result of its small absorption, large temperature phase-matching bandwidth and high damage threshold, BBO is a suitable candidate for frequency conversion at high peak powers [19]. Furthermore, BBO exhibits a large transparency range over the ultraviolet and visible wavelengths, e.g. 190–3500 nm [20–22]. The BBO-OPOs have been established as excellent sources of radiation with broad and continuous tuning range with high output powers [14,23–26]. The performance of the BBO-OPOs has been investigated in a number

of experiments employing nanosecond [15], picosecond [21,27] and femtosecond [28] pump pulses.

The other classic crystal is lithium triborate (LBO), which is a biaxial crystal of group point symmetry $mm2$ and exhibits a wide transparency range (160–2600 nm), moderate nonlinear coefficient, high optical damage threshold, and the possibility of temperature tuning with noncritical phase-matching [29]. The last feature is favorable because of a considerable increase in the angular acceptance and elimination of the spatial beam walk-off. The maximum nonlinearity ($d_{\text{eff}} = 1.02 \text{ pm V}^{-1}$) is expected when the type I noncritical phase-matching is maintained [30,31]. Due to the high temperature sensitivity of LBO, temperature tuning for noncritical phase-matching is preferred since no further re-alignment of the laser cavity is necessary. Compared to the BBO with higher nonlinear coefficient, LBO exhibits a higher damage threshold, smaller walk-off angle and larger angular bandwidth [32]. The performance of the LBO-OPOs has been demonstrated using nanosecond [33], picosecond [17] and femtosecond [1] pump pulses. As an example, Cleff et al. reported the operation of a temperature-tuned LBO-OPO pumped by a frequency doubled mode-locked Yb-fiber laser at 1050 nm. The tuning range of a signal wave in the 780–940 nm range was obtained by changing the temperature of the crystal from 132 to 170° C [1].

Recent developments in nonlinear optical materials have introduced a crystal of bismuth triborate (BiB_3O_6 , BIBO) with attractive features. As a biaxial crystal, BIBO exhibits a broad transmission range (286–2600 nm), large angular and spectral acceptance bandwidths, low walk-off and a considerable wavelength tuning range [34]. It exhibits an effective nonlinear coefficient of about 3.7 pm V^{-1} , which is larger than that of LBO and BBO, and is comparable to KTP [35,36]. The versatile phase-matching and high efficiency of BIBO for both frequency-up and frequency-down conversion of ultrafast pulses from the UV to the IR region have been demonstrated in experimental results, including efficient second harmonic generation (SHG) using continuous-wave, picosecond and femtosecond lasers [37–39], third harmonic generation [40], and optical parametric generation and amplification with green and IR pumps [41,42]. The BIBO-OPOs have been also investigated, including the OPOs pumped by femtosecond lasers in the blue and IR [43,44] and pumped by a green nanosecond laser [45]. For instance, Peltz et al. performed an experiment in which the BIBO-OPO was pumped by the second harmonic of a Q-switched Nd:YVO₄ laser, generating 5.8 ns duration pulses at a repetition rate of 10 kHz at 532 nm. Through

the angle tuning scheme in the YZ plane, the signal was tuned from 735.6 nm at $\varphi=0^\circ$ to 970 nm at $\varphi=11.7^\circ$, and the corresponding idler was tuned from 1930 to 1180 nm [45]. Therefore, a BIBO crystal is an attractive candidate for femtosecond OPOs with green pumps provided by the second harmonic of ultrafast Yb-doped lasers.

Optical parametric generation is also possible in periodically poled materials such as PPKTP, PPcLN and PPSLT based on a quasi-phase-matching scheme (QPM) [46–49]. The engineered structure of these crystals makes it feasible to employ the largest nonlinearity element of a crystal, as well as eliminating the Poynting vector walk-off since the interacting waves have the same polarizations ($e+e\rightarrow e$). For instance, PPcLN exhibits an effective nonlinearity on the order of 17 pm V^{-1} , but it suffers from the photorefractive damage and a high coercive field which severely limits the achievable output power level and length of the crystal, respectively. On the other hand, the PPKTP and PPSLT crystals offer lower coercive fields, albeit at the expense of lower nonlinearity. These two crystals also exhibit a higher photorefractive damage threshold and should be more suitable for high-power applications. The phase-matching condition is attained through temperature tuning and was studied in detail in [46,48,49]. In contrast, BIBO, BBO and LBO do not suffer from photorefractive damage and can be used in high-power OPOs.

6.3. Optical properties

The linear refractive index of a material as a function of wavelength (or frequency) is an important optical property since it affects the speed of frequency components of an electrical field in the material and can disperse an optical pulse. The Sellmeier's equation defines the refractive index as a function of wavelength for the material of interest (Appendix C). We have examined the best sets of Sellmeier's coefficients for the linear refractive indices of the nonlinear crystals in question. For BBO, the wavelength-dependent Sellmeier's equations from [22,50–52] were evaluated and compared to the experimental results from [15,32,51,53–55]. The most complying sets of coefficients were presented by [51], which were the altered version from [50] for long wavelengths (deep infrared region). For LBO, the Sellmeier's coefficients from [56–60] were chosen and evaluated in comparison to the experimental results of [18,57,61] for angle-tuned phase-matching and the results of [4,62–64] for temperature-tuned phase-matching schemes. The coefficients provided by [57] were found to be the most compatible with the experimental results

of the temperature-tuned wavelength curves. However, there are no significant differences from angle-tuned results. For BIBO, the coefficients from [40,65–67] were evaluated and compared to [41,43,68] for angle-tuned phase-matching, and to [41,69] for temperature tuning. The most accurate sets were found from [67] for the temperature-tuned curves and for the angle-tuned curves at long wavelengths. The variation of the refractive indices and the group velocities (i.e. velocity of the pulse envelope) as functions of wavelength in a tuning range of these crystals are depicted in figure 6.2.

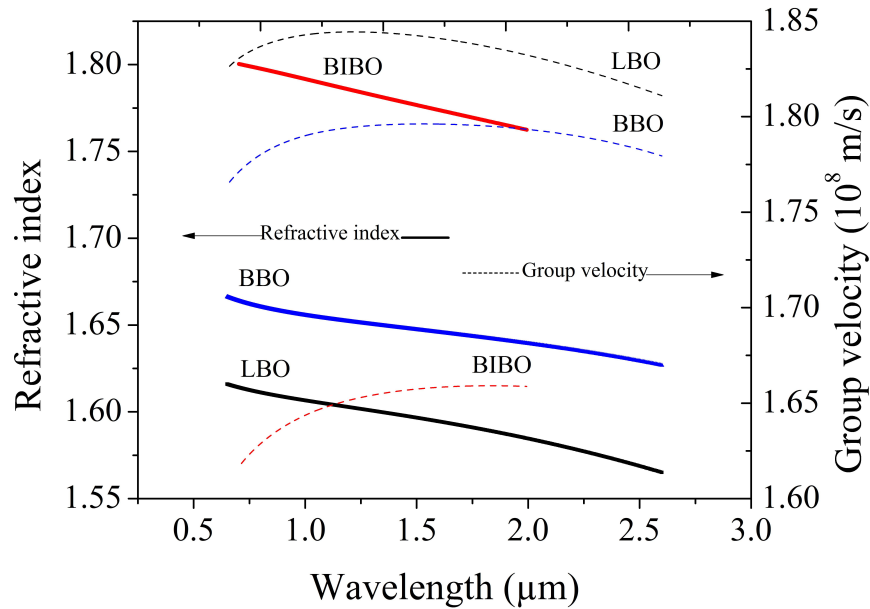


Figure 6.2. The refractive index profiles and the group velocities versus the wavelength at room temperature.

6.4. Phase-matching properties

The phase-matching properties of each nonlinear crystal are a function of crystal structure, wavelength, polarization states of the interacting waves, temperature and orientation of the crystal. There are two principal conditions described by Eq. 6.1 that must be satisfied simultaneously by propagating waves in order to have phase-matched interaction: the energy conservation condition ($\omega_3 = \omega_2 + \omega_1$), and the momentum conservation condition ($k_3 = k_2 + k_1$), where $\omega_{j=1,2,3}$ and $k_{j=1,2,3}$ are the frequencies and wave vectors of the pump, signal and idler, respectively. On the other hand, a suitable type of wavelength tuning method for an OPO, temperature- or angle-based, is dependent on the required range of wavelengths, and the angular and temperature sensitivities of the chosen

crystal. However, in case of an acceptable temperature sensitivity and tuning response, temperature tuning is a favorable method owing to the fact that no further re-alignment of an OPO cavity is needed. The crystal's orientation, propagation direction and polarization states of the interacting waves also determine the maximum achievable effective nonlinearity, maximum conversion efficiency, as well as the unfavorable parameters such as walk-off angle. In this section, we have investigated the collinear phase-matching conditions and wavelength tuning range of crystals based on the aforementioned contributing factors for an OPO pumped by a femtosecond Yb-ion-based laser at 520 nm. The main features of the investigated crystals are represented in table 6.1.

Table 6.1. Optical properties of BBO, BIBO and LBO crystals.

	BBO	BIBO	LBO
Point group	3m	2	mm2
Transparency range (nm)	190-3500 [20–22]	286-2600 [34]	160-2600 [29]
Sellmeier's coefficients	[51]	[67]	[57]
Nonlinearity coefficients (pm V ⁻¹)	$d_{22}=2.3$ $d_{31}=-0.16$ [70]	$d_{12}=3.2$, $d_{13}=-1.76$ $d_{14}=1.66$ [34]	$d_{31}=-0.95$, $d_{32}=1.02$, $d_{33}=0.057$ [31]
Effective phase-matching configuration	Type I ($o+o\rightarrow e$) Angle tuning	Type I ($e+e\rightarrow o$) Angle tuning YZ plane	Type I ($e+e\rightarrow o$) Noncritical phase-matching
Effective nonlinearity	$d_{\text{eff}}=d_{31}\sin(\theta)-$ $d_{22}\cos(\theta)\sin(3\varphi)$	$d_{\text{eff}}=-d_{12}\cos(\theta)^2-$ $d_{13}\sin(\theta)^2+d_{14}\sin(2\theta)$	$d_{\text{eff}}=1.02$ pm V ⁻¹
Thermo-optic coefficients	–	[67]	[57]

The best performance of a BBO crystal is realized through a type I ($o+o\rightarrow e$) angle-tuned interaction owing to its largest effective second-order nonlinearity (see table 6.1). The pump is assumed to be polarized in the extraordinary plane, and the phase-matched signal and idler would be in the ordinary plane. The calculated wavelength tuning range is shown in figure 6.3 (a). It can be readily seen that the signal wavelength can be tuned smoothly from about 650 nm at the blue side to the degeneracy at 1040 nm, while the corresponding idler is tuned from 1040 nm steeply to the infrared region by an azimuthal angle change from 23.2° to 21°, accordingly. The degeneracy happens at around 23.2°, so the pertinent angle tuning range would be limited only to 2.2°. The type II interaction with a smaller nonlinear coefficient, acceptable conversion efficiency but narrower wavelength tuning range has been also previously investigated [71–73].

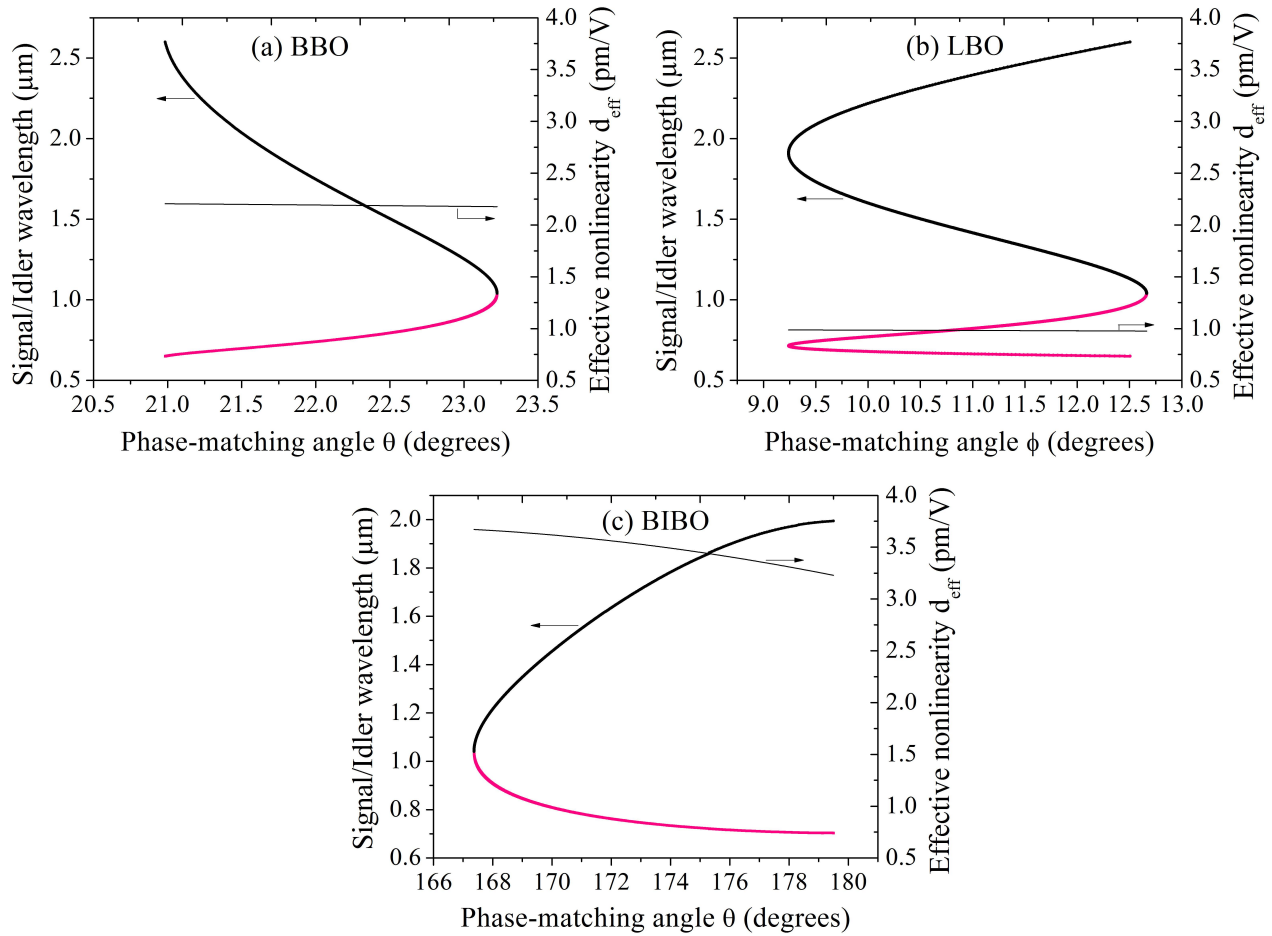


Figure 6.3. Angle tuning curves in BBO (a), LBO (b) and BIBO (c) crystals at room temperature with an effective nonlinearity coefficient d_{eff} . Idler — black curve, signal — red.

The angle tuning scheme can also be applied in LBO. The most suitable phase-matching would be type I interaction in the principal XY plane, utilizing the maximum effective nonlinearity. For azimuthal angle change from 12.5° to about 9.2° , the signal wavelength covers 650 nm to 1040 nm, and the idler is tuned from 1040 nm to the infrared region, namely $2.5 \mu\text{m}$ at 11.7° . The applicable angle tuning range would be limited to about 3° , as can be seen from figure 6.3 (b).

For BIBO, the angle-based wavelength tuning is favorable through type I phase-matching in the principal YZ plane, where the maximum d_{eff} is achievable. The maximum effective nonlinearity is experienced if the azimuthal angle is changed near the Z axis. As shown in figure 6.3 (c), the signal wavelength is tunable gently from 700 to 1040 nm and the idler wavelength changes from 1040 nm to $2 \mu\text{m}$. The feasible range of angle tuning in this case is about 12.6° ,

roughly five times that in BBO. The calculations clearly show that compared to BIBO, BBO gives a considerably greater phase-matched wavelength tuning range, especially at the red side, but it is much more sensitive to angular changes owing to the limited range of tuning angles.

On the other hand, temperature tuning is of interest due to the fact that no re-alignment is necessary in the cavity, and it can be applied to BIBO and LBO, while BBO does not significantly respond to temperature changes. Assuming a collinear, non-critical phase-matching, i.e. $\varphi=0^\circ$ and $\theta=90^\circ$, calculations show that an LBO-OPO pumped at 520 nm allows continuous wavelength tuning range from 650 nm to 1040 nm for signal and from 2600 nm to 1040 nm for the idler wavelength when the temperature is changed from 168° C down to 116° C (figure 6.4a). The temperature tuned BIBO-OPO, however, does not exhibit considerable wavelength tuning range, as can be seen in figure 6.4.

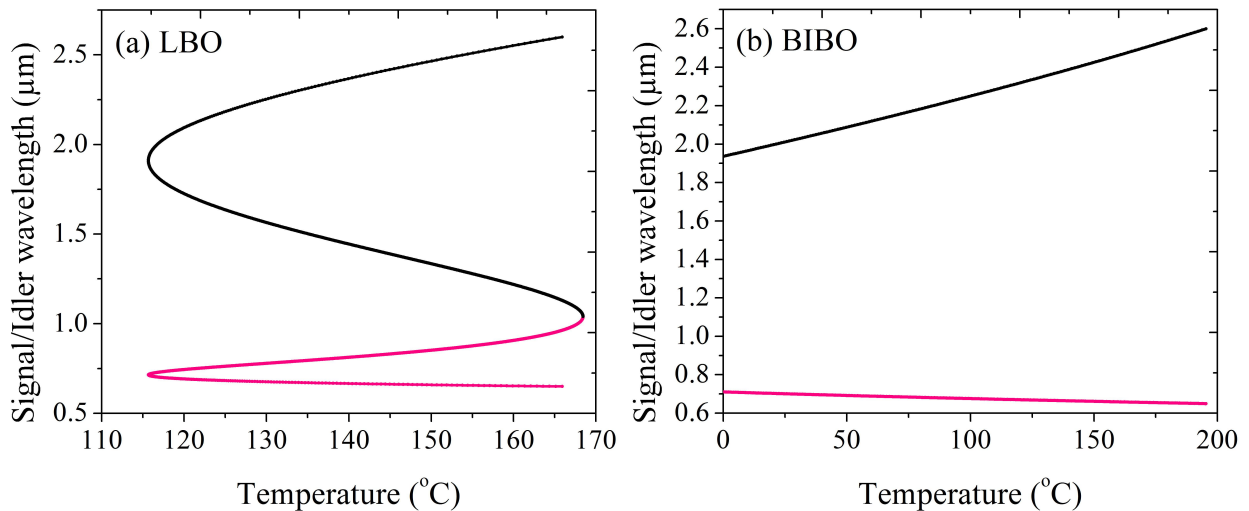


Figure 6.4. Temperature tuning curves in LBO (a) and BIBO (b) crystals with corresponding effective nonlinearity coefficients d_{eff} . Idler—black curve, signal—red.

Another important parameter which sets limitations on the effective nonlinear length is the angular walk-off (spatial walk-off), which is primarily determined by the angle of light propagation, as well as by the refractive index profiles at the corresponding wavelengths [74]. For the phase-matching schemes for BIBO and BBO, the angular walk-offs at room temperature are predicted in figure 6.5. Since the walk-off angle is zero in the vicinity of the principal axes, in BIBO the spatial walk-off increases from zero to a maximum value of around 29 mrad, while BBO maintains a relatively constant walk-off angle (52–55 mrad) due to a considerably more limited

range of angle tuning. It can be readily seen that the maximum angular walk-off in BBO is roughly two times the maximum value in BIBO. In contrast, in temperature-tuned LBO the effect of angular walk-off is absent due to non-critical phase-matching condition.

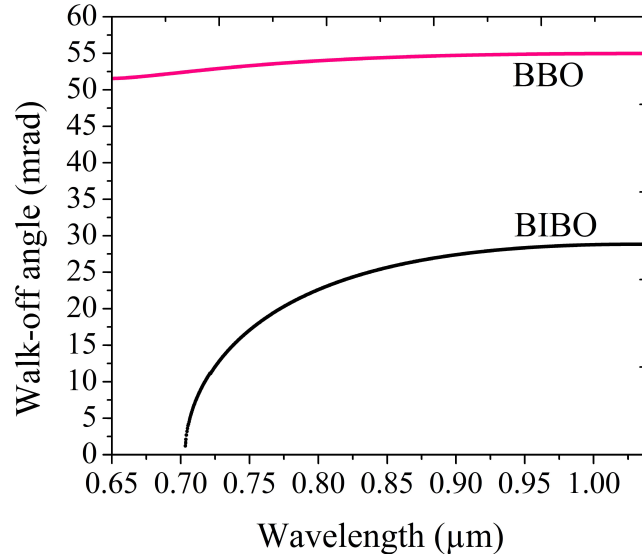


Figure 6.5. Angular walk-off versus wavelength in BBO and BIBO crystals.

The comparison of borate-based crystals, i.e. BIBO and BBO, is of importance in terms of OPO performance in the UV and visible ranges. In addition to the higher effective nonlinearity of BIBO, it exhibits a superior angular acceptance and a lower spatial walk-off angle. Although the inferior nonlinearity of BBO could be compensated by using a longer crystal, BIBO is advantageous for its favorable characteristics in the femtosecond interaction regime when the length of a crystal is restricted due to the group velocity mismatch (GVM). On the other hand, BBO and LBO are preferable for deep UV performance owing to their wider transparency in the UV range. However, the lower nonlinearity of these crystals limits their use mainly for applications that involve high pulse energy.

6.5. Dispersive properties

Dispersive properties of the nonlinear crystals are of particular importance in the femtosecond pumping regime due to their effects on the effective interaction length of the pump pulses, the pulse width, and the conversion efficiency. Temporal pulse broadening by GVD (group velocity dispersion) and temporal walk-off by GVM (group velocity mismatch) impose limits on

the applicable crystal length. Practically, in order to restrict the signal pulse broadening to around 10%, the maximum temporal dispersion, defined by $\Delta t = L(v_p^{-1} - v_s^{-1})$, should be smaller than half of the initial pump pulse width [75,76]. Here, L is the crystal length, v_p is the group velocity of the pump wave and v_s is the group velocity of the signal wave.

The group velocity mismatch values between the pump, signal and idler for BIBO and BBO are depicted in figures 6.6 (a) and (b), respectively. For type I phase-matching with 520 nm pump, BIBO exhibits about two times higher GVM between the pump and generated wavelengths than BBO over its wavelength tuning range and more than three times higher than LBO. The difference between the GVM_{PS} (pump and signal) and GVM_{PI} (pump and idler) becomes substantial (~ 150 fs mm^{-1}) far from degeneracy (~ 700 nm) in the case of BIBO, whereas it approaches 17 fs mm^{-1} at around 650 nm in BBO. In addition, the GVM between the signal and idler is always lower in BBO when compared to BIBO over the most of the wavelength tuning range, implying a smaller spectral acceptance bandwidth for BIBO, which is approximately defined as $\nabla v_1 = \nabla v_2 = 0.886/(L|GVM_{si}|)$ [77].

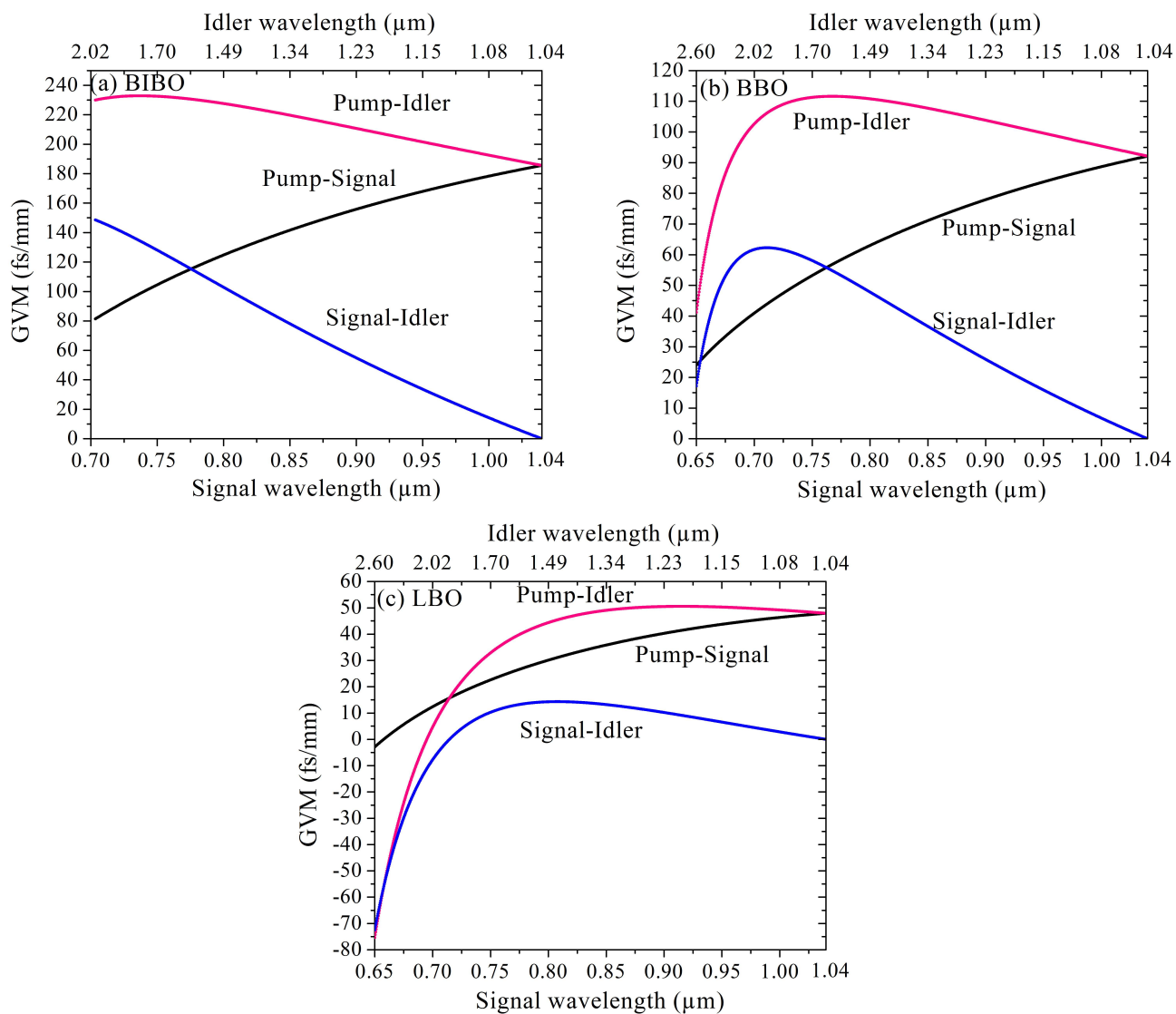


Figure 6.6. Group velocity mismatch between the pump, signal and idler in BIBO (a), BBO (b), and LBO (c) crystals.

Thus, a shorter crystal of BIBO should be used in the femtosecond regime, which can compromise the overall conversion efficiency. The group velocity mismatch values in LBO for the type I phase-matching scheme are shown in figure 6.6 (c). Exhibiting similar trends to BBO crystal, LBO maintains smaller values of GVM between the pump and generated wavelengths. The GVM_{SI} reaches its maximum of 14.3 fs mm^{-1} at 800 nm in LBO, while it is almost 62 fs mm^{-1} at around 700 nm in BBO. In the case of LBO, there are two points (710 and 1040 nm) at which the group velocities of signal–idler with respect to the pump are the same.

Group velocity dispersion is also calculated for these crystals, shown in figure 6.7. The signal wave experiences the lowest GDD over the wavelength tuning range in LBO. Since GDD for the signals in all crystals has positive values, the zero GDD points are located at 1580 nm in BIBO, 1490 nm in BBO, and 1190 nm in LBO in the idler wavelength region. The idlers in LBO and BIBO, on the other hand, experience substantially higher (negative) GDD values than signals.

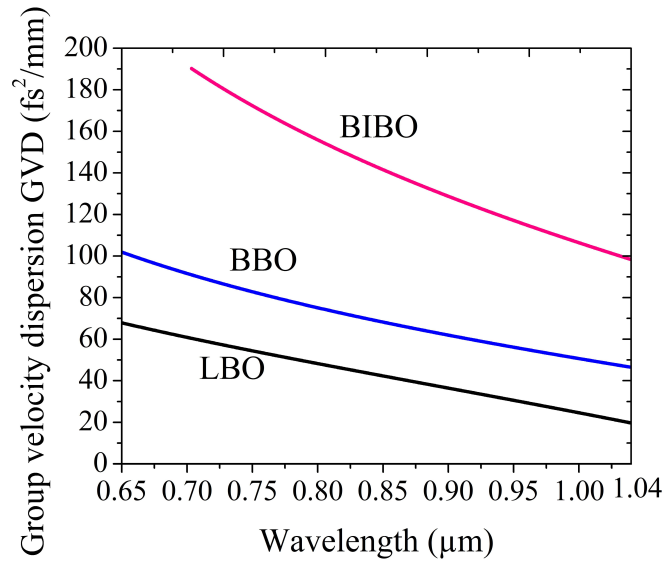


Figure 6.7. Group velocity dispersion vs. signal wavelength.

6.6. Spectral properties

The spectral gain bandwidth is of importance because it defines the minimum achievable pulse duration. Under the assumptions of plane-wave approximation, the absence of pump depletion, steady-state gain approximation and the pump chromaticity, the analytical expression for the spectral bandwidth could be estimated by expansion of the wave-vector mismatch Δk . The parametric single-pass gain for the case of a large gain can be expressed as [34]

$$G = \frac{1}{4} \exp(2L\sqrt{\Gamma^2 - (\Delta k/2)^2}), \quad \text{Eq. 6.2}$$

where $\Gamma^2 = \frac{8\pi^2 d_{\text{eff}}^2 I_p}{n_p n_s n_i \lambda_s \lambda_i \epsilon_0 c}$ ($\Gamma L \gg 1$), n_j is the refractive index, λ_j is the wavelength, L is the length of crystal and I_p is the pump intensity. The wave vector mismatch in terms of signal frequency can then be expressed as

$$\Delta k = \Delta k_0 + \left(\frac{\partial k_S}{\partial \omega_s} - \frac{\partial k_I}{\partial \omega_s} \right) \Delta \omega_s + \frac{1}{2!} \left(\frac{\partial^2 k_S}{\partial \omega_s^2} + \frac{\partial^2 k_I}{\partial \omega_s^2} \right) (\Delta \omega_s)^2 + \dots \quad \text{Eq. 6.3}$$

The gain bandwidth is defined by the amount of Δk for which the gain drops to half of its maximum value, which can be expressed as $\Delta k_{FWHM} \approx \pm 2(\ln 2)^{1/2} (\Gamma/L)^{1/2}$. In case of a phase-matched process $\Delta k_0=0$ and the higher orders of derivatives, usually the second order, should be included near the degeneracy where the first term of the expansion approaches zero.

The gain bandwidths for 1 mm long crystals with a pump intensity of 5 GW cm⁻² are depicted in figure 6.8. The first-order approximations of bandwidth exhibit rapid increases and discontinuities around signal–idler degenerate wavelengths in all crystals (at 1040 nm) and around two-signal degenerate wavelengths in LBO and BBO. The second-order bandwidth approximations are also calculated near the signal–idler degeneracy. As can be seen, LBO exhibits the widest and BIBO the narrowest gain bandwidth over the entire wavelength tuning range. Similar calculations showed that exploiting other types of phase-matching in different principal planes in BIBO do not offer wider bandwidth for the pump wavelength of 520 nm. Nevertheless, it can be significantly improved if a shorter crystal is selected. In this case, the effect of a larger GVM in BIBO can be also reduced. For instance, a 0.5 mm BIBO crystal provides a bandwidth of around 18.2 THz at 900 nm for the same pumping scheme, compared to 12.8 THz at the 900 nm in BIBO with the crystal length of 1 mm.

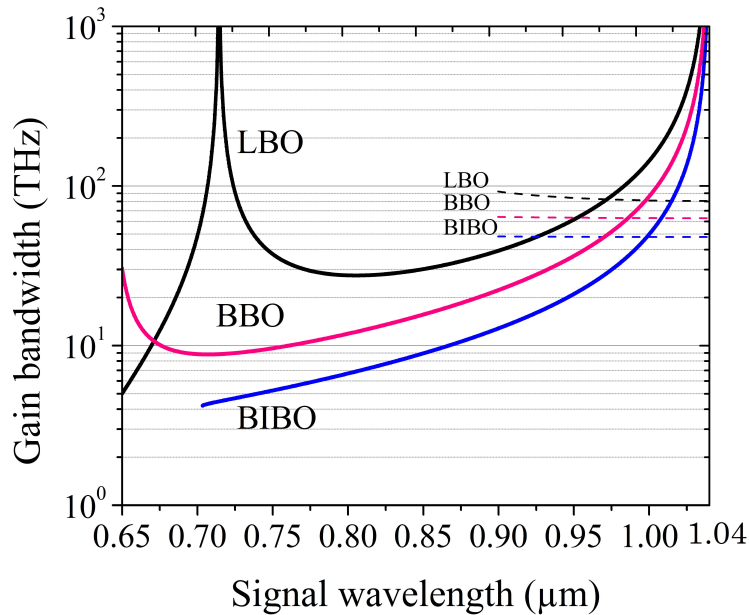


Figure 6.8. The gain bandwidth versus the signal wavelength for LBO, BBO and BIBO crystals. The solid lines show the first derivative of the bandwidth approximation and the dashed lines show the second derivative around the degeneracy.

6.7. Conclusion

In this Chapter the phase-matching properties of BBO, BIBO and LBO crystals at a pump wavelength of 520 nm (which can be generated by the frequency-doubled Yb-doped lasers) were investigated. The BBO and LBO have been well established as nonlinear crystals with a moderate effective nonlinearity compared to the recently developed BIBO with substantially higher nonlinearity. The calculations were performed by considering the geometries of each crystal that yielded the highest effective nonlinearity. Comparing the angle tuning versatility of BBO and BIBO, BIBO offers a greater angular tuning range and as a result smoother wavelength tuning with smaller spatial walk-off. On the other hand, temperature tuning in LBO is preferable in order to avoid OPO cavity re-alignment, and the wavelength tuning properties of LBO are shown to be very favorable.

Calculation of GVM values over the wavelength tuning range of crystals showed that the signal and idler in LBO experience the least amount of group velocity mismatch and BBO is

preferable to BIBO over the whole tuning range. The GVM is a crucial parameter in femtosecond OPOs, and in this case, LBO is the best choice. On the other hand, the shorter length of BIBO crystal could be chosen to minimize the effect of GVM while taking advantage of its superior nonlinearity.

The gain bandwidth is another prominent factor in ultrafast OPOs. It was shown that LBO and BBO crystals offer broader gain bandwidths over the whole considered wavelength tuning range than BIBO. However, for spectroscopic investigation where narrow bandwidth is desirable, highly nonlinear BIBO would be preferred.

In summary, the results of this work indicate the basic properties and highlight the potential of the LBO, BBO, and BIBO crystals for use in femtosecond OPOs with a green pump at 520 nm. The results of this work can be considered as the future application of the demonstrated mode-locked lasers in the previous chapters.

References

1. C. Cleff, J. Epping, P. Gross, and C. Fallnich, "Femtosecond OPO based on LBO pumped by a frequency-doubled Yb-fiber laser-amplifier system for CARS spectroscopy," *Appl. Phys. B* **103**, 795–800 (2011).
2. T. F. Albrecht, J. H. H. Sandmann, J. Feldmann, W. Stolz, E. O. Göbel, H. Hillmer, R. Lösch, and W. Schlapp, "Design and application of a femtosecond optical parametric oscillator for time-resolved spectroscopy of semiconductor heterostructures," *Appl. Phys. B* **60**, 459–467 (1995).
3. W. Min, S. Lu, S. Chong, R. Roy, G. R. Holtom, and X. S. Xie, "Imaging chromophores with undetectable fluorescence by stimulated emission microscopy," *Nature* **461**, 1105–1109 (2009).
4. M. Jurna, J. P. Korterik, H. L. Offerhaus, and C. Otto, "Noncritical phase-matched lithium triborate optical parametric oscillator for high resolution coherent anti-Stokes Raman scattering spectroscopy and microscopy," *Appl. Phys. Lett.* **89**, (2006).
5. K. Kieu, B. G. Saar, G. R. Holtom, X. S. Xie, and F. W. Wise, "High-power picosecond fiber source for coherent Raman microscopy," *Opt. Lett.* **34**, 2051–2053 (2009).
6. F. Ganikhanov, S. Carrasco, X. S. Xie, M. Katz, W. Seitz, and D. Kopf, "Broadly tunable dual-wavelength light source for coherent anti-Stokes Raman scattering microscopy," *Opt. Lett.* **31**, 1292–1294 (2006).
7. K. Yamakawa, M. Aoyama, S. Matsuoka, T. Kase, Y. Akahane, and H. Takuma, "100-TW sub-20-fs Ti:sapphire laser system operating at a 10-Hz repetition rate," *Opt. Lett.* **23**, 1468–1470 (1998).
8. K. C. Burr, C. L. Tang, M. A. Arbore, and M. M. Fejer, "High-repetition-rate femtosecond optical parametric oscillator based on periodically poled lithium niobate," *Appl. Phys. Lett.* **70**, (1997).
9. E. Innerhofer, T. Südmeyer, F. Brunner, R. Paschotta, and U. Keller, "Mode-locked high-power lasers and nonlinear optics – a powerful combination," *Laser Phys. Lett.* **1**, 82 (2004).
10. G. R. Holtom, "Mode-locked Yb:KGW laser longitudinally pumped by polarization-coupled diode bars," *Opt. Lett.* **31**, 2719 (2006).
11. A. Major, R. Cisek, and V. Barzda, "Femtosecond Yb:KGd(WO₄)₂ laser oscillator pumped by a high power fiber-coupled diode laser module," *Opt. Express* **14**, 12163–12168 (2006).
12. A.-L. Calendron, K. S. Wentsch, and M. J. Lederer, "High power cw and mode-locked oscillators based on Yb:KYW multi-crystal resonators," *Opt. Express* **16**, 18838–18843 (2008).
13. A. Major, R. Cisek, D. Sandkuijl, and V. Barzda, "Femtosecond Yb:KGd(WO₄)₂ laser with > 100 nJ of pulse energy," *Laser Phys. Lett.* **6**, 272–274 (2009).
14. Y. X. Fan, R. C. Eckardt, R. L. Byer, J. Nolting, and R. Wallenstein, "Visible BaB₂O₄ optical parametric oscillator pumped at 355 nm by a single-axial-mode pulsed source," *Appl. Phys. Lett.* **53**, (1988).
15. Y. X. Fan, R. C. Eckardt, R. L. Byer, C. Chen, and A. D. Jiang, "Barium borate optical parametric oscillator," *IEEE J. Quantum Electron.* **25**, 1196–1199 (1989).
16. H. Komine, "Average-power scaling for ultraviolet-pumped β -barium borate and lithium triborate optical parametric oscillators," *J. Opt. Soc. Am. B* **10**, 1751–1757 (1993).
17. H. Zhou, J. Zhang, T. Chen, C. Chen, and Y. R. Shen, "Picosecond, narrow-band, widely tunable optical parametric oscillator using a temperature-tuned lithium borate crystal,"

- Appl. Phys. Lett. **62**, (1993).
18. G. Robertson, A. Henderson, and M. H. Dunn, "Broadly tunable LiB_3O_5 optical parametric oscillator," Appl. Phys. Lett. **60**, (1992).
 19. D. N. Nikogosyan, "Beta barium borate (BBO)," Appl. Phys. A **52**, 359–368 (1991).
 20. C. Chen, "A new-type ultraviolet SHG crystal- $\beta\text{-BaB}_2\text{O}_4$," Sci. Sinca (Ser. B) **28**, 235–243 (1985).
 21. L. J. Bromley, A. Guy, and D. C. Hanna, "Synchronously pumped optical parametric oscillation in beta-barium borate," Opt. Commun. **67**, 316–320 (1988).
 22. D. Eimerl, L. Davis, S. Velsko, E. K. Graham, and A. Zalkin, "Optical, mechanical, and thermal properties of barium borate," J. Appl. Phys. **62**, (1987).
 23. W. R. Bosenberg, L. K. Cheng, and C. L. Tang, "Ultraviolet optical parametric oscillation in $\beta\text{-BaB}_2\text{O}_4$," Appl. Phys. Lett. **54**, (1989).
 24. H. Komine, "Optical parametric oscillation in a beta-barium borate crystal pumped by an XeCl excimer laser," Opt. Lett. **13**, 643–645 (1988).
 25. L. K. Cheng, W. R. Bosenberg, and C. L. Tang, "Broadly tunable optical parametric oscillation in $\beta\text{-BaB}_2\text{O}_4$," Appl. Phys. Lett. **53**, (1988).
 26. W. R. Bosenberg, W. S. Pelouch, and C. L. Tang, "High-efficiency and narrow-linewidth operation of a two-crystal $\beta\text{-BaB}_2\text{O}_4$ optical parametric oscillator," Appl. Phys. Lett. **55**, (1989).
 27. S. Burdulis, R. Grigonis, A. Piskarskas, G. Sinkevicius, V. Sirutkaitis, A. Fix, J. Nolting, and R. Wallenstein, "Visible optical parametric oscillation in synchronously pumped beta-barium borate," Opt. Commun. **74**, 398–402 (1990).
 28. G. M. Gale, M. Cavallari, and F. Hache, "Femtosecond visible optical parametric oscillator," J. Opt. Soc. Am. B **15**, 702–714 (1998).
 29. C. Chen, Y. Wu, A. Jiang, B. Wu, G. You, R. Li, and S. Lin, "New nonlinear-optical crystal: LiB_3O_5 ," J. Opt. Soc. Am. B **6**, 616–621 (1989).
 30. T. Schröder, K.-J. Boller, A. Fix, and R. Wallenstein, "Spectral properties and numerical modelling of a critically phase-matched nanosecond LiB_3O_5 Optical Parametric Oscillator," Appl. Phys. B **58**, 425–438 (1994).
 31. S. Lin, Z. Sun, B. Wu, and C. Chen, "The nonlinear optical characteristics of a LiB_3O_5 crystal," J. Appl. Phys. **67**, (1990).
 32. C. L. Tang, W. R. Bosenberg, T. Ukachi, R. J. Lane, and L. K. Cheng, "Optical parametric oscillators," Proc. IEEE **80**, 365–374 (1992).
 33. Y. Tang, Y. Cui, and M. H. Dunn, "Lithium triborate optical parametric oscillator pumped at 266 nm," Opt. Lett. **17**, 192–194 (1992).
 34. V. Petrov, M. Ghotbi, O. Kokabee, A. Esteban-Martin, F. Noack, A. Gaydardzhiev, I. Nikolov, P. Tzankov, I. Buchvarov, K. Miyata, A. Majchrowski, I. V Kityk, F. Rotermund, E. Michalski, and M. Ebrahim-Zadeh, "Femtosecond nonlinear frequency conversion based on BiB_3O_6 ," Laser Photon. Rev. **4**, 53–98 (2010).
 35. M. Ghotbi and M. Ebrahim-Zadeh, "Optical second harmonic generation properties of BiB_3O_6 ," Opt. Express **12**, 6002–6019 (2004).
 36. M. Ghotbi and M. Ebrahim-Zadeh, "990 mW average power, 52% efficient, high-repetition-rate picosecond-pulse generation in the blue with BiB_3O_6 ," Opt. Lett. **30**, 3395–3397 (2005).
 37. A. Major, K. Sukhoy, H. Zhao, and I. T. Lima, "Green sub-nanosecond microchip laser based on BiBO crystals," Laser Phys. **21**, 57–60 (2011).

38. A. Major, D. Sandkuijl, and V. Barzda, "Efficient frequency doubling of a femtosecond Yb:KGW laser in a BiB₃O₆ crystal," *Opt. Express* **17**, 12039 (2009).
39. Y. F. Lü, X. H. Zhang, R. Chen, J. Xia, J. F. Chen, and Z. T. Liu, "Diode-pumped Nd:YAG/BiB₃O₆ deep-blue laser at 449.5 nm," *Laser Phys. Lett.* **7**, 347 (2010).
40. K. Miyata, N. Umemura, and K. Kato, "Phase-matched pure $\chi^{(3)}$ third-harmonic generation in noncentrosymmetric BiB₃O₆," *Opt. Lett.* **34**, 500–502 (2009).
41. Z. Sun, M. Ghotbi, and M. Ebrahim-Zadeh, "Widely tunable picosecond optical parametric generation and amplification in BiB₃O₆," *Opt. Express* **15**, 4139–4148 (2007).
42. M. Ghotbi, M. Ebrahim-Zadeh, V. Petrov, P. Tzankov, and F. Noack, "Efficient 1 kHz femtosecond optical parametric amplification in BiB₃O₆ pumped at 800 nm," *Opt. Express* **14**, 10621–10626 (2006).
43. M. Ghotbi, A. Esteban-Martin, and M. Ebrahim-Zadeh, "BiB₃O₆ femtosecond optical parametric oscillator," *Opt. Lett.* **31**, 3128–3130 (2006).
44. A. Esteban-Martin, V. Ramaiah-Badarla, V. Petrov, and M. Ebrahim-Zadeh, "Broadband, rapidly tunable Ti:sapphire-pumped BiB₃O₆ femtosecond optical parametric oscillator," *Opt. Lett.* **36**, 1671–1673 (2011).
45. M. Peltz, J. Bartschke, A. Borsutzky, R. Wallenstein, S. Vernay, T. Salva, and D. Rytz, "Bismuth triborate (BiB₃O₆) optical parametric oscillators," *Appl. Phys. B* **80**, 55–60 (2005).
46. S. Manjooran, H. Zhao, I. T. Lima, and A. Major, "Phase-matching properties of PPKTP, MgO:PPSLT and MgO:PPcLN for ultrafast optical parametric oscillation in the visible and near-infrared ranges with green pump," *Laser Phys.* **22**, 1325–1330 (2012).
47. H. Zhao, K. Sukhoy, J. I T Lima, and A. Major, "Generation of green second harmonic with 60% conversion efficiency from a Q-switched microchip laser in MgO:PPLN crystal," *Laser Phys. Lett.* **9**, 355 (2012).
48. H. Zhao, I. T. Lima, and A. Major, "Near-infrared properties of periodically poled KTiOPO₄ and stoichiometric MgO-doped LiTaO₃ crystals for high power optical parametric oscillation with femtosecond pulses," *Laser Phys.* **20**, 1404–1409 (2010).
49. I. T. Lima, V. Kultavewuti, and A. Major, "Phasematching properties of congruent MgO-doped and undoped periodically poled LiNbO₃ for optical parametric oscillation with ultrafast excitation at 1 μ m," *Laser Phys.* **20**, 270–275 (2010).
50. K. Kato, "Second-harmonic generation to 2048 Å in B-Ba₂O₄," *IEEE J. Quantum Electron.* **22**, 1013–1014 (1986).
51. D. Zhang, Y. Kong, and J. Zhang, "Optical parametric properties of 532-nm-pumped beta-barium-borate near the infrared absorption edge," *Opt. Commun.* **184**, 485–491 (2000).
52. G. Ghosh, "Temperature dispersion of refractive indices in β -BaB₂O₄ and LiB₃O₅ crystals for nonlinear optical devices," *J. Appl. Phys.* **78**, (1995).
53. M. Ebrahimzadeh, A. J. Henderson, and M. H. Dunn, "An excimer-pumped β -BaB₂O₄ optical parametric oscillator tunable from 354 nm to 2.370 μ m," *IEEE J. Quantum Electron.* **26**, 1241–1252 (1990).
54. L. A. W. Gloster, Z. X. Jiang, and T. A. King, "Characterization of an Nd:YAG-pumped β -BaB₂O₄ optical parametric oscillator in collinear and noncollinear phase-matched configurations," *IEEE J. Quantum Electron.* **30**, 2961–2969 (1994).
55. X. D. Zhu and L. Deng, "Broadly tunable picosecond pulses generated in a β -BaB₂O₄ optical parametric amplifier pumped by 0.532 μ m pulses," *Appl. Phys. Lett.* **61**, (1992).
56. K. Kato, "Temperature-tuned 90° phase-matching properties of LiB₃O₅," *IEEE J. Quantum*

- Electron. **30**, 2950–2952 (1994).
57. S. Lin, J. Y. Huang, J. Ling, C. Chen, and Y. R. Shen, "Optical parametric amplification in a lithium triborate crystal tunable from 0.65 to 2.5 μm ," *Appl. Phys. Lett.* **59**, (1991).
 58. S. P. Velsko, M. Webb, L. Davis, and C. Huang, "Phase-matched harmonic generation in lithium triborate (LBO)," *IEEE J. Quantum Electron.* **27**, 2182–2192 (1991).
 59. Y. Tang, Y. Cui, and M. H. Dunn, "Thermal dependence of the principal refractive indices of lithium triborate," *J. Opt. Soc. Am. B* **12**, 638–643 (1995).
 60. H. Mao, B. Wu, C. Chen, D. Zhang, and P. Wang, "Broadband optical parametric amplification in LiB_3O_5 ," *Appl. Phys. Lett.* **62**, (1993).
 61. J. Y. Zhang, J. Y. Huang, Y. R. Shen, and C. Chen, "Optical parametric generation and amplification in barium borate and lithium triborate crystals," *J. Opt. Soc. Am. B* **10**, 1758–1764 (1993).
 62. M. Ebrahimzadeh, G. J. Hall, and A. I. Ferguson, "Broadly tunable, all-solid-state, visible and infrared picosecond optical parametric oscillator," *Opt. Lett.* **18**, 278–280 (1993).
 63. T. W. Tukker, C. Otto, and J. Greve, "Design, optimization, and characterization of a narrow-bandwidth optical parametric oscillator," *J. Opt. Soc. Am. B* **16**, 90–95 (1999).
 64. G. Robertson, M. J. Padgett, and M. H. Dunn, "Continuous-wave singly resonant pump-enhanced type II LiB_3O_5 optical parametric oscillator," *Opt. Lett.* **19**, 1735–1737 (1994).
 65. H. Hellwig, J. Liebertz, and L. Bohatý, "Linear optical properties of the monoclinic bismuth borate BiB_3O_6 ," *J. Appl. Phys.* **88**, (2000).
 66. N. Umemura, K. Miyata, and K. Kato, "New data on the optical properties of BiB_3O_6 ," *Opt. Mater.* **30**, 532–534 (2007).
 67. N. Umemura, S. Banerjee, K. Miyata, F. Tanno, and K. Kato, "Thermo-Optic Dispersion Formula for BiB_3O_6 ," in *Conference on Lasers and Electro-Optics/Quantum Electronics and Laser Science and Photonic Applications Systems Technologies (Optical Society of America, 2005)*, p. JTuC18.
 68. M. Peltz, J. Bartschke, A. Borsutzky, R. Wallenstein, T. Salva, S. Vernay, and D. Rytz, "Low threshold optical parametric oscillation and third harmonic generation in the new nonlinear optical material BiB_3O_6 ," *Lasers Electro-Optics CLEO 1*, 332–333 (2002).
 69. S. Lin, M. Sharifi, R. J. D. Miller, R. Castelino, and S. Foster, "High Repetition Rate Bismuth Borate Optical Parametric Oscillator Pumped by a Cavity-Dumped Nd:YLF Laser," in *Conference on Lasers and Electro-Optics/International Quantum Electronics Conference (Optical Society of America, 2009)*, p. JWA13.
 70. D. A. Roberts, "Simplified characterization of uniaxial and biaxial nonlinear optical crystals: a plea for standardization of nomenclature and conventions," *IEEE J. Quantum Electron.* **28**, 2057–2074 (1992).
 71. W. R. Bosenberg and C. L. Tang, "Type II phase matching in a β -barium borate optical parametric oscillator," *Appl. Phys. Lett.* **56**, (1990).
 72. S. R. Greenfield and M. R. Wasielewski, "Near-transform-limited visible and near-IR femtosecond pulses from optical parametric amplification using Type II β -barium borate," *Opt. Lett.* **20**, 1394–1396 (1995).
 73. G. Cerullo and S. De Silvestri, "Ultrafast optical parametric amplifiers," *Rev. Sci. Instrum.* **74**, (2003).
 74. F. Brehat and B. Wyncke, "Calculation of double-refraction walk-off angle along the phase-matching directions in non-linear biaxial crystals," *J. Phys. B At. Mol. Opt. Phys.* **22**, 1891 (1989).

75. A. Nebel, C. Fallnich, R. Beigang, and R. Wallenstein, "Noncritically phase-matched continuous-wave mode-locked singly resonant optical parametric oscillator synchronously pumped by a Ti:sapphire laser," *J. Opt. Soc. Am. B* **10**, 2195–2200 (1993).
76. A. Mokhtari, L. Fini, and J. Chesnoy, "Efficient frequency mixing of a cw femtosecond laser synchronously pumped by a frequency doubled Nd:YAG laser," *Opt. Commun.* **61**, 421–424 (1987).
77. Powers, P. E., "Fundamentals of nonlinear optics." CRC Press, 2011

Chapter 7

Conclusions and future works

7.1. Conclusions

The main focus of this thesis was to develop a high power ultrafast laser source which can be considered as substitution to the widely used, but inefficient and costly Ti:sapphire laser and its concomitant external laser amplifier system. In fact, the demonstrated lasers in this work delivered comparable output powers in sub-100 fs regime to Ti:sapphire laser oscillator. Such a compact and efficient watt-level femtosecond laser source is required, for example, for nonlinear biomedical imaging, material spectroscopy and the study of nonlinear properties of materials. The demonstrated laser systems based on a diode-pumped Yb:KGW laser crystal were compact, efficient and cost-effective. Using the Yb:KGW laser crystal enabled us to generate watt-level output power due to its fairly high thermal conductivity and the absence of non-radiative losses. A fairly broad spectral gain bandwidth of this crystal also facilitated generation of ultra-short pulses.

During the development of the laser system, a high power dual-wavelength continuous wave laser was demonstrated. Based on a simple approach, this laser exhibited substantial enhancement in terms of the output power and optical-to-optical efficiency when compared with prior work.

High power femtosecond laser systems were demonstrated by using two well-known techniques: semiconductor saturable absorber and Kerr-lens mode locking. The hybrid action of these techniques allowed us to generate reliable multi-watt sub-100 fs laser pulses. The employed saturable absorber mirror was a novel quantum-dot based saturable absorber. The laser showed a substantial improvement in output power when compared with the previous work based on QD-SESAMs. Furthermore, the generation of the shortest pulses from monoclinic double tungstate crystals (and Yb:KGW laser crystal in particular) and the most powerful in the sub-60 fs regime was also demonstrated using this technique.

By using the Kerr-lens mode-locking technique, a high power pure Kerr-lens mode-locked Yb:KGW laser pumped by a highly multimode fiber-coupled diode laser was demonstrated. This

laser was the first demonstration of a watt-level KLM laser among the Yb-ion doped bulk lasers which used multimode fiber-coupled laser diode module as a pump. The optical-to-optical efficiency in this work was also higher than the overall efficiency of high power KLM lasers where fiber laser systems were used for pumping.

All of these demonstrations extended the boundaries of the generation of high power ultra-short laser pulses based upon efficient, compact and cost effective approach. Such laser systems can be used as the source of excitation for imaging and spectroscopy experiments and also an optical parametric oscillator (OPO).

7.2. Future works

Some aspects of the demonstrated laser systems are subject to improvement. In this section, possible solutions are suggested, which may result in enhancement of the performance of the demonstrated lasers in terms of output power and pulse duration as well as the elimination of undesired features.

For the case of CW dual-wavelength laser, larger variety of wavelength pairs can be generated by using birefringent filter plates with different thicknesses. The CW dual-wavelength laser can be also developed to generate terahertz radiation using a photoconductive antenna (photomixer). Such a terahertz radiation is useful for THz imaging and spectroscopy applications.

In case of the ultrafast laser, providing a group-delay dispersion (GDD) compensation for a wide range of wavelength with a smooth dispersion profile is of crucial importance to ultrafast laser. In chapter 4, it was shown that a dispersive wave appeared at long wavelengths, co-propagating with the main pulse. The appearance of the dispersive wave is due to the rapidly shifting GDD profile of one of the GTI mirrors into the normal regime. Therefore, using GTI mirrors with wider and smoother dispersive profile can help to eliminate such a dispersive wave, further broaden the pulse spectrum into the longer wavelengths and, therefore, generate shorter pulses.

In addition, by using a high power fiber-coupled laser diode with better beam quality (smaller M^2 factor) as the pump source improvement for our femtosecond lasers is possible. A better beam quality of the pump enhances the performance of a laser through a more efficient

mode-matching between the laser mode and pump beam. Therefore, it is speculated that the optical-to-optical efficiency of the laser will be improved. A better mode-matching also improves the soft-aperturing effect in the Kerr-lens mode locking mechanism (Chapter 2). Therefore, it will be possible to suppress the undesired CW background radiation in case of the pure Kerr-lens mode-locked laser (Chapter 5), which would translate into shorter pulses with higher output power. Another possible solution to improving the KLM laser performance would be using a shorter length of the laser crystal with higher doping level so that more effective soft-aperturing effect can be provided between the highly diverging pump beam and the laser mode.

Laser oscillation with other polarizations (e.g. $E//N_p$ or $E//N_g$) may result in generation of even shorter pulses since the spectral gain bandwidth for these polarizations is broader than for the polarization along the N_m -axis of the crystal (Chapter 2). These polarizations, however, exhibit smaller values of emission cross-section and therefore the generated output power can be lower than the results of this work.

Future development of the proposed high power ultrashort lasers also involves the generation of even higher pulse energies by extending the length of the laser cavity. It is based on the fact that the energy of the pulse is related to the product of the average output power and the period of repetition rate of the pulses. This would eliminate the need for external amplifier for further pulse amplification and up to 1000 nJ of pulse energy can be reached for a long enough laser cavity.

Finally, the demonstrated ultrafast lasers can be developed into a femtosecond laser with widely tunable wavelength by using it as the pump source of an optical parametric oscillator (OPO), as investigated in chapter 6. It would result in a compact and efficient OPO laser source for spectroscopy and microscopy applications.

Appendix A

The beam quality factor (M^2)

The beam quality factor is a measure of the spatial quality of a laser beam. This dimensionless factor relates the beam divergence and the minimum achievable beam waist for the beam and for a given wavelength as [1]

$$M^2 = \theta \frac{\pi \omega_0}{\lambda} \quad \text{Eq.A.1}$$

where ω_0 is the beam waist, λ is wavelength and θ is half-angle beam divergence. A diffraction-limited Gaussian beam has $M^2=1$. Therefore, a higher M^2 factor shows a deviation of the laser beam from an ideal Gaussian beam.

References

1. W. Koechner, "Solid-state laser engineering," Springer (2013).

Appendix B

Ray transfer matrix analysis (ABCD matrix analysis)

The effect of an optical system on a propagating wave can be analyzed by using the ray transfer matrix analysis (or ABCD matrix analysis) [1]. This analysis is widely used for ray optics and the Gaussian beams with paraxial approximation. In this method each optical element is ascribed to a 2×2 matrix and the optical system is then described by a matrix which is the product of the constituent matrices. In case of a Gaussian beam, a complex quantity (q) is used to calculate the parameters of the beam after its propagation through the system. The q parameter contains information about the beam radius and radius of curvature of the beam wavefront,

$$\frac{1}{q} = -i \frac{\lambda}{\pi \omega^2} + \frac{1}{R} \quad \text{Eq.B.1}$$

where λ is wavelength, and ω and R are the beam radius and the radius of wavefront curvature of a beam, respectively, prior to its entering into the optical system. The q parameter of the output beam will be then transformed into,

$$q' = \frac{Aq+B}{Cq+D} \quad \text{Eq.B.2}$$

where A , B , C and D are the matrix elements of the total matrix of the system.

The ABCD matrix analysis can be also used to calculate the parameters of the fundamental laser mode in a laser resonator. Since a laser cavity consists of elements such as reflective mirrors, propagation distance in air and in the laser crystal, the total matrix of the laser cavity is calculated from the roundtrip product of all the constituent elements. In this way, the beam waist of the laser mode in the cavity or the beam size in the gain crystal can be calculated. The thermal lensing strength of the gain medium in the laser cavity can be also estimated by using the ABCD matrix analysis [2]. In this case, the thermal lensing effect is approximated by an equivalent focal length of a lens element in the gain medium so that the output laser beam has the same parameters as measured in the experiment.

References

1. B. E. A Saleh, M. C. Teich, "Fundamentals of photonics," Wiley, 2007.
2. H. Mirzaeian, S. Manjooran, A. Major, Proc. SPIE **9288**, 928802-1 (2014).

Appendix C

The Sellmeier equation

The refractive index of an optical medium is expressed by an empirical equation as a function of wavelength, which is called the Sellmeier equation or dispersion formula. It describes the dispersion of wavelength in a transparent medium. The general Sellmeier formula is

$$n(\lambda)^2 = A + \sum_i \frac{B_i}{\lambda^2 - C_i} + D_i \lambda^{2i} \quad \text{Eq.C.1}$$

where A , B_i , C_i and D_i are the Sellmeier's coefficients of the medium. In the following, the Sellmeier's coefficients for pure KGW crystal (Chapter 4) and nonlinear crystals BBO, LBO and BIBO (Chapter 6) are presented.

		A	B_1	C_1	D_1	D_2	D_3
BBO [1]	n_o	2.7359	0.01878	0.01822	-0.01471	6.081×10^{-4}	-0.00006740
	n_e	2.3753	0.01224	0.01667	-0.01627	5.716×10^{-4}	-0.00006305
LBO [2]	n_x	2.45316	0.01150	0.01058	-0.01123	-	-
	n_y	2.53969	0.01249	0.01339	-0.02029	-	-
	n_z	2.58515	0.01412	0.00467	-0.0179132	-4.17241×10^{-4}	7.65183×10^{-6}
BIBO[3]	n_x	3.07403	0.03231	0.03163	-0.013376	-	-
	n_y	3.16940	0.03717	0.03483	-0.01827	-	-
	n_z	3.6545	0.05112	0.03713	-0.02261	-	-

For pure KGW crystal, a modified Sellmeier formula was used as

$$n(\lambda) = A + \frac{B}{1 - \left(\frac{C}{\lambda}\right)^2} - D\lambda^2 \quad \text{Eq.C.2}$$

		<i>A</i>	<i>B</i>	<i>C/nm</i>	<i>D/nm²</i>
KGW [4]	<i>n_g</i>	1.3867	0.6573	170.02	0.2913×10 ⁻⁹
	<i>n_m</i>	1.5437	0.4541	188.91	2.1567×10 ⁻⁹
	<i>n_p</i>	1.5344	0.4360	186.18	2.0999×10 ⁻⁹

References

1. D. Zhang, Y. Kong, and J. Zhang, "Optical parametric properties of 532-nm-pumped beta-barium-borate near the infrared absorption edge," *Opt. Commun.* **184**, 485–491 (2000).
2. S. Lin, J. Y. Huang, J. Ling, C. Chen, and Y. R. Shen, "Optical parametric amplification in a lithium triborate crystal tunable from 0.65 to 2.5 μm," *Appl. Phys. Lett.* **59**, (1991).
3. N. Umemura, K. Miyata, and K. Kato, "New data on the optical properties of BiB₃O₆," *Opt. Mater.* **30**, 532–534 (2007).
4. M. C. Pujol, M. Rico, C. Zaldo, R. Solé, V. Nikolov, X. Solans, M. Aguiló, and F. Díaz, "Crystalline structure and optical spectroscopy of Er³⁺-doped KGd(WO₄)₂ single crystals," *Appl. Phys. B* **68**, 187–197 (1999).

Appendix D

The Kerr-lens mode locking sensitivity

In a Kerr-lens mode-locked laser, the laser gain crystal or an additional optical medium with large nonlinear refractive index induces the Kerr lensing effect in the presence of an intense pulse. However, the position of the nonlinear medium and the waist of a laser mode determine the strength of this effect. In general, the laser mode distribution in a cavity can be calculated by using the ray-tracing ABCD matrix analysis which defines matrices for the optical components in the cavity [1]. Using this method it is possible to define the strength of the Kerr lensing effect by only employing linear matrices of the components. The Kerr-lens mode locking sensitivity can be expressed as [2]

$$\delta = \left. \frac{1}{\omega} \frac{d\omega}{dP} \right|_{P=0} \quad \text{Eq.D.1}$$

where ω is the laser beam size and P is the intra-cavity beam power. This parameter shows the rate of change of a laser mode size at the hard-aperture (in case of hard-aperture mode locking) or in a laser gain medium (in case of soft-aperture Kerr-lens mode locking (chapter 2, figure 2.8)) with respect to optical power in the Kerr medium. In order to have a relatively strong Kerr lensing effect which would effectively reduce the size of a laser mode, the sensitivity parameter need to be a large and negative value. It can be shown that the position of the laser crystal and the separation of the folding mirrors around the gain medium have a crucial effect on the Kerr sensitivity value [1,2].

References

1. V. Magni, G. Cerullo, and S. De Silvestri, "ABCD matrix analysis of propagation of gaussian beams through Kerr media," *Opt. Commun.* **96**, 348–355 (1993).
2. V. Magni, G. Cerullo, and S. De Silvestri, "Closed form gaussian beam analysis of resonators containing a Kerr medium for femtosecond lasers," *Opt. Commun.* **101**, 365–370 (1993).

Appendix E

Optical parametric generation

Ultra-short pulses with high peak power can couple energy into the induced nonlinear polarization P in a nonlinear crystal as follows [1,2]

$$P = P_0 + \varepsilon_0\chi^{(1)}E + \varepsilon_0\chi^{(2)}E^2 + \dots \quad \text{Eq.E.1}$$

where P_0 is the intrinsic polarization, ε_0 is the permittivity of free space and $\chi^{(i)}$ are the susceptibility coefficients and E is the electric field strength. Efficient interaction between the waves requires phase-matching and energy conservation conditions

$$\begin{aligned} \omega_p &= \omega_s + \omega_i \\ \vec{k}_p &= \vec{k}_s + \vec{k}_i \end{aligned} \quad \text{Eq.E.2}$$

to be satisfied, where \vec{k} is the wave vector with absolute value of $|\vec{k}| = \omega n/c$, n is the refractive index, c is the speed of light in vacuum, ω is the angular frequency of wave, and p, s, i stand for the pump, signal and idler, respectively. The phase-matching condition depends on the refractive indices which, in turn, depend on the propagation direction and polarization states of waves (i, p, s), wavelength and temperature ($|\vec{k}| = 2\pi n(\theta, T, \lambda)/\lambda$). Therefore, the phase-matching condition for different wavelengths can be fulfilled for different geometry of the crystal, temperature and polarization of the interacting waves.

The phase-matching between the pump, signal and idler is possible in two general categories of crystal structures: uniaxial and biaxial birefringent crystals. The structures of these two types of crystals are depicted in figure E.1. The refractive indices of principal axes for a unit cell crystal are given by the Sellmeier's equations and the corresponding refractive index for the phase-matched waves (i, p, s) can be calculated based on them [1,2].

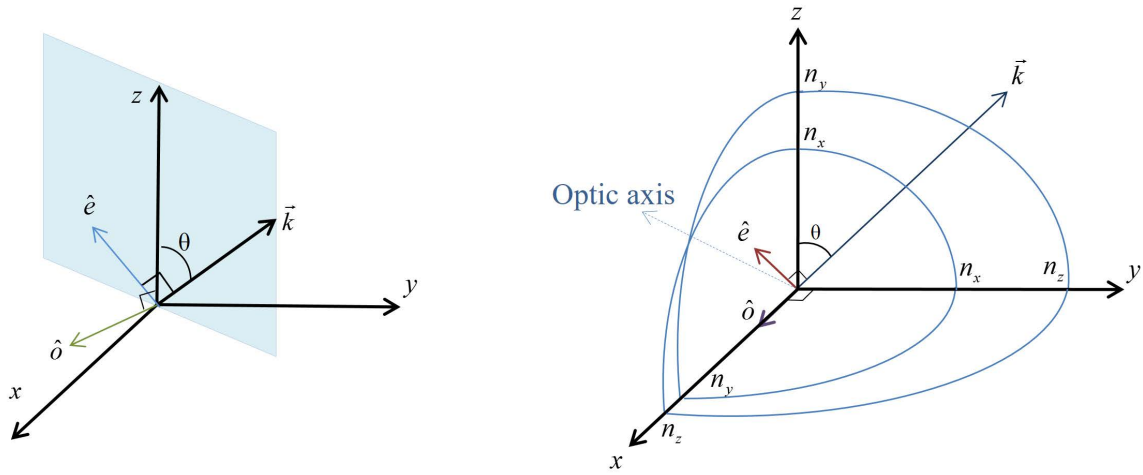


Figure E.1. Uniaxial crystal (a) and biaxial crystal (b); \vec{k} defines the propagation direction of a wave (i, s, p); \hat{e} and \hat{o} are the unit vectors of possible polarization state of the wave; the intersecting curves in (b) define the values of the refractive indices for a wave (\vec{k}), given by the Fresnel's equation.

The uniaxial crystal has two principal refractive indices and its optic axis, by convention, is along the z-axis. If the polarization vector of a wave is perpendicular to the plane formed by its wave vector (\vec{k}) and the optic axis, the wave is called ordinary wave (o-wave) and its corresponding refractive index is constant (n_o) and independent of its angle θ with respect to the optic axis. If the polarization vector of the wave is in the same plane formed by the vector and optic axis, it is called an extra-ordinary wave (e-wave) and the refractive index along its propagation path varies as

$$\frac{1}{n_e^2(\theta)} = \frac{\cos^2(\theta)}{n_o^2} + \frac{\sin^2(\theta)}{n_z^2}. \quad \text{Eq.E.3}$$

Therefore, for a specific angle of propagation and polarization states of interacting waves the phase-matching condition (Eq.E.2) can be satisfied. In a biaxial structure, there are three principal axes of refractive index (figure E.1(b)) and if a wave is propagating in one of three principal planes formed by these axes, the situation can be treated similar to the uniaxial structure.

References

1. P. E. Powers, "Fundamentals of nonlinear optics." CRC Press, 2011
2. R. L. Sutherland, "Handbook of nonlinear optics." CRC press, 2003